DISSERTATION

Prediction of aerodynamic parameters of plant canopies and of soil heating in ridges covered with plastic mulch as contributions to SVAT modelling

zur Erlangung des akademischen Grades

doctor rerum agriculturarum

(Dr. rer. agr.)

eingereicht an der

Landwirtschaftlich-Gärtnerischen Fakultät

der Humboldt-Universität zu Berlin

von Jan Gräfe

geboren am 28.12.1965 in Storkow (Mark), Deutschland

Dekan der Landwirtschaftlich-Gärtnerischen Fakultät: Prof. Dr. Dr. h.c. Otto Kaufmann

Gutachter:

1. Prof. Dr. Christel Richter
2. Prof. Dr. Matthias Langensiepen
3. Prof. Dr. Thomas Foken

Tag der mündlichen Prüfung: 16.3. 2006

Zusammenfassung

Die Implementierung und Anwendung von Soil-Vegetation-Atmosphere-Transport-Modellen (SVAT) in der Landwirtschaft erfordert die Kenntnis der aerodynamischen Eigenschaften der Unterlage. Diese sind die Verschiebungslänge d, die Rauhigkeitslänge z_0 und weitere Parameter welche den Effekt der Rauhigkeitsschicht unmittelbar über dem Pflanzenbestand beschreiben, wie die Schichthöhen für den Transfer von Impuls Z_{m*} und Skalaren Z_{s*}. Umfangreiche Literaturangaben über einen weiten Bereich von Bestandsmerkmalen wurden zur Entwicklung und Ableitung neuer Schätzfunktionen der genannten Parameter genutzt. Ein neues Modell wird für d als Funktion der Bestandeshöhe h_c und dem Plant Area Index PAI vorgeschlagen. Ein semi-empirisches Vorhersagemodell wird für die Längenskale L_s in Abhängigkeit von h_c, PAI, der relativen Kronenhöhe und dem mittleren Abstand zwischen Rauhigkeitselementen entwickelt. Mit Schätzwerten für d, L_s, Z_{m*} und anderen Inputs wurde eine Gleichung für z_0 entwickelt und geprüft. Unter Berücksichtigung der Rauhigkeitsschicht werden geschlossene analytische Lösungen für die Schubspannungsgeschwindigkeit, das Windprofil und den aerodynamischen Widerstand präsentiert.

Es wird ein Energiebilanzmodell für teilweise mit Folien bedeckten Erddämmen vorgestellt. Bekannte Vorgehensweisen aus der Literatur wurden hinsichtlich der Effekte des peripheren Strahlungsanteils der Sonne, der Modifizierung des kurzwelligen und langwelligen Strahlungstransfers durch den Damm selbst und der winkelabhängigen Transmission und Reflexion von Folien erweitert. Nur 3 Parameter mussten aus stündlichen Messwerten der Bodentemperatur über einen Monat bestimmt werden. Beim Gesamttest des Modells zeigte sich eine mittlere quadratische Abweichung zwischen Simulationen und Messungen der Dammtemperatur von 1.5-1.9 K in Abhängigkeit vom Standort. Testsimulationen zeigten, dass für strahlungsundurchlässige Folien eine präzise Darstellung der winkelabhängigen Reflexion nicht notwendig ist. Für transparente Folien sind zur Beschreibung von Transmission und Reflexion auch einfache Ansätze ausreichend. Nur wenige Inputs sind zur Simulation erforderlich wie die Gehalte an Humus, Sand und Ton, die Dammgeometrie und die Transmissions- und Reflexionsgrade der eingesetzten Folien.

Summary

Implementation and application of Soil Vegetation Atmosphere Transport Models (SVAT) in agriculture require knowledge of aerodynamic properties of the exchanging surface. These are the zero plane displacement d, the roughness length for momentum z_0, and additional parameters describing the roughness layer just above the canopy as the height of the roughness layer for momentum and scalars (Z_{m*}, Z_{s*}), and parameters of the modified diffusivity profile functions. Several data summaries from the literature on aerodynamic properties over a broad range of plant canopies are used to develop and test predictive models for a number of needed aerodynamic parameters. A new model for d is presented as a function of canopy height h_c and Plant Area Index PAI. A semi-empirical equation for the canopy length scale L_s is derived from h_c, PAI, fractional crown height, and inter-element spacing of roughness elements. Having estimates of d, L_s, Z_{m*} and other inputs one can derive predictive equations for z_0. Closed form analytical expressions are given for the friction velocity, the horizontal wind speed profile and the aerodynamic resistance**,** which account for both stability and roughness layer effects.

An energy balance model for a two-dimensional ridge surface partly covered by a plastic mulch is presented. Previous approaches are modified and extended to include (1) the circumsolar part of diffuse radiation and (2) the altered interception of diffuse short- and long-wave radiation due to horizon obstructions and surface slope and (3) the directional dependence of transmissivity and reflectivity of plastic mulches. Only three parameters had to be estimated from data taken over one month at one site. Overall, simulated data fitted with the whole data set on soil temperatures, with root mean square errors of 1.5 K and 1.9 K for both sites, respectively. Test simulations established that for opaque plastics, detailed analysis of directional radiative properties is not necessary, and for transparent plastics, rather simpler approaches are sufficient. Only a few inputs have to be provided to apply the model: the soil humus content and texture, the shape of the ridge, and the transmissivities and reflectivities of the used plastic mulches in the short-wave and long-wave range.

To my patient wife Peggy

and

my daughters Theresa and Martha

Danksagung

Hiermit möchte ich mich bei Frau Prof. Dr. Christel Richter für das andauernde Interesse an der Thematik und Ihr stetes Drängen auf eine präzise Darstellung bedanken.

Ebenso möchte ich meinen Kollegen Frau Dr. Carmen Feller und Herrn Dr. Adolf Heißner meinen Dank für die vielen konstruktiven Diskussionen zur Ableitung der Energiebilanz und zur geeigneten Darstellung der Simulationsergebnisse aussprechen. Bei Frau Dr. Stefanie Schmidt und Herrn Ingo Hauschild möchte ich mich für die organisatorisch-technische Umsetzung der Validierungsversuche bedanken.

Table of Contents

1 Introduction

Our understanding of structural relationships of agricultural systems has come a long way since the early pioneering work of DE WIT (1965). Due to the advent and rapid advances of computational technologies, methods from system analysis and mathematical modelling can be better exploited to gain further insights.

A mathematical model of an agricultural system is an abstraction or simplified idealisation of the real world. Such models apply several methods from mathematics, where the methods used (*e.g.* ordinary differential equations, partial differential equations, markov chains, cellular automates, probability distributions) vary with the kind of system investigated. A system is composed of inputs, outputs and components. A model of such a system describes consistently (*i.e.* contradiction free) the components, their interrelationships and dependencies on inputs. A state can be assigned (*e.g.* mass, concentration, height, length) to each system component that contributes to the system's output. Therefore, for a given model with data on all required input quantities, a simulation can be performed and this provides a numerical realisation of the system in time and/or space.

Historically, many field and greenhouse experiments have been carried out to verify hypothesises about agricultural systems. However, the system was mostly treated as a 'black box' with no consideration being given to its components. Nowadays, statistical procedures that have been refined over the years to increase prediction accuracy and to be able to make more reliable inductions about the underlying real world or population from experimental results are available. For example, to aid prediction, statistical methods such as nonlinear regression, fuzzy logic or neuronal network procedures have evolved, and are able to represent very complex input - output relations.

So, why we should seek for a deeper understanding of system's internals, and thereby make the 'black box' more transparent and comprehensible? Some arguments for a wider application of a system analysis approach in agricultural science are:

- The obtained deeper understanding of the system enables faster research progress.
- Process models are becoming increasingly available (*e.g.* energy and radiation transfer of plant canopies, non-stressed leaf photosynthesis of C_3 - plants, canopy photosynthesis, water and heat transfer in soils) that can be used for abstraction and description of some system components.
- Prior obtained knowledge can be partly integrated into the system abstraction (type of system components and their relationships, process models, known parameters) while the inclusion of such information into classical statistical procedures (analysis of variance, regression) is difficult (*e.g.* Bayesian approach).
- A survey or experiment on the system under study with classical statistical methods may not be always feasible in terms of costs, risks or practicality.
- A prediction of the system's output will frequently occur at input occasions (scenarios) that were not included during the estimation of the statistical model.
- The system under consideration has to be optimised under a multitude of input variations.
- During application or simulation, information about the state of the system, which might be not easily observable (*e.g.* soil state variables), could be obtained.

Several research stages are typically encountered when using the methods from system analysis and mathematical modelling. First, the system has to be identified, *i.e.* the essential components and their relations to the environment as well as their interrelations are to be defined from previous work, experiments or theoretical considerations. This stage or task is characterised by available system inputs and outputs, but a largely unknown system structure. The process of system identification itself is related to the second task of parameter identification, *i.e.* parameters with unknown values are estimated from the system's output (measurements). As this can be very demanding and difficult for large models in terms of number of parameters to be identified, it is preferable to estimate parameters from single process behaviour if possible. Whereas system and parameter identification are typical for the research stage of model development, the final task of model prediction has a clear industrial or research application. Yet another applied field emerges from optimal control studies.

Here, the system output is provided and a consistent input and/or specific parameter values are identified. Therefore, identified and parameterised systems which can be controlled at least partly (*e.g.* growing crops under greenhouse conditions) are amenable to computational optimisation.

This thesis considers a number of problems for a specific class of systems often encountered in agriculture called Soil-Vegetation-Atmosphere Transport Models (SVAT). In short, these models calculate the fluxes of energy and matter (*e.g.* heat, H_2O, CO_2) between the soil, the canopy and the atmosphere over several days or months. Research on these kind of models has been performed since the 1940s. Hence, there is already extensive knowledge in this area and several software implementations of SVAT models are now available. However, a general application of SVAT models to a range of agricultural scenarios requires parameter sets for the most commonly encountered soils and economically important crops. As the behaviour of soils is almost static, it is not surprising that research on "pedo-transfer functions" providing predictions of soil parameters (*e.g.* saturated hydraulic conductivity) based on simple soil properties (soil texture, humus content, bulk density) was the first to be ongoing. Similarly, one may define other crop related transfer functions for the emerging class of models that predict important SVAT model parameters from simple stand properties (*e.g.* canopy height, Leaf Area Index, total aboveground nitrogen content, mean specific leaf weight).

In the first part of this thesis, a generally applicable "aero-transfer function" framework is derived for aerodynamic vegetation parameters that are used for turbulent transport computations over and within plant canopies. The derivation is based on published data sets and theoretical arguments. Moreover, on some occasions, the usage of some parameters in turbulent transfer calculations is refined. The suggested improvements should contribute to increased overall precision of sensible and latent heat flux calculations if one SVAT model is applied to various vegetation types.

The second part considers a SVAT model with no vegetation. A very detailed energy balance model for agricultural fields containing soil ridges partly covered by plastic

mulches is developed. Special emphasis is given to the modelling of radiation interception from short-wave and long-wave radiation sources and the directional response of transmission and reflection of radiation of plastics. As a result, the energy balance of the ridge surface can be calculated more thoroughly and was linked to a two-dimensional soil model (2DSOIL, TIMLIN *et al.*, 1996). As the simulated system is a two-dimensional soil column, this body of work could be described as input modelling. The technical implementation of model coupling and simulation was performed within the Compaq Visual Fortran programming environment. A simulation of the overall model provides time series of soil temperatures and water contents at spatial locations the user is interested in. All required inputs for simulation are:

- a geometric description of soil ridge shape
- radiation properties of applied plastic mulches (transmission and reflection for short-wave and long-wave radiation)
- standard thermal and hydrological soil parameters
- depth of the water table
- hourly weather station data

The final part of this thesis concerns the steps of calibration or parameter identification and overall model validation of the proposed simulation model. For this task, extensive measurements of soil temperature were taken at two sites and for six soil–plastic mulch treatments and compared to model simulations. The necessary parameters are derived from published pedo-transfer functions, additionally obtained data sets and, to a minor extent, from the validation data set.

The developed simulation model reported here could have several future applications. One application would be the development of a decision support system for growers of white asparagus. Such a system could provide information on the best current plastic-mulch cover types based on simulation conditioned on the actual goals of the grower (continuous, high, low or week day specific spear yield). Another field for further research would be an optimal control study using the identified system to optimise ridge shape, timing of ridge preparation and covering or the radiative properties of plastic

mulches.

This thesis was prepared from the following published work:

GRAEFE, J. (2004): Roughness layer corrections with emphasis on SVAT model applications. Agricultural and Forest Meteorology, 124, 237-251.

GRAEFE, J. (2005): Simulation of soil heating in ridges partly covered with plastic mulch, Part I: Energy balance model. Biosystems Engineering, 92, 391-407.

GRAEFE, J., SCHMIDT, S., HEIßNER, A., RUSIN, W., WONNEBERGER, C. (2005): Simulation of soil heating in ridges partly covered with plastic-mulch, Part II: Model calibration and validation. Biosystems Engineering, 92, 495-512.

Each chapter was provided with its own list of Symbols and Abbreviations as several scientific topics with a non-unique symbolisation are covered and in order to avoid confusion.

2 Roughness layer corrections with emphasis on SVAT model applications

List of Symbols and Abbreviations

$a(z)$	leaf area density function with height	$m^2\ m^{-3}$
c_d	drag coefficient	
C_r	canopy drag coefficient	
C_s	substrate drag coefficient	
d	zero plane displacement	m
D	inter-element spacing between roughness elements	m
f_{cr}	crown height to canopy height ratio	
H	sensible heat flux	$W\ m^{-2}$
h_c	canopy height	m
h_{ci}	critical canopy height	m
k	von Kármán's constant (0.4)	
K_m	turbulent diffusivity for momentum	$m^2\ s^{-1}$
K_s	turbulent diffusivity for scalars (H_2O, CO_2)	$m^2\ s^{-1}$
L	Obukhov length scale	m
L_s	canopy length scale $u(h_c)/(du/dz)$	m
L_t	Plant Area Index (*PAI*)	$m^2\ m^{-2}$
M_{SC}	Model Selection Criterion	
PAI	Plant Area Index	$m^2\ m^{-2}$
Pr	turbulent Prandtl number	
r_a	aerodynamic resistance, turbulent transfer resistance	$s\ m^{-1}$
r_b	boundary layer resistance	$s\ m^{-1}$

$RMSE$	root mean square error	
T_L	Lagrangian time scale	s
u	mean horizontal wind speed	m s^{-1}
u_*	friction velocity	m s^{-1}
z	vertical coordinate, height	m
$z_{0,m}$	roughness length for momentum	m
$z_{0,s}$	roughness length for scalars	m
Z_{m*}	height of the roughness layer for momentum	m
z_r	reference height for momentum or scalar exchange	m
z_{so}	source height	m
Z_{s*}	height of the roughness layer for scalars	m
α	extinction parameter for canopy wind speed	
$\varepsilon_m(z)$	enhancement function for momentum diffusivities	
$\varepsilon_s(z)$	enhancement function for scalar diffusivities	
γ	inverse square root of canopy drag $u(h_c)/u_*$	
η	empirical parameter	
λ	horizontal projected leaf area per unit ground area	m^2 m^{-2}
σ_w	standard deviation of vertical component of wind speed	m s^{-1}
φ_m	universal stability function for momentum	
φ_s	universal stability function for scalars	
$\Psi_h(z_1, z_2)$	momentum roughness layer correction function	
$\Psi_{h'}$	momentum roughness layer correction parameter	
Ψ_m	integrated universal stability function for momentum	
Ψ_{m*}	integrated stability and roughness function for momentum	

Ψ_s integrated universal stability function for scalars

Ψ_{s*} integrated stability and roughness function for scalars

2.1 Introduction

The exchange of momentum and scalars between vegetation and the atmosphere is of great importance in related modelling projects and experiments. Most momentum transfer models and applications still rely on use of one-dimensional approaches, such as the semi-logarithmic wind speed law, which follows from the Obukhov similarity theory. However, even in computations of scalar transfer with more sophisticated Lagrangian models some input is needed from one-dimensional momentum transfer theory (friction velocity u_*, zero plane displacement d, RAUPACH, 1987).

Parameters, such as the zero plane displacement, the roughness length for momentum ($z_{0,m}$) are usually estimated from principal biophysical characteristics of the ground cover, such as canopy height (h_c), Plant Area Index (PAI), or its horizontal projection – the frontal area index (λ) (RAUPACH, 1992; VERHOEF *et al.,* 1997). These aerodynamic transfer functions are of fundamental importance for a broad range of applications that deal with exchange processes between plant canopies and the atmosphere as well as the soil surface.

There are still some uncertainties regarding the estimation of d and $z_{0,m}$ from h_c and PAI. Moreover, the existence of a roughness sublayer that extends from canopy to the bottom of the inertial sublayer (GARRATT, 1980; RAUPACH *et al.,* 1980) requires additional parameters as the height of the roughness layer for momentum (Z_{m*}). So far, some roughness layer corrections have been made within predictive models for $z_{0,m}$ (RAUPACH, 1992) in terms of a constant correction parameter $\Psi_{h'}$. However, there has been no attempt to make an explicit canopy structure dependent parameterisation of the roughness layer.

Applications under a broad range of atmospheric conditions call for analytical solutions of the combined effect of roughness layer and stability in order to increase computational efficiency. While principal definitions were given in previous studies

(CELLIER & BRUNET, 1992; MÖLDER *et al.*, 1999; PHYSICK & GARRAT, 1995), closed analytical solutions for all stability cases have not yet been presented.

Figure 2.1 gives an overview about the quantities and the order of calculations of the proposed parameterisation scheme.

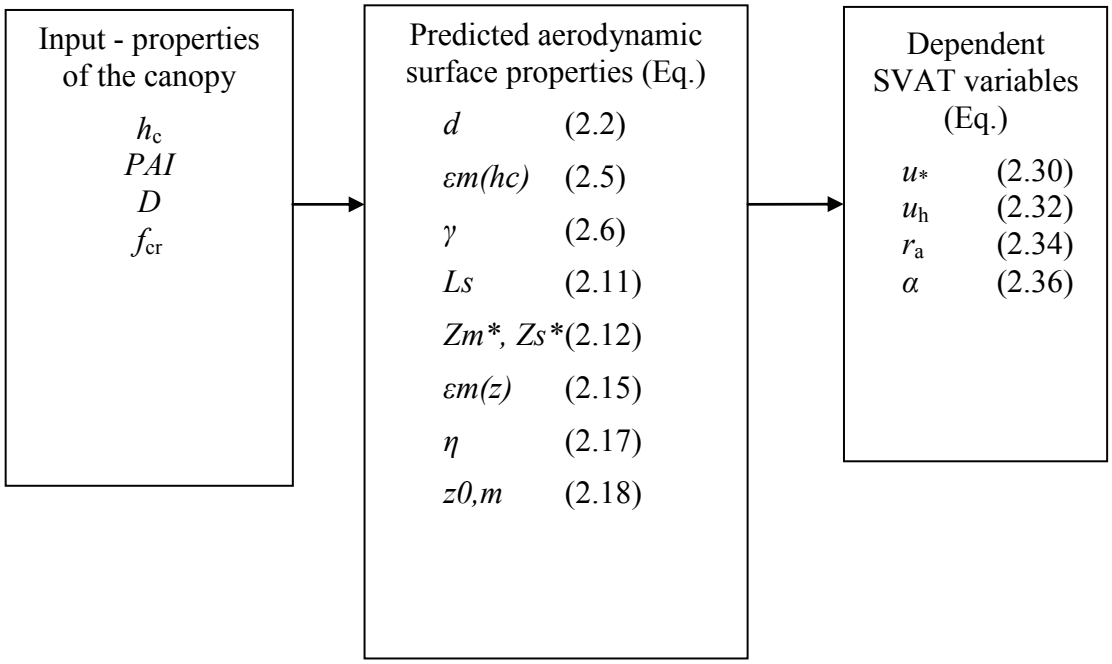

Fig. 2.1 Computed quantities as result of the parameterisation (equation numbers are in parentheses): h_c – canopy height, *PAI* – Plant Area Index, *D* – inter-element spacing between roughness elements, f_{cr} – crown thickness to canopy height ratio, *d* – zero plane displacement, γ - inverse square root of drag coefficient, L_s – length scale $u_h/(du/dz)$, Z_{m*} - roughness layer height for momentum, Z_{s*} - roughness layer height for scalars, $\varepsilon_m(z)$ – enhancement function of momentum diffusivity with height, $z_{0,m}$ – roughness length for momentum, u_* - friction velocity, u_h – horizontal wind speed at canopy height, r_a ¯ aerodynamic resistance, α – canopy wind speed extinction parameter

2.2 Description of the parameterisation

2.2.1 Data sets

Several data sets retrieved from the literature are summarised in Table 2.1. These were mainly drawn from data summaries of RAUPACH *et al.* (1980, 1991, 1996); VERHOEF *et al.* (1997), and GARRATT (1977) and were extended to include more records from agricultural crops, which were found to be under-represented. The main criterion was that single records had to provide information on h_c and *PAI* or λ and an aerodynamic quantity, such as d, $z_{0,m}$, L_s or ε_m ($z = h_c$).

Table 2.1 Data sets used from the literature (h_c – canopy height [m], D – inter-element spacing between roughness elements [m], λ – frontal area index, *PAI* – Plant Area Index; for across flow aligned thin strips: $PAI = \lambda$, plant canopies: $PAI = 2\,\lambda$, cylinders: $PAI = 1.57\,\lambda$, u_* - friction velocity, u_h – horizontal wind speed at canopy height, L_s – length scale $u_h/(\mathrm{d}u/\mathrm{d}z)$ [m], d – zero plane displacement [m], $z_{0,m}$ – roughness length for momentum [m], Z_{m*} - roughness layer height for momentum [m], Z_{s*} - roughness layer height for scalars [m], ε_m – enhancement factor of momentum diffusivities at canopy height, f_{cr} –crown thickness to canopy height ratio; guessed or estimated from vertical distribution of leaf area, WT –wind tunnel). Sources: 1-RAUPACH *et al.* (1996), 2-VERHOEF *et al.* (1997), 3-RAUPACH *et al.* (1991), 4-GARRATT (1977), 5-RAUPACH *et al.* (1980), 6-THOM (1971), 7-SOEGAARD (1999), 8-JACOBS & VAN BOXEL (1988), 9-CELLIER & BRUNET (1992), 10 – MÖLDER *et al.* (1999)

id	Surface	h_c	D	λ	PAI	u_h/u_*	L_s/h_c	d	$z_{0,m}$	Z_{m*}	Z_{s*} [a)]	ε_m [b)]	f_{cr}	Source
1	WT strips	0.060	0.044	0.23	0.23	3.3	0.85	0.043	0.0087	0.128		2.22	1	1
2	WT wheat	0.047		0.47	0.738	3.31[c)]	0.81[c)]	0.033	0.0056	0.087		2.09	1	1
3	WT rods	0.19		1	1.57	5	0.49	0.140	0.0067			0.91	1	1
4	Corn	2.6		1.5	3	3.6	0.39					1.12	1	1
5	Corn	2.25		1.45	2.9	3.2	0.46					1.46	1	1
6	Eucalypt forest	12		0.5	1	2.9	0.58					1.86	1	1
7	Pine forest	20		2.05	4.1	2.5	0.29					1.6	0.7	1
8	Aspen forest	10		1.95	3.9	2.6	0.58					2.82	0.9	1
9	Pine forest	15		1	2	2.2	0.50					2.55	0.7	1
10	Spruce forest	12		5	10	2.4	0.44					3.02	0.6	1
11	Spruce forest	12		5.1	10.2	4	0.30	10.125	1.1			1.17	0.7	1
12	Deciduous	24		2.5	5	2.8	0.12	21.6		33.6[d)]		1.045	0.35	1
13	Pine/spruce	24.5		2.5	5	3.2	0.43	21.1		45	57	2.38	0.7	10
14	Savannah	2.3	5	0.32	0.64			1.8	0.435	10	10	2	1	2
15	Savannah	8	20	0.03	0.06			4.8	0.4	64.8	44.8	1.76	1	2
16	Savannah	9.5	10	0.2	0.4			7.1	0.9	37.1		2.13	1	2
17	Savannah	2.5	6.6	0.17	0.34			1.5	0.25				1	2
18	Tiger-bush	4	40	0.05	0.1			2	0.44				1	2
19	Vineyard	0.9	2.5	0.13	0.26			0.31	0.08				1	2
20	Cotton	0.49	1	0.19	0.38			0.31	0.066				1	2
21	Vineyard	1.5	1.75	0.15	0.3			0.75	0.2				1	2
22	Forest	10		2.8	5.6	3.8		7.6	0.5				0.7	3
23	Forest	22		3.1	6.2	2.9		19.8	0.66				0.7	3
24	Forest	15.5		4.3	8.6	3.3		11.8	0.93				0.7	3
25	Forest	4.5		0.8	1.6	2.9		3	0.45				0.7	3
26	Forest	23		1.7	3.4	3.1		19.1	1.15				0.7	3
27	Forest	11.5		9.6	19.2	3.4		9.7	0.35				0.7	3
28	Early Wheat	0.4	0.2	0.1	0.2				0.015				1	4
29	Late Wheat	1	0.2	0.25	0.5				0.05				1	4
30	Pine forest	13	2.4	2.3	4.6				0.4				1	4
31	Vineyard	0.4	2.5	0.22	0.44				0.12				1	4
32	WT Cylinder	0.006	0.057	0.011	0.0173			0.001	0.000054	0.015		2.5	1	5
33	WT Cylinder	0.006	0.040	0.023	0.0361			0.002	0.000144	0.016		3.04	1	5
34	WT Cylinder	0.006	0.028	0.045	0.0706			0.003	0.000214	0.014		3.06	1	5
35	WT Cylinder	0.006	0.020	0.091	0.1428			0.004	0.000346	0.013		3.46	1	5
36	WT Cylinder	0.006	0.014	0.179	0.2810			0.005	0.000395	0.015		6.25	1	5
37	WT Cylinder	0.143	0.010	1.42	2.2292			0.109	0.0135	0.173		1.33	1	6
38	Beans	1.18		3.1	6.2			0.885	0.0758				1	6
39	Barley	0.34		1.4	2.8			0.272	0.036				1	7
40	Wheat	1.1		2.75	5.5			0.847	0.08				1	7
41	Corn	2		1.5	3			1.540	0.115				1	8
42	Corn	2.35		1.7	3.4					5.16	5.16	2	1	9

[a)] as given or estimated from height where inertial layer diffusivities matches measured (records 1+2)

[b)] calculated from h_c, d, u_h/u_* and L_s/h_c (records 1-12, see Eq. 2.5), calculated from h_c, d, Z_{m*} and η at $z = h_c$ (record 13: $\eta = 0.6$ record 42: $\eta = 0.45$, records 32-37: $\eta = 1$), calculated from $1/\alpha_1$ (records 15 + 16) see GARRATT (1980)

[c)] calculated from given u_h and u_* or estimated from mean wind profile as given in primary source (BRUNET *et al.,* 1994)

[d] estimated from vertical profile of r_{uw} and the condition $|r_{uw}(Z_{m*})| \sim 0.3$

2.2.2 Zero plane displacement

This parameter describes the effective aerodynamic origin of a rough surface. A physical interpretation was given by THOM (1971) as d being the height of the centre of pressure of the drag forces acting on a surface including the drag on the soil surface. Various models for d have been proposed on the basis of h_c and PAI or λ. The most reliable models - being partly physically based - have been developed from drag partition theory (RAUPACH, 1992, 1994, 1995; VERHOEF *et al.*, 1997), higher order closure canopy wind flow models (SHAW & PEREIRA, 1982), and by the use of Thom's interpretation (MASSMAN, 1996).

Here the empirical model of RAUPACH (1994) with the parameterisation of VERHOEF *et al.* (1997) is used for comparison:

$$\frac{d}{h_c} = 1 - \frac{1 - \exp(-\sqrt{10.5\,L_t})}{\sqrt{10.5\,L_t}} \tag{2.1}$$

where PAI (L_t) is used instead of λ – the so-called frontal area index, which is the projected leaf area on a plane normal to the wind flow. To a good approximation for plant canopies $PAI = 2\lambda$. PAI is selected because it does not rely on a detailed geometrical description of leaf (and other plant organs) angle distributions. An empirical modification of Eq. (2.1) is:

$$\frac{d}{h_c} = 1 - \frac{1 - \exp(-(x\,L_t)^{0.25})}{(x\,L_t)^{0.25}} \qquad x = 107.5\,h_c^{\,0.363} + 20.6\,\frac{L_t}{h_c} - 74.8 \tag{2.2}$$

where it was preferred to fit Eqs. (2.1) – (2.2) on d/h_c rather on d. The new model yields a coefficient of determination (R^2) of 82% and a $RMSE$ of 0.076, compared with 44% and 0.133 when using Eq. (2.1) (see Fig. 2.2).

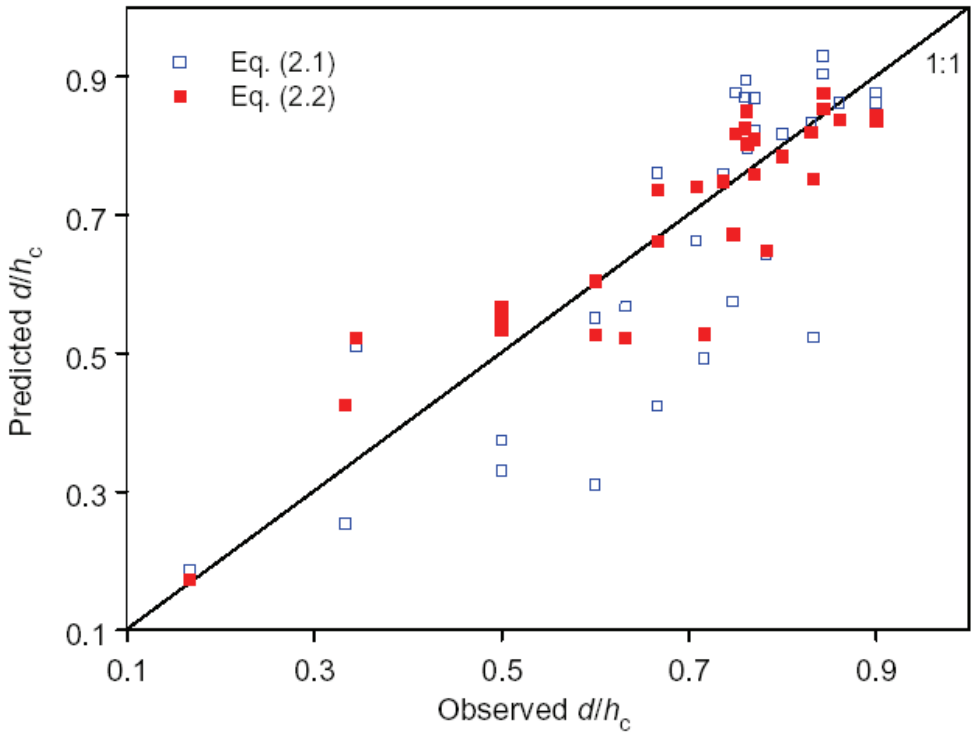

Fig. 2.2 Comparison of predicted and observed d/h_c using a new (Eq. (2.2)) and a previous (Eq. (2.1)) suggested model and data from the literature as given in Table 2.1. Statistical details of comparison are: n = 30; Eq. (2): R^2 = 82%, $RMSE$ = 0.07.6, M_{SC} = 1.363; Eq. (1): R^2 = 44%, $RMSE$ = 0.133, M_{SC} = 0.515 (d – zero plane displacement, h_c – canopy height, $RMSE$ – root mean square error, M_{SC} – Model Selection Criterion).

To check whether this extra complexity of Eq. (2.2) (3 parameters more) is justified, the Model Selection Criterion (M_{SC}, AKAIKE, 1976) was calculated as:

$$M_{SC} = \ln\left[\frac{\sum_{i=1}^{n}\left(\frac{d_{obs_i}}{h_{c_i}} - \overline{\left(\frac{d_{obs_i}}{h_{c_i}}\right)}\right)^2}{\sum_{i=1}^{n}\left(\frac{d_{obs_i}}{h_{c_i}} - \frac{d_{calc_i}}{h_{c_i}}\right)^2}\right] - \frac{2p}{n} \qquad (2.3)$$

where d_{obs} and d_{calc} stand for observations and calculations, respectively, whereas p and n are the number of parameter and observations, respectively. The M_{SC} was 1.36 and 0.51 for Eqs. (2.2) and (2.1), respectively. Therefore, the usage of Eq. (2.2) is justified,

as the equation with the highest M_{SC} is the preferred equation, independently of the number of parameters.

2.2.3 Length scale L_s

RAUPACH *et al*. (1996) showed that turbulence in and just above plant canopies is better described by a mixing layer analogy than by the common surface layer similarity theory. They concluded that the length scale L_s is an important aerodynamic property of plant canopies and is given by $L_s = u(h_c)/(\mathrm{d}u/\mathrm{d}z)$. Some quantities are thought to depend directly on L_s, such as the height of the roughness layer for momentum and scalars, which have been expressed as $Z_{m*} = h_c + cL_s$, where c denotes a constant (VERHOEF *et al*., 1997). Moreover, a relation to the enhancement of momentum transfer at canopy height itself can be deduced from the definition of the wind speed gradient at the canopy top:

$$\frac{\mathrm{d}u}{\mathrm{d}z} = \frac{u_*}{k\,(h_c - d)\,\varepsilon_m(z)} \tag{2.4}$$

with friction velocity u_*, von Kármán's constant k, and enhancement function $\varepsilon_m(z)$. Writing $\gamma = u_h/u_*$ (γ - inverse square root of the bulk drag coefficient at canopy height), the enhancement of momentum transfer at canopy height can be written as

$$\varepsilon_m(h_c) = \frac{L_s}{k\,(h_c - d)\,\gamma} \tag{2.5}$$

while γ may be estimated via an expression given by RAUPACH (1994):

$$\gamma = \max\left[(C_s + C_r\,L_t)^{-0.5}, 1/0.3\right] \tag{2.6}$$

with soil or substrate drag coefficient C_s (0.003) and canopy drag coefficient C_r (0.15).

Experimental records given by RAUPACH *et al*. (1996) and MÖLDER *et al*. (1999) were used to develop an empirical expression for L_s. To use a physically sound base term, the

differential equation of horizontal wind speed within the canopy derived from first order K- closure (RAUPACH & THOM, 1981)

$$\frac{\partial K_m}{\partial z}\frac{\partial u}{\partial z} + K_m \frac{\partial^2 u}{\partial z^2} = c_d\, a(z)\, u^2$$
$$K_m = u_* \, k\,(z-d) \tag{2.7}$$

with leaf drag coefficient c_d, leaf area density $a(z)$ and diffusivity for momentum K_m was related to L_s. The enhancement factor ε_m was omitted from the K_m formulation, otherwise L_s would cancel out. As L_s is defined at the inflexion point of the wind profile, which will occur roughly at canopy top (RAUPACH *et al.*, 1996), the second derivative term was neglected in Eq. (2.7). Substituting $L_s = u_h/(\mathrm{d}u/\mathrm{d}z)$ and $\gamma = u_h/u_*$ into Eq. (2.7) yields the following relation at $z = h_c$:

$$\frac{L_s}{h_c} \sim \frac{1}{\gamma\, a_{top}\, h_c} \tag{2.8}$$

where a_{top} denotes leaf area density in the upper part of the canopy. This quantity is usually not known, but as most canopies have a nearly linear leaf area density distribution with a vertical maximum between 40 - 60% of the height of the leafed sub volume (*i.e.* the crown; AMIRO, 1990; DENMEAD, 1976; RAUNER, 1976; RIPLEY & REDMANN, 1976; SAUGIER, 1976) a simplification may be possible. Thus, assuming a triangular leaf area distribution (PEREIRA & SHAW, 1980) with a maximum at 50% of crown depth, the leaf area density at some upper height $z' = c\,(h_c - d)$ is given as (z' is counted from h_c):

$$a_{top} = a(c(h_c - d)) = \frac{L_t\, c\,(h_c - d)}{\left(h_c\, f_{cr}\, 0.5\right)^2} \sim \frac{L_t\,(h_c - d)}{\left(h_c\, f_{cr}\right)^2} \tag{2.9}$$

with the crown thickness to canopy height ratio f_{cr}. Using Eqs. (2.8), (2.9) and introducing two parameters (a, b) the following function was fitted to observed L_s/h_c:

$$\frac{L_s}{h_c}=\left(\frac{a\,f_{cr}{}^2\,h_c}{\gamma\,L_t\left(h_c-d\right)}\right)^b \qquad a=0.219\;\; b=0.317 \tag{2.10}$$

Predicted versus observed L_s/h_c are shown in Fig. 2.3.

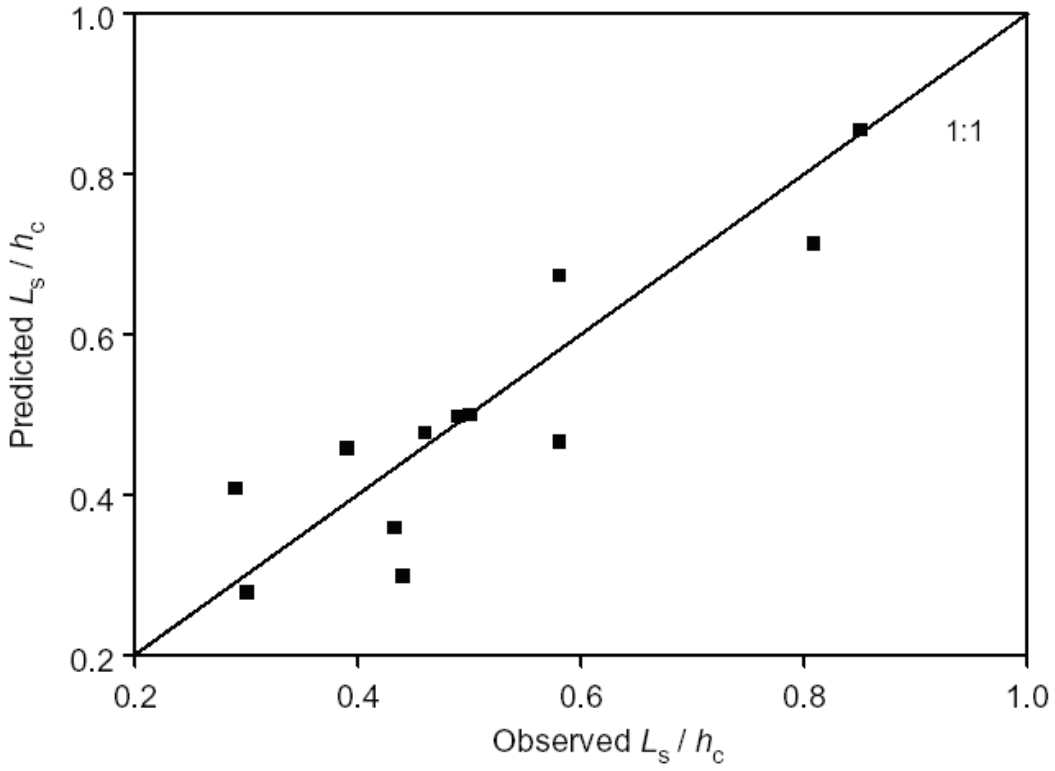

Fig. 2.3 Observed versus predicted L_s/h_c using Eq. (2.10). n = 13, R^2 = 81%, *RMSE* = 0.087 ($L_s = u(h_c)/(\mathrm{d}u/\mathrm{d}z)$, h_c – canopy height, u – horizontal wind speed, *RMSE* – root mean square error).

Unfortunately, there are no observations of L_s/h_c for widely spaced canopies, which are characterised by $D/h_c >> 0$, with D being the inter-element spacing of roughness elements (row distance, mean distance between trees). Provided that Eq. (2.5) is still valid under these conditions and that predictions of d and γ are reliable, observed enhancements of momentum diffusivity for those canopies may be used to solve Eq. (2.5) for an "observed" $L_{s,o}$. The resulting deviation ($\Delta L_s = (L_{s,o} - L_s)/h_c$) from predictions of Eq. (2.10) was found to be significant and was parameterised with a linear equation in D/h_c, which is illustrated together with "observed" deviations of L_s/h_c from

predictions of Eq. (2.10) in Fig. 2.4. The modified equation for L_s/h_c is:

$$\frac{L_s}{h_c} = \left(\frac{0.219 f_{cr}^{\,2} h_c}{\gamma L_t \left(h_c - d \right)} \right)^{0.32} + \begin{cases} 1.18 D/h_c - 1.18 & D/h_c > 1 \\ 0 & D/h_c \le 1 \end{cases} \tag{2.11}$$

It can be seen from Fig. 2.4 that for canopies with relative spacing (D/h_c) lower 1 deviations can be neglected whereas larger spacing induce significant errors.

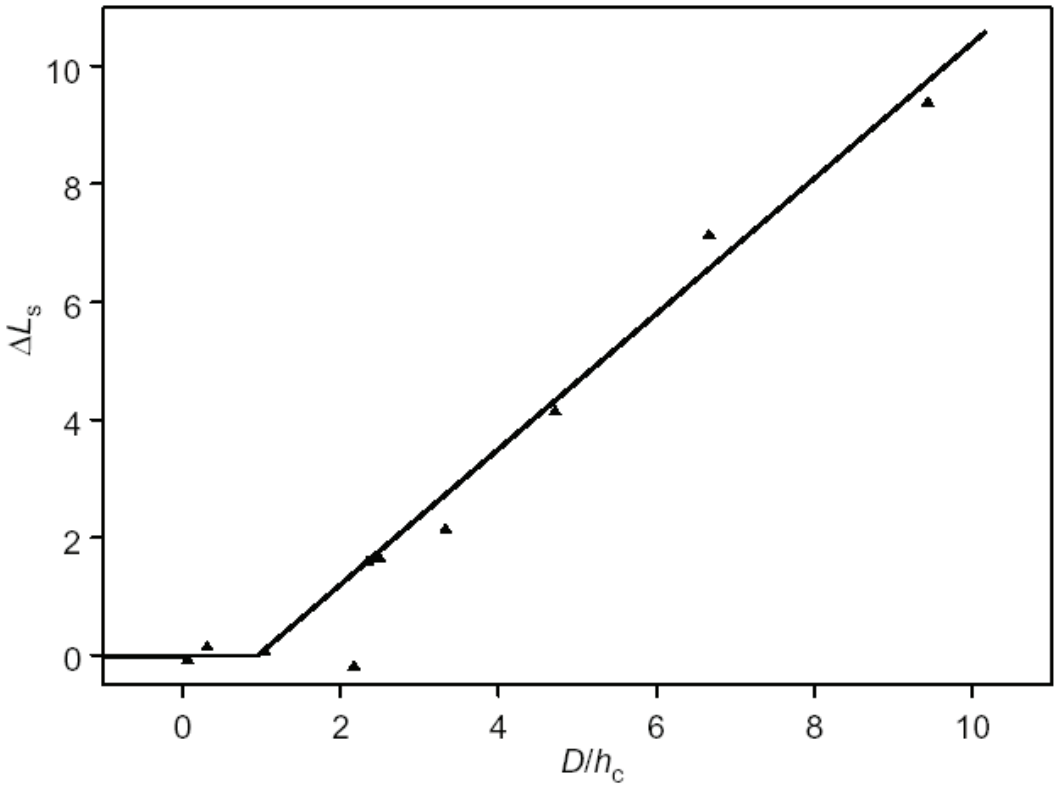

Fig. 2.4 Observed deviations $\Delta L_s = (L_{s,o} - L_s)/h_c$ in relation to relative spacing D/h_c together with a fitted linear function (compare Eqs. (2.10) and (2.11), $L_s = u(h_c)/(\mathrm{d}u/\mathrm{dz})$, h_c – canopy height, D – inter-element spacing, u – horizontal wind speed).

2.2.4 Height of the roughness layer

Several relationships have been proposed for the height of the roughness layer for momentum. The most recent view (RAUPACH *et al.*, 1996, VERHOEF *et al.*, 1997) suggests a linear relation to the length scale L_s such as $Z_{m*} = h_c + cL_s$ (with c = 2..3).

MÖLDER *et al.* (1999) determined $c \sim 2$ for a spruce forest. For low and sparse canopies RAUPACH *et al.* (1991) proposed a multiple of canopy height: $Z_{m*} = 2h_c$. The available empirical information, as listed in Table 2.1, was approximated with two relations (Fig. 2.5):

$$Z_{m*} = \begin{cases} h_c + 2.32\,L_s & h_c > h_{ci} \\ 2.42\,\min(L_s, h_c) & h_c \le h_{ci} \end{cases} \qquad (2.12)$$

$$Z_{s*} = h_c + 2.32\,L_s$$

where the critical canopy height h_{ci} (~1.7) and Z_{s*} are roughly guessed here as they cannot be precisely estimated from available data. The length scale L_s was given for the canopies of the two forests and the wind tunnel studies of RAUPACH *et al.* (1986) and BRUNET *et al.* (1994); otherwise it was calculated using Eq. (2.11).

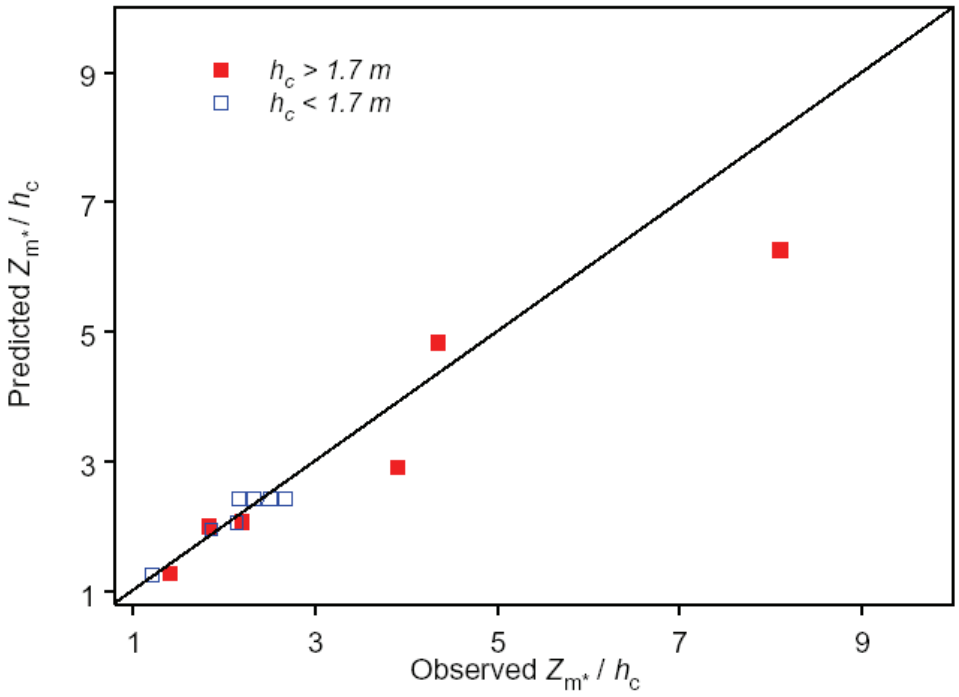

Fig. 2.5 Observed (Table 2.1) versus predicted height of roughness layer for momentum (Z_{m*}) from Eq. (2.12) for "tall" canopies with canopy heights $h_c > 1.7$ m and "short" canopies with $h_c < 1.7$ m.

Direct estimations of Z_{m*} by GARRAT (1980, 1983) indicate, that under stable conditions

Z_{m*} is strongly reduced whereas unstable conditions have no effect. Following PHYSICK & GARRAT (1995) this response may be expressed as:

$$Z'_{m_*,s_*} = \begin{cases} Z_{m_*,s_*} & L < 0 \\ Z_{m_*,s_*}\left(1 - 0.63(Z_{m_*,s_*} - d)/0.2L\right) & 0 < (Z_{m_*,s_*} - d)/L < 0.2 \\ 0.37 Z_{m_*,s_*} & (Z_{m_*,s_*} - d)/L \geq 0.2 \end{cases} \tag{2.13}$$

2.2.5 Choice of profile function

Several functions have been proposed to describe the vertical profile of momentum diffusivity enhancement throughout the roughness layer. GARRAT (1980) proposed an exponential equation of the form:

$$\varepsilon_m(z) = \frac{1}{\exp\left(\alpha\left(1 - \frac{z-d}{Z_{m*}-d}\right)\right)} \tag{2.14}$$

whereas CELLIER & BRUNET (1992) suggested the following function:

$$\varepsilon_m(z) = \left(\frac{Z_{m*}-d}{z-d}\right)^{\eta} \quad \eta = 0...1 \tag{2.15}$$

which is a more general form of the approach of RAUPACH *et al.* (1980) to model momentum diffusivities being constant throughout the roughness layer (η = 1). The measurement of such profiles is costly and difficult, so there are not enough direct results to judge or even develop a function. However, it is argued that observations of momentum roughness length ($z_{0,m}$) can be used to verify different profile functions of momentum diffusivity enhancement. Using Eqs. (2.14) and (2.15) α and η can be determined from Z_{m*} and $\varepsilon_m(h_c)$ according to:

$$\alpha = \ln(\varepsilon_m(h_c)^{-1})\frac{Z_{m*}-d}{Z_{m*}-h_c} \tag{2.16}$$

$$\eta = \ln(\varepsilon_{\mathrm{m}}(h_{\mathrm{c}})) / \ln\left(\frac{Z_{\mathrm{m}*} - d}{h_{\mathrm{c}} - d}\right) \tag{2.17}$$

where estimates of η will be forced to values in (0, 1]. The relation to the roughness length for momentum $z_{0,\mathrm{m}}$ is derived from integration of the logarithmic wind speed profile (Eq. (2.4)).

$$z_{0,\mathrm{m}} = \frac{h_{\mathrm{c}} - d}{\exp\left(k\gamma + \Psi_{\mathrm{h}}(h_{\mathrm{c}}) - \Psi_{\mathrm{h}}(Z_{\mathrm{m}*})\right)} \qquad \Psi_{\mathrm{h}}(z) = \int \frac{1 - \varepsilon_{\mathrm{m}}(z)^{-1}}{z - d}\, dz \tag{2.18}$$

Equation (2.18) was already given by RAUPACH (1992) and VERHOEF *et al.* (1997), but with a constant roughness layer influence function ($\Psi_{\mathrm{h}'} = \Psi_{\mathrm{h}}(Z_{\mathrm{m}*}) - \Psi_{\mathrm{h}}(h_{\mathrm{c}}) = 0.2$), that was derived using constant diffusivities ($\eta = 1$) throughout the roughness layer and a prognostic equation for $Z_{\mathrm{m}*} = c_{\mathrm{w}}(h_{\mathrm{c}} - d) + d$ (with $c_{\mathrm{w}} = 2$). $\Psi_{\mathrm{h}}(z)$ must be numerically solved for Eq. (2.14), whereas for Eq. (2.15) the result is:

$$\Psi_{\mathrm{h}}(z) = -\ln\left(\frac{Z_{\mathrm{m}*} - d}{z - d}\right) - \left(\frac{Z_{\mathrm{m}*} - d}{z - d}\right)^{-\eta} / \eta \tag{2.19}$$

There are 31 observations of $z_{0,\mathrm{m}}$ over a large range of canopies to compare with (see Table 2.1). As the sensitivity of $z_{0,\mathrm{m}}$ on Ψ_{h}' is rather low (RAUPACH, 1995) all available inputs (d, $\varepsilon_{\mathrm{m}}(h_{\mathrm{c}})$, γ, L_{s}, $Z_{\mathrm{m}*}$) were used if given to predict $z_{0,\mathrm{m}}$ from Eq. (2.18), but otherwise calculated via Eqs. (2.2), (2.5), (2.6), (2.11) and (2.12). The comparison between predicted and observed $z_{0,\mathrm{m}}/h_{\mathrm{c}}$ resulted in *RMSEs* of 0.049 and 0.037 for the proposed profile functions of GARRAT (1980) and CELLIER & BRUNET (1992) (Eqs. (2.14), (2.15)). The exponential expression has been used for sparse canopies with a significant inter-element spacing D (GARRATT, 1980), but even analysis of a subset of canopies with $D/h_{\mathrm{c}} > 0.5$ ($n = 14$) revealed no advantages compared with Eq. (2.15) with *RMSEs* of 0.061 and 0.046 for Eqs. (2.14) and (2.15), respectively.

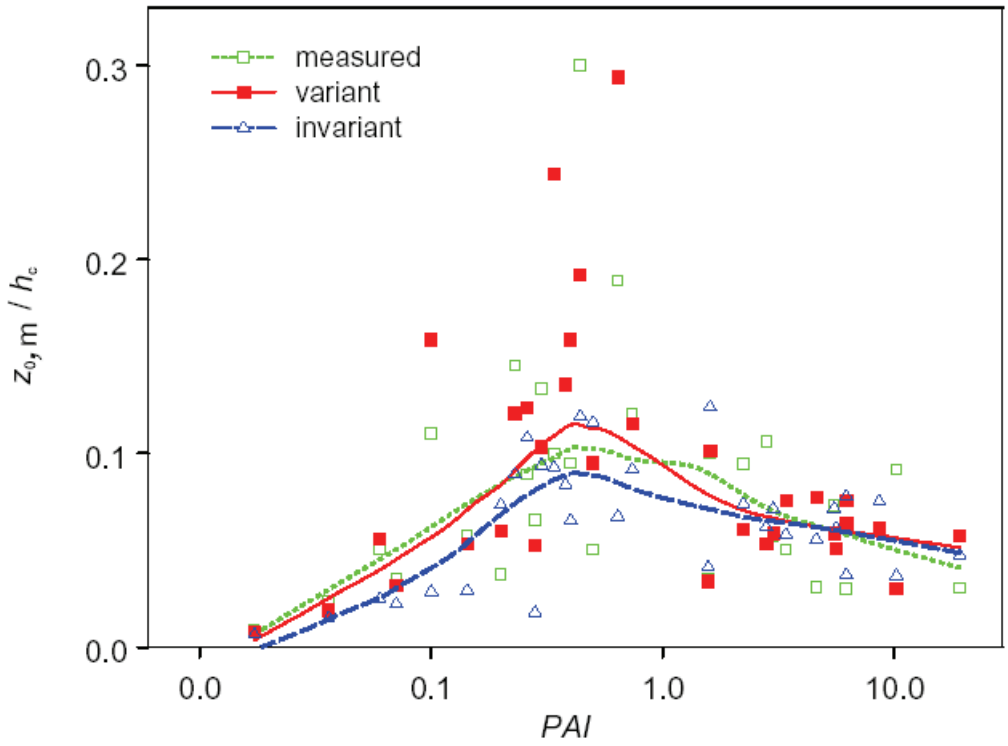

Fig. 2.6 Predicted and observed normalised roughness lengths for momentum $z_{0,m}/h_c$ versus PAI together with smoothing functions using Ψ_h terms that are variant or invariant to canopy structure defined by *PAI*, h_c, and *D* (*PAI* – Plant Area Index, h_c – canopy height, *D* – inter-element spacing).

Next, using only *PAI*, h_c and *D* as inputs and Eq. (2.15) resulted in a better prediction of $z_{0,m}/h_c$ compared with estimations using a constant Ψ_h'= 0.2. The *RMSEs* were 0.04 and 0.049, respectively and the R^2 was 50% , compared with 26% when using Ψ_h'= 0.2. An overall comparison of predicted and observed $z_{0,m}$, together with estimated trends (symmetric loess algorithm, MATHSOFT, 2001) is presented in Fig. 2.6. For sparse canopies (*PAI* < 1), there is a systematic underestimation of $z_{0,m}/h_c$ by the model of VERHEOF *et al.* (1997). The mean predicted Ψ_h' using Eq. (2.19) would be for sparse canopies 0.55 and for other cases 0.252.

It was observed that the enhancement profile of scalar diffusivity within the roughness layer is well described by Eq. (2.15) with η = 1 (CELLIER & BRUNET, 1992, MÖLDER *et al.*, 1999) such as:

$$\varepsilon_s(z) = \frac{Z_{s*} - d}{z - d} \tag{2.20}$$

and this expression will be adopted here.

2.3 Derivation of the integrated functions

Some studies have considered both roughness layer and atmospheric stability effects in a combined description of wind and scalar profiles (CELLIER & BRUNET, 1992; MÖLDER *et al.*, 1999; PHYSIK & GARRATT, 1995). If both processes are treated independently, the appropriate relations can be stated easily (CELLIER & BRUNET, 1992), but so far no integrated combined stability/roughness functions have been derived for each stability regime.

Using the roughness layer profile functions for momentum (Eq. 2.15) and scalars (Eq. 2.20) together with the universal stability functions φ_m and φ_s recommended by HÖGSTRÖM (1996)

$$\varphi_s(z,L) = \begin{cases} (1-\gamma_{s,u}\,\zeta)^{-0.5} & L<0 \\ (1+\gamma_{s,s}\,\zeta) & L>0 \end{cases} \qquad \zeta = \frac{z-d}{L},\ \gamma_{s,u}=11.6,\ \gamma_{s,s}=8 \tag{2.21}$$

$$\varphi_m(z,L) = \begin{cases} (1-\gamma_{m,u}\,\zeta)^{-0.25} & L<0 \\ (1+\gamma_{m,s}\,\zeta) & L>0 \end{cases} \qquad \zeta = \frac{z-d}{L},\ \gamma_{m,u}=19,\ \gamma_{m,s}=5.3 \tag{2.22}$$

various integrations have been done. The integrated universal functions ($\Psi_{s/m}$) for scalars and momentum, which apply in the inertial layer are defined by:

$$\Psi_{s/m} = \int \frac{1-\varphi_{s/m}(z,L)}{z-d}\,dz \tag{2.23}$$

where integration yielded

$$\Psi_{\mathrm{s}}(z,L) = \begin{cases} \ln(z-d) + 2\,\mathrm{arctanh}\left[\left(1-\gamma_{\mathrm{s,u}}\,\dfrac{z-d}{L}\right)^{0.5}\right] & L<0 \\ -\gamma_{\mathrm{s,s}}\,\dfrac{z}{L} & L>0 \end{cases} \tag{2.24}$$

$$\Psi_{\mathrm{m}}(z,L) = \begin{cases} \ln(z-d) - 2\arctan(x) - \ln\left(\dfrac{x-1}{1+x}\right) & L<0 \\ -\gamma_{\mathrm{m,s}}\,\dfrac{z}{L} & L>0 \end{cases} \tag{2.25}$$

$$x = \left(1-\gamma_{\mathrm{m,u}}\,\frac{z-d}{L}\right)^{0.25}$$

Similarly, assuming independence of stability and roughness layer effects, the integration of the combined stability/roughness response was done according to:

$$\Psi_{\mathrm{s*/m*}} = \int \frac{1-\varphi_{\mathrm{s/m}}(z,L)\,\varepsilon_{\mathrm{s/m}}(z)^{-1}}{z-d}\,dz \tag{2.26}$$

and the result, which is valid for the roughness layer is

$$\Psi_{\mathrm{s*}}(z,L) = \begin{cases} \ln(z-d) + \dfrac{2L}{(Z_{\mathrm{s*}}-d)\,\gamma_{\mathrm{s,u}}}\left(1-\gamma_{\mathrm{s,u}}\,\dfrac{z-d}{L}\right)^{0.5} & L<0 \\ \dfrac{(zd-0.5z^2)\gamma_{s,s}/L - z}{Z_{\mathrm{s*}}-d} + \ln(z-d) & L>0 \\ \ln(z-d) - \dfrac{z}{Z_{\mathrm{s*}}-d} & L=0 \end{cases} \tag{2.27}$$

$$\Psi_{m*}(z,L) = \begin{cases} \ln(z-d) + \dfrac{4L\,\delta(z_l)}{3(Z_{m*}-d)\gamma_{m,u}}\left(1-\gamma_{m,u}\dfrac{z-d}{L}\right)^{0.75} & L<0 \\ \left(\dfrac{z-d}{Z_{m*}-d}\right)^{\eta}\dfrac{1}{\eta+1}\left((d-z)\dfrac{\gamma_{m,s}}{L}-1-1/\eta\right)+\ln(z-d) & L>0 \\ -\ln\left(\dfrac{Z_{m*}-d}{z-d}\right)-\left(\left(\dfrac{Z_{m*}-d}{z-d}\right)^{-\eta}\right)/\eta & L=0 \end{cases} \tag{2.28}$$

$$\delta(z_l) = \frac{Z_{m*}-d}{(Z_{m*}-z_l)\eta}\left(1-\frac{(z_l-d)^{\eta}}{(Z_{m*}-d)^{\eta}}\right)$$

In the case of momentum transfer under unstable conditions ($L < 0$), no explicit solution can be found to Eq. (2.26) as already stated by CELLIER & BRUNET (1992). The given equation (2.28, $L < 0$) represents the special solution for $\eta = 1$ multiplied by an empirical correction function $\delta(z_l)$. This correction term was derived under conditions of neutral stability with an identity relation between an approximate and an exact formulation of the wind speed gradient.

This was stated as:

$$\int_{z_l}^{Z_{m*}} \frac{\delta(z-d)}{Z_{m*}-d}/(z-d)\,dz = \int_{z_l}^{Z_{m*}}\left(\frac{z-d}{Z_{m*}-d}\right)^{\eta}/(z-d)\,dz \tag{2.29}$$

and solved for $\delta(z_l)$. The Ψ_{m*}- function is always calculated for two heights: the roughness layer height Z_{m*} and some lower height (z_l). This approximation works quite well, as shown in Fig. 2.7, where the approximate integral between two heights $\Psi_{m*}(Z_{m*}, L)$ - $\Psi_{m*}(z_l = h_c, L)$ is related to the exact integral (h_c =1, d = 0.75, η = 0.43). Even for large Z_{m*} the error does not exceeds 5%.

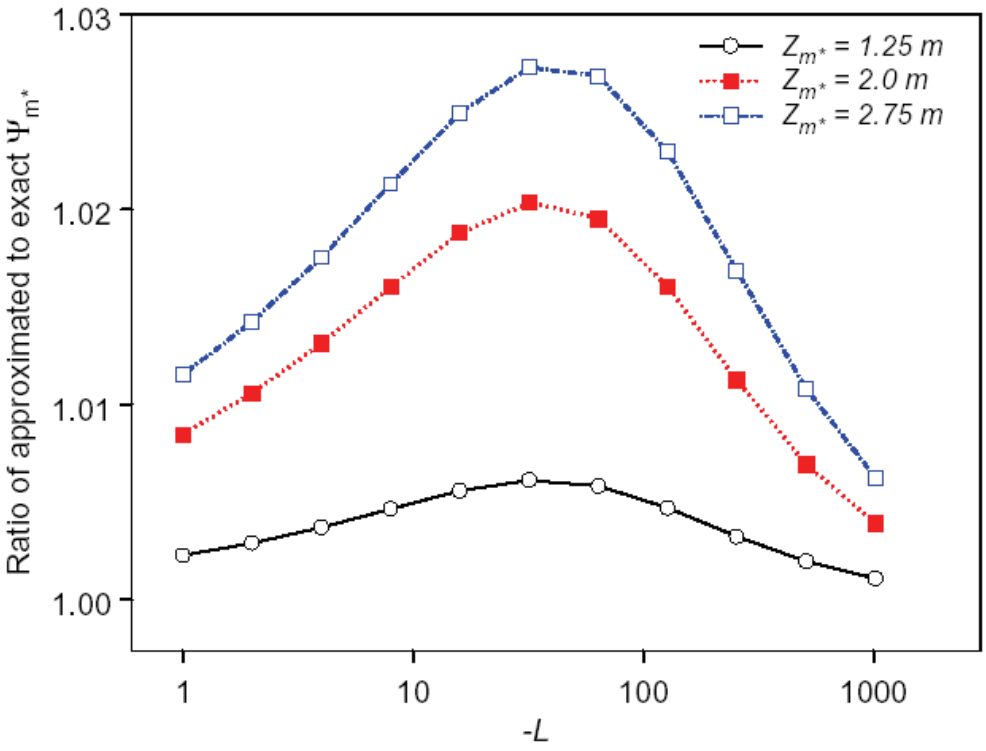

Fig. 2.7 Ratio between approximately and exactly integrated stability/roughness function for momentum under unstable atmospheric stratification for different height ranges (h_c, Z_{m*}) and stability classes as expressed with L (L - Obukhov length, h_c – canopy height assumed to be 1 m, Z_{m*} - roughness layer height).

2.4 Application in SVAT models

Using meteorological inputs at a reference height (z_r) above the canopy, the energy balance of the canopy - soil system is solved using different approaches. Common to all SVAT models is the calculation of friction velocity u_* and aerodynamic resistance to transfer of scalars r_a (heat, water vapour, CO_2). Calculations of wind speed at canopy top u_h and its gradient are used for computations of boundary layer resistance of leaves in multi-layer representations of the canopy - soil system or similarly the so-called excess resistance r_b (MONTEITH & UNSWORTH, 1990) known in one layer representations as the Penman - Monteith equation.

In the following it is assumed that the Obukhov length scale L is given, although it is usually estimated via an iteration procedure using relations for u_*, L, and the sensible

heat flux H, which depend on each other. Calculation of the friction velocity u_* requires the treatment of two cases:

$$u_* = \begin{cases} \dfrac{ku(z_\mathrm{r})}{\ln\left(\frac{z_\mathrm{r}-d}{z_{0,\mathrm{m}}}\right) - \Psi_\mathrm{m}(z_\mathrm{r},L) + \Psi_\mathrm{m}(z_{0,\mathrm{m}},L)} & z_\mathrm{r} \geq Z_{\mathrm{m}*} \\ \dfrac{ku(z_r)}{\ln\left(\frac{z_\mathrm{r}-d}{z_{0,\mathrm{m}}}\right) - \Psi_\mathrm{m}(Z_{\mathrm{m}*},L) + \Psi_\mathrm{m}(z_{0,\mathrm{m}},L) + \Psi_{\mathrm{m}*}(Z_{\mathrm{m}*},L) - \Psi_{\mathrm{m}*}(z_\mathrm{r},L)} & z_\mathrm{r} < Z_{\mathrm{m}*} \end{cases} \quad (2.30)$$

where this solution is derived from the definition of wind speed gradient in the inertial and roughness layer.

$$\frac{du}{dz} = \begin{cases} \dfrac{u_*\varphi_\mathrm{m}(z,L)}{k(z-d)} & \text{is integrated from } d+z_{0,\mathrm{m}} \text{ to the larger of } z_\mathrm{r} \text{ and } Z_{\mathrm{m}*} \\ \dfrac{u_*\varphi_\mathrm{m}(z,L)}{k(z-d)\,\varepsilon_\mathrm{m}(z)} & \text{is integrated from } Z_{\mathrm{m}*} \text{ to the smaller of } z_\mathrm{r} \text{ and } Z_{\mathrm{m}*} \end{cases} \quad (2.31)$$

with $u(d+z_{0,\mathrm{m}}) = 0$

with given details on integration limits and lower boundary condition. From Eq. (2.31) wind speed at canopy height is given as follows:

$$u(h_\mathrm{c}) = u(z_\mathrm{r}) - \frac{u_*}{k}\left[\ln\left(\frac{z_\mathrm{r}-d}{h_\mathrm{c}-d}\right) - x\right]$$

$$x = \begin{cases} \Psi_\mathrm{m}(z_\mathrm{r},L) - \Psi_\mathrm{m}(Z_{\mathrm{m}*},L) + \Psi_{\mathrm{m}*}(Z_{\mathrm{m}*},L) - \Psi_{\mathrm{m}*}(h_\mathrm{c},L) & z_\mathrm{r} > Z_{\mathrm{m}*} \\ \Psi_{\mathrm{m}*}(z_\mathrm{r},L) - \Psi_{\mathrm{m}*}(h_\mathrm{c},L) & z_\mathrm{r} \leq Z_{\mathrm{m}*} \end{cases} \quad (2.32)$$

The aerodynamic resistance r_a for scalars is defined as:

$$r_a = \begin{cases} \int_{z_{so}}^{Z_{s*}} \frac{Pr\,\varphi_s(z,L)}{k(z-d)u_*\,\varepsilon_s(z)}dz + \int_{Z_{s*}}^{z_r} \frac{Pr\,\varphi_s(z,L)}{k(z-d)u_*}dz + r_b & z_r > Z_{s*} \\ \int_{z_{so}}^{z_r} \frac{Pr\,\varphi_s(z,L)}{k(z-d)u_*\,\varepsilon_s(z)}dz + r_b & z_r \le Z_{s*} \end{cases} \tag{2.33}$$

where integration is from a virtual height of sources for scalars (z_{so}) and Pr denotes the turbulent Prandtl number (Pr = 0.95, HÖGSTRÖM (1996)). Integration of Eq. (2.33) leads to:

$$r_a = \begin{cases} \frac{\ln\left(\frac{z_r-d}{z_{so}-d}\right) - \Psi_s(z_r,L) + \Psi_s(Z_{s*},L) - \Psi_{s*}(Z_{s*},L) + \Psi_{s*}(z_{so},L)}{ku_*\,P_r^{-1}} + r_b & z_r > Z_{s*} \\ \frac{\ln\left(\frac{z_r-d}{z_{so}-d}\right) - \Psi_{s*}(z_r,L) + \Psi_{s*}(z_{so},L)}{ku_*\,P_r^{-1}} + r_b & z_r \le Z_{s*} \end{cases} \tag{2.34}$$

The value of z_{so} is usually h_c (r_b is calculated explicitly), otherwise it will be set to d + $z_{0,s}$ ($z_{0,s}$ roughness height of scalars, r_b = 0). Multi-layer models are designed to describe r_b directly via an integration of scalar fluxes and calculations of boundary layer resistances and turbulent exchange between the different layers. For one layer models r_b is very difficult to predict, but a comprehensive multi-layer model based parameterisation of r_b has been proposed by MASSMAN (1999), which accounts also for cases of partial covered soil.

In multi-layer models the boundary layer resistance is calculated from the described wind speed profile in the canopy, which is well described by an exponential decrease with relative height (RAUPACH & THOM, 1980; RAUPACH *et al.*, 1991):

$$u(z) = u_h \exp\left(-\alpha\left(1-\frac{z}{h_c}\right)\right) \tag{2.35}$$

Matching wind speed gradient of roughness and canopy layer at $z = h_c$ gives

$$\alpha = \frac{u_* \varphi_m(h_c, L)}{k(h_c - d)\,\varepsilon_m(h_c)\,u_h} = \frac{h_c \varphi_m(h_c, L)}{L_s} \tag{2.36}$$

a simple relation for the extinction parameter α. Moreover, after realizing the failure of the classical K-theory approach for computing scalar profiles in plant canopies, more advanced theories, such as the Lagrangian transfer theory, have been developed and applied within multi layer SVAT models (RAUPACH, 1987; BALDOCCHI & HARLEY, 1995). The key parameters of this approach are the Lagrangian time scale T_L and the vertical wind speed variance σ_w^2. RAUPACH *et al.* (1996) related T_L and L_s by:

$$T_L \approx \frac{0.71 L_s}{\sigma_w} \tag{2.37}$$

so there is a link to a canopy structure dependent prediction of T_L through L_s.

2.5 Discussion

2.5.1 Prediction of L_s/h_c

Here, an initial attempt is made to predict the length scale L_s/h_c from basic canopy properties. Thus, some additional comparisons are warranted to verify the proposed relation (Eq. (2.11)). The adaptation of L_s/h_c required for canopies with high relative spacing may be due to the advection of larger eddies from surrounding bare soil patches, which implies higher momentum transport efficiency, lower wind speed gradients and subsequently a higher L_s/h_c.

The relation of L_s to the extinction parameter α of the exponential wind speed profile broadens the empirical basis for comparison using Eq. (2.36). For instance, RAUPACH & THOM (1981) state that α has a typical range between 2 and 3 for most plant canopies, which is in good accordance with a stated typical value of $(L_s/h_c)^{-1}$ of about 2 by RAUPACH *et al.* (1996) where the mean calculated value of measured $(L_s/h_c)^{-1}$ is here 2.44 (excluding wind tunnel studies).

Whereas the predictions for L_s/h_c were made for ideal horizontally homogeneous canopies (in terms of h_c and *PAI*) there is some indication that it can also be related to local canopy structure. KATUL *et al.* (1999) showed that change of Eulerian length scale L_w depends on local PAI in a pine forest. RAUPACH *et al.* (1996) stated that L_w and L_s are linearly related. Therefore, it is argued that the estimated fraction $(L_w(L_{t,max})-L_w(L_{t,min}))/L_w(L_{t,max})$ from KATUL *et al.* (1999) should be similar as the analogue quantity derived from L_s computed with Eq. (2.11). Calculations with given inputs from KATUL *et al.* (1999) show indeed that these fractions compare well with measured 0.28 and predicted fraction 0.19 (Eq. (2.11) with $h_c = 14$, $d = 0.65h_c$, $f_{cr} \sim 0.8$, $\gamma \sim 3.3$, $L_{t,max} = 4.56$, $L_{t,min} = 2.65$).

The local dependence of L_s/h_c on *PAI* might be partly predictable, but conclusions for rather non-local aerodynamic quantities as $z_{0,m}$ are not possible within the here adopted one-dimensional framework.

2.5.2 Proposed relations for Z_{m*} and Z_{s*}

It is remarkable that the recorded values for Z_{m*} over corn (CELLIER & BRUNET, 1992), forests (MÖLDER *et al.*, 1999; BALDOCCHI & MEYERS, 1988), and savannah sites (GARRATT, 1980; FAZU & SCHWERDTFEGER, 1989) are well represented by Eq. (2.12) (see Fig. 2.5). Particularly in early studies on sparse canopies, Z_{m*} has been related to D.

The functional form of Z_{m*} for short canopies is just a guess ($h_c < 1.7$ m). Compared with the tall canopy term, the canopy height was omitted and L_s had to be upper-bounded to match observations appropriately. Regarding the limited experimental data and the fact that all estimates of Z_{m*} of short canopies are from wind tunnel studies, these choices are not well founded yet. However, this parameterisation is consistent with the finding over dense field crops (*e.g.* wheat) that estimates of friction velocity from wind profile measurements down to the canopy top compare well with estimates from direct eddy covariance measurements (DENMEAD, 1976; KOITZSCH *et al.*, 1988).

Even less is known about the behaviour of the roughness layer height for scalars Z_{s*}, which was observed to be equal to or greater than Z_{m*}. Here, only one expression is

used (Eq. (2.12)), because in contrast to momentum transfer it was found for short dense crops (cereals) that sensible heat fluxes are underestimated when using temperature profiles down to canopy top (DENMEAD, 1976; KOITZSCH *et al.,* 1988), which indicates a significant roughness layer effect on heat transfer or analogue: $Z_{s*} >> h_c$. For instance KOITZSCH *et al.* (1988) had to assume a mean ratio of K_s/K_m of ~ 2.1 for a wheat canopy to match sensible heat flux estimates from aerodynamic (profile based at heights 10, 20, 40, 80, 160 cm over h_c) with eddy covariance data. With an assumed $PAI = 6$ and their given mean $h_c = 0.88$ m (years 1982/83) the model presented here predicts a mean ratio $K_s/K_m = 1.72$ ($d/h_c = 0.82$. $Z_{m*}/h_c = 1.01$. $Z_{s*}/h_c = 1.91$). Thus, a reinterpretation would be that about 3 - 4 out of 5 heights were probably within the roughness layer for heat and have therefore confounded the estimates of sensible and latent heat flux through the presence of scalar diffusivity enhancement.

2.6 Conclusions

Several new predictive relations for parameters of momentum and scalar transfer in and above plant canopies are suggested. Based on retrieved records from the literature that cover a broad range of canopy structures, empirical models were proposed for the zero plane displacement d, the canopy length scale L_s, and the height of the roughness layer for momentum exchange Z_{m*} from basic canopy properties h_c, PAI, D, and f_{cr} .

The model of d is well justified, whereas the models for L_s and Z_{m*} are less certain because of the limited number of experimental records. Both the definition of a critical height h_{ci} as well as the parameterisation of Z_{m*} for short canopies with $h_c < h_{ci}$ need more independent justification. Nonetheless, there is an improved prediction of observed roughness lengths compared with a previous simpler roughness layer description (Raupach, 1992), which is a good indication on the overall parameterisation, as roughness lengths are rather insensitive to roughness layer details. The proposed equations represent therefore some progress compared with a neglected roughness layer or to an assumption of a constant effect.

From comparisons of predicted and observed roughness length $z_{0,m}$ it was concluded that

use of the profile function proposed by Cellier and Brunet (1992) is more appropriate even for canopies with high relative spacing D/h_c where the functional form of Garratt (1980) originated.

Assuming no interaction between buoyancy and roughness effects, the integrated stability/roughness layer functions are derived, and an approximate integration of the momentum function at unstable atmospheric conditions is proposed. Closed form analytical expressions are given for the friction velocity (u_*), the wind speed profile ($u(z)$) and the aerodynamic resistance (r_a) which account for both stability and roughness layer effects.

3 Simulation of soil heating in ridges partly covered with plastic-mulch - Energy balance model

List of Symbols and Abbreviations

c	fraction of sky covered with cloud (0..1)	
C_{air}	specific heat capacity of air	J mol^{-1} K^{-1}
C_s	volumetric heat capacity of soil	J m^{-3} K^{-1}
C_w	volumetric heat capacity of water	J m^{-3} K^{-1}
d	zero plane displacement	m
d_{gap}	thickness of the air layer between soil and plastic mulch	m
d_m	plastic thickness	µm
$d_{w,max}$	maximum effective thickness of liquid water film on plastic	µm
$d_{w,l}$	water film thickness at the lower plastic side	µm
$d_{w,u}$	water film thickness at the upper plastic side	µm
E	evaporation flux density	mol m^{-2} s^{-1}
e_a	water vapour pressure of air at reference height	mol m^{-3}
e_{ce}	water vapour pressure of air at common exchange height	mol m^{-3}
$e^*(T)$	saturation vapour pressure of water at temperature T	mol m^{-3}
F_b	geometry factor for direct (beam) radiation (0..1)	
F_d	sky view factor (01)	
$f_{d,ci}$	circumsolar part of diffuse solar radiation	
f_{drip}	fraction of dripping water on tilted surfaces if water capacity is exceeded, fraction (1- f_{drip}) slips down	
f_{wet}	wet area fraction of plastic surface	
F_s	soil view factor (0..1)	

g	gravitational constant	m s^{-2}
G	soil heat flux	W m^{-2}
h	water potential of soil	hPa
H	sensible heat flux	W m^{-2}
h_{eq}	parameter of the relative humidity function of upper soil layer	
k	von Kármán constant (0.4)	
$k(h)$	soil hydraulic conductivity function with water potential	cm d^{-1}
k_{mi}	mean thermal conductivity of minerals excluding quartz	W m^{-1} K^{-1}
k_o	thermal conductivity of organic matter	W m^{-1} K^{-1}
k_q	thermal conductivity of quartz	W m^{-1} K^{-1}
k_s	soil thermal conductivity	W m^{-1} K^{-1}
k_{sl}	effective thermal conductivity of solids	W m^{-1} K^{-1}
L	Obukhov length scale	m
M_w	molar mass of water	g mol^{-1}
n_{im}	imaginary part of refraction index	
n_r	real part of refraction index	
P	precipitation rate	cm d^{-1}
Pr	turbulent Prandtl number	
r_{a1}	turbulent transfer resistance between common exchange and reference height	s m^{-1}
r_{a2}	turbulent transfer resistance between surface and common exchange height	s m^{-1}
R_b	direct solar radiation including circumsolar diffuse radiation received by a horizontal plane	W m^{-2}
$r_{b,h}$	boundary layer resistance for forced and free convection of heat	s m^{-1}

$r_{b,v}$	boundary layer resistance for forced and free convection of water vapour	s m^{-1}
$r_{c,h}$	contact resistance to sensible heat transfer between soil and plastic	s m^{-1}
$r_{c,v}$	contact resistance to latent heat transfer between soil and plastic	s m^{-1}
R_d	diffuse solar radiation received by a horizontal plane	W m^{-2}
R_e	residual radiation exchange	W m^{-2}
r_h	resistance to heat transfer between surface and common exchange height	s m^{-1}
$r_{h,r}$	combined heat transfer and radiative resistance	s m^{-1}
$R_{L,e}$	emitted longwave radiation	W m^{-2}
R_n	net radiation	W m^{-2}
r_r	radiative resistance to long-wave radiation exchange	s m^{-1}
R_S	solar radiation received by a horizontal plane	W m^{-2}
$R_{S,g}$	mean short-wave radiation leaving ground surface	W m^{-2}
r_v	resistance to water vapour transfer between surface and common exchange height	s m^{-1}
rh_s	effective relative air humidity of the uppermost soil layer	
RMSE	root mean square error	
s_h	shadow indicator flag for surface point (0 or 1)	
T_a	reference height air temperature	K
T_{ce}	common exchange height air temperature	K
T_m	plastic mulch temperature	K
T_s	soil surface temperature	K
t_S	atmospheric transmission to solar radiation	
u	mean horizontal wind speed	m s^{-1}

u_*	friction velocity	m s^{-1}
u_a	horizontal wind speed at reference height	m s^{-1}
u_{so}	horizontal wind speed at source height	m s^{-1}
w	horizontal width of a surface patch represented by node i	m
W_{ba}	running nodal water balance	mm
w_e	condensation flux exeeding plastic mulch water capacity	µm d^{-1}
X_{hu}	soil humus content	g g^{-1}
X_{sand}	soil sand content	g g^{-1}
X_{silt}	soil silt content	g g^{-1}
y	psychrometric constant	mol m^{-3} K^{-1}
z	vertical coordinate	m
z_0	roughness length	m
z_{ce}	common exchange height	m
z_r	reference height, measurement height for u_a, T_a and e_a	m
z_{so}	effective height of sources or sinks (*e.g.* for sensible heat flux)	m
α	absorptivity	
α_b	sun (sky point) azimuth	rad
α_s	azimuth of surface normal	rad
β	sun elevation angle	rad
δ	incidence angle, angle between surface normal and light ray	rad
Δ	slope of the saturated vapour pressure temperature function	mol m^{-3} K^{-1}
Δ_t	time step	d
ε	emissivity	

γ_1	horizon obstruction angle at the opposing ridge	rad
γ_2	horizon obstruction angle by the nearest visible ridge	rad
θ	volumetric water content of soil	$m^3\ m^{-3}$
θ_{fk}	field capacity of soil	$m^3\ m^{-3}$
θ_{dry}	air dry water content of soil	$m^3\ m^{-3}$
κ	thermal diffusivity of air	$m^2\ s^{-1}$
λ	wave length of radiation	µm
λ_w	latent heat of vaporisation of liquid water	$J\ mol^{-1}$
μ	surface slope	rad
ρ	reflectivity	
ρ_{air}	air density	$mol\ m^{-3}$
σ	Stefan Boltzmann constant	$W\ m^{-2}\ K^{-4}$
τ	transmissivity	
Ψ_{mo}	integrated universal stability function for momentum	
Ψ_{sc}	integrated universal stability function for scalars	

3.1 Introduction

Soil ridges are sometimes used for agricultural production. In addition to ridging, parts of the soil surface may be covered with plastic mulches. Their application helps to achieve higher or sometimes lower soil temperatures compared to uncovered ridges and thereby to control the onset and dynamic of crop growth. For example, white asparagus spear production is commonly managed with ridges partially covered with plastic mulch.

Previous theoretical work has been done on the description of two dimensional heat and water transfer of uncovered soil ridges (MAHRER, 1982; MAHRER & AVISSAR, 1985; NOVAK, 1993) and on one-dimensional soil columns covered with plastic mulch (CHUNG & HORTON, 1987; DE LUCA & RUOCCO, 2000; HAM & KLUITENBERG, 1994; MAHRER *et al.,* 1984, MATTHIAS & PERALTA HERNANDEZ, 1998; SUI *et al.,* 1992; WU *et al*., 1996). Both types of models are amenable to improvements which will increase their accuracy. Additionally, neither model has yet been extended to enable a study of the heat and water transfer of soil ridges partly covered with plastic mulch.

One important process at the atmospheric boundary is the exchange of short- and long-wave radiation. To date, the approaches used to model the absorption of short- and long-wave radiation along ridge surfaces do not consider all factors required to produce the most accurate predictions for radiation absorption and hence energy balance. Therefore, these models can be improved by incorporating (1) a separate treatment of the absorption of direct and diffuse radiation including the addition of the circumsolar part of diffuse radiation to the direct part, (2) the modified interception of diffuse radiation and long-wave radiation depending on the surface location, and (3) the treatment of directional responses of short- and long-wave reflectivity and transmissivity of dry and wetted plastic mulches.

MAHRER (1982) accounted for a modified long-wave radiation interception of surface points depending on the ridge elevation angles; however, the effect of slope or non-uniform sky radiance distribution was not taken into account. Occasionally, global

radiation was separated into direct and diffuse fractions (MAHRER, 1982; SHARRATT *et al.*, 1992), but the reduced interception of diffuse radiation caused by the limited view of the sky dome and the effect of slope was not considered.

Here, an energy balance model for a two-dimensional ridge surface partly covered by a plastic mulch is presented. To avoid repeating work, a well-tested soil model (2DSOIL, TIMLIN *et al.*, 1996) which can be interfaced with a detailed description of aboveground energy balances was used to simulate the soil heat and water transfer.

3.2 Description of the energy balance model

3.2.1 Definition of the system

A horizontal extended field of parallel and infinitely long soil ridges is considered, where the ridge shape is assumed to vary only in the direction perpendicular to the ridges. The ridges may be partly covered with a plastic mulch. The ridge shape could be given as a continuous or piecewise linear function of the horizontal width ($y(x)$). Using this function and the ridge direction, several geometric surface properties can be deduced at a specific surface location: the slope μ, the aspect α_s [*i.e.* the azimuth of the surface normal at point (x_i, y_i) from the north] and the angles of perpendicular obstructed horizons (γ_1, γ_2, see Fig. 3.1).

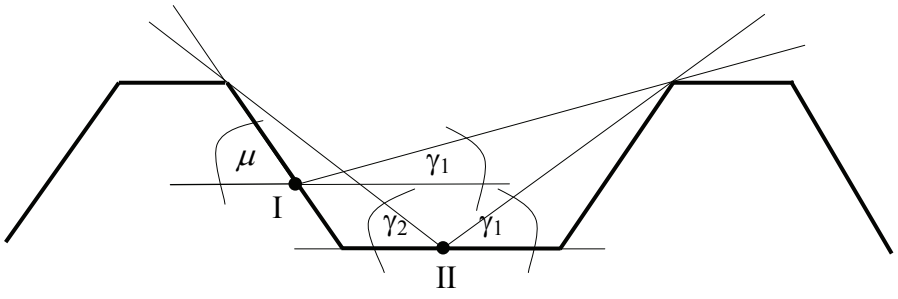

Fig. 3.1 A transect through a ridge configuration with two indicated locations (I, II) characterised by slope μ and perpendicular horizon obstruction angles γ_1 and γ_2. Note that at location I: $\mu = \gamma_2$ and at location II: $\mu = 0$.

Single surface patches which are represented by nodes exchange energy between the

soil and the overlying free air stream via short- and long-wave radiation fluxes as well as sensible and latent heat fluxes. Latent heat exchange of covered surface nodes is confined to the air layer between the soil and the plastic mulch as plastics are largely non-permeable to water vapour (PIERGIOVANNI *et al.,* 1995; QIRK & ALSAMARRAIE, 1999).

The applied resistive network for the sensible heat flux is illustrated in Fig. 3.2. All nodes exchange heat in parallel with a virtual common exchange height (z_{ce}), which is below the usual reference height (z_r = 2 m) of air temperature.

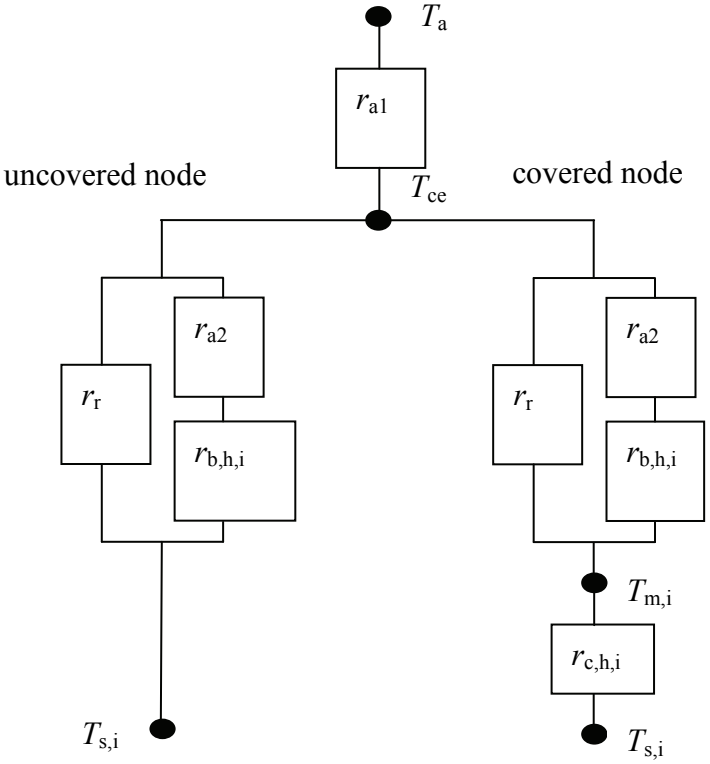

Fig. 3.2 Assumed resistive network of sensible heat fluxes from uncovered nodes on the left and covered surface nodes on the right. r_{a1}: turbulent transfer resistance between reference height and common exchange height; r_{a2}: turbulent transfer resistance between common exchange height and effective height of sources; $r_{b,h,i}$: node-specific boundary layer resistance; r_r: radiative resistance; $r_{c,h,i}$: heat contact resistance at node i; T_a, T_{ce}: air temperatures at reference and common exchange height, respectively; $T_{m,i}$, $T_{s,i}$: temperatures of plastic mulch and soil surface, respectively

This common exchange height was introduced to mimic interactions between potential

hot and cool surface nodes and to supply an appropriate free stream temperature for free convection calculations. Uncovered and covered nodes exchange heat very similarly. However, for covered nodes, an additional contact resistance ($r_{c,h}$), which describes the effect of the very thin air layer between the plastic mulch and the soil on heat exchange (HAM & KLUITENBERG, 1994), is required. The radiative resistance (r_r), which acts in parallel both to the boundary layer resistance for heat ($r_{b,h}$) and the lower turbulent resistance (r_{a2}), was included to express net radiation in terms of the air temperature at common exchange height (isothermal net radiation concept, MONTEITH & UNSWORTH, 1990).

Similarly, the same resistance network applies for latent heat fluxes of nodes with the corresponding boundary layer resistance for water vapour ($r_{b,v}$), contact resistance to water vapour exchange ($r_{c,v}$) and an omitted radiative resistance.

3.2.2 Specification of resistances

The turbulent resistances (r_{a1}, r_{a2}) have been defined from the semi-logarithmic wind speed law with stability correction terms (Ψ_{sc}, Ψ_{mo}) as provided in HÖGSTRÖM (1996).

$$
\begin{aligned}
r_{a1} &= \frac{\ln\left(\frac{z_r - d}{z_{ce} - d}\right) - \Psi_{sc}(z_r, L) + \Psi_{sc}(z_{ce}, L)}{k u_* Pr^{-1}} \\
r_{a2} &= \frac{\ln\left(\frac{z_{ce} - d}{z_{so} - d}\right) - \Psi_{sc}(z_{ce}, L) + \Psi_{sc}(z_{so}, L)}{k u_* Pr^{-1}} \\
\text{with} \quad u_* &= \frac{k u_a}{\ln\left(\frac{z_r - d}{z_{0,m}}\right) - \Psi_{mo}(z_r, L) + \Psi_{mo}(z_0 + d, L)}
\end{aligned}
\tag{3.1}
$$

where the reference height of wind and temperature measurement is z_r, the assumed height of sources is z_{so}, the friction velocity is u_*, Obukhov length scale is L, wind speed at reference height is u_a, the turbulent Prandtl number is Pr, zero plane displacement is d and roughness length is z_0.

The boundary layer resistance for heat has been calculated by a relation adapted from KUSTAS and NORMAN (1999) which accounts for both forced and free convection.

$$r_{\mathrm{b,h,i}} = (0.018u_{\mathrm{s}} + 0.0025fc_{\mathrm{i}})^{-1}$$
$$fc_{\mathrm{i}} = \begin{cases} max(T_{\mathrm{s,i}} - T_{\mathrm{ce}}, 0)^{\frac{1}{3}} & \mu = 0 \\ |T_{\mathrm{s,i}} - T_{\mathrm{ce}}|^{\frac{1}{3}} & \mu > 0 \end{cases} \qquad (3.2)$$

where u_{s} is the calculated horizontal wind speed close to the soil surface, $T_{\mathrm{s,i}}$ is the temperature of the node i which represents either the surface soil temperature for uncovered nodes or the mulch temperature for covered nodes. T_{ce} is the calculated air temperature at common exchange height. The typical range for the coefficient to u_{s} is 0.012…0.024 (KUSTAS & NORMAN, 1999) and was set to 0.018 to obtain similar responses as from the parameterisation of $r_{\mathrm{b,h}}$ given by MCINNES *et al*. (1994). In contrast to horizontal surfaces, the modification factor for free convection (fc_{i}) also applies to tilted surface patches ($\mu > 0$) which are cooler than the surrounding air temperature as an airflow is initiated down the slope (INCROPERA & DEWIT, 2002).

The wind speed close to the soil surface was derived from the friction velocity term (Eq. (3.1))

$$u_{\mathrm{s}} = u_* / k \left(\ln\left(\frac{z_{\mathrm{so}} - d}{z_0} \right) - \Psi_{\mathrm{mo}}(z_{\mathrm{so}}, L) + \Psi_{\mathrm{mo}}(z_0 + d, L) \right) \qquad (3.3)$$

MCINNES *et al.* (1994) found that the boundary layer resistance varies by about ± 10% depending on the vertical position of surface nodes with the lowest resistance at the ridge top and the highest near the furrow. Introducing this dependence as a linear interpolation between top and furrow states and a serial combination of r_{b} and r_{a2} gives resistances for heat and water vapour, respectively

$$r_{\mathrm{h,i}} = r_{\mathrm{a2}} + f_{\mathrm{z,i}} r_{\mathrm{b,h,i}}, \quad r_{\mathrm{v,i}} = r_{\mathrm{a2}} + 0.93 f_{\mathrm{z,i}} r_{\mathrm{b,h,i}} \qquad \text{with} \quad f_{\mathrm{z,i}} = 1 / \left(0.9 + 0.2 \frac{z_{\mathrm{i}} - z_{\mathrm{min}}}{z_{\mathrm{max}} - z_{\mathrm{min}}} \right) \qquad (3.4)$$

where z_i, z_{min} and z_{max} denote the z-coordinate of the node and the maximum and minimum of z values over all surface nodes, *i.e.* the heights of the peak and the furrow, respectively. Furthermore, a parallel combined boundary and radiative resistance (r_r) is calculated.

$$r_{h,r,i} = \left(\frac{1}{r_{h,i}} + \frac{1}{r_r} \right)^{-1} \quad \text{with } r_r = \frac{\rho_{air} C_{air}}{4 n_{sides} \sigma \varepsilon_i T_{ce}^{\ 3}} \tag{3.5}$$

where air density is ρ_{air}, specific heat of air is C_{air}, Stefan-Boltzmann constant is σ, surface emissivity is ε_i and the number of emitting surfaces n_{sides} (n_{sides} = 1 and 2 for uncovered and covered nodes, respectively).

The contact resistance between the soil and the lower side of the plastic can be approximated with the theory of horizontal or inclined rectangular cavities (INCROPERA & DEWITT, 2002). However, calculations with reasonable thicknesses of that air layer (1 to 6 mm) revealed that the critical Rayleigh number (Ra = 1708) will be rarely exceeded. Thus, the prevailing mode of mass and heat transfer will be via conduction through a resting air layer. The contact resistances for heat and water vapour transfer are therefore given as:

$$r_{c,h,i} = (d_{gap} - d_{w,l,i}) / \kappa_i, \; r_{c,v,i} = 0.93 r_{c,h,i} \tag{3.6}$$

with mean air layer and lower plastic side liquid water thickness represented by d_{gap} and $d_{w,l,i}$, respectively, and air thermal diffusivity by κ_i which was parameterised as function of temperature from data provided in MONTEITH and UNSWORTH (1990).

3.2.3 Absorption of short-wave radiation

The incident global radiation (R_S) is separated into diffuse (R_d) and direct (R_b) components. The interception of diffuse radiation is altered by obstructed horizons and the inclination of the surface. Several models are available that describe the diffuse part (f_d) of global radiation as a function of atmospheric transmittance (t_S) and solar

elevation (β, see Fig. 3.3). Here, the parameterisation of SKARTVEIT *et al.* (1998) is used. Furthermore, the anisotropy of diffuse sky radiation, which is caused by the circumsolar region of the sky, was considered. This fraction was approximated by HAY (1979) using $f_{d,ci} = (1 - f_d)t_S$. Taking the aforementioned factors into account, the effective direct and diffuse components of solar radiation incident on a horizontal plane can be calculated as:

$$\begin{aligned} R_d &= f_d R_S (1 - f_{d,ci}) \\ R_b &= R_S - R_d \end{aligned} \tag{3.7}$$

The absorbed solar radiation of an uncovered soil surface point ($R_{S,s,i}$) can be expressed as:

$$R_{S,s,i} = \alpha_{b,s,i} R_b F_{b,i} + \alpha_{d,s,i}(R_d F_{d,i} + R_{S,g} F_{s,i}) \text{ with } F_{b,i} = s_{h,i} \frac{\cos \delta_i}{\sin \beta} \text{ and } F_{s,i} = 1 - F_{d,i} \tag{3.8}$$

where the $\alpha_{b,s,i}(\delta)$ and $\alpha_{d,s,i}$ are the absorptivities of the direct and diffuse radiation components of the soil, respectively, δ is the incidence angle of the direct light beam, s_h denotes a shadow flag (which is zero if the point lies in a beam shadow, otherwise it is one), the view factors $F_{b,i}$, $F_{d,i}$ and $F_{s,i}$ account for the modified interception of direct, diffuse sky radiation and reflected radiation from the soil, respectively, and $R_{S,g}$ denotes a mean reflected radiation leaving the surrounding soil.

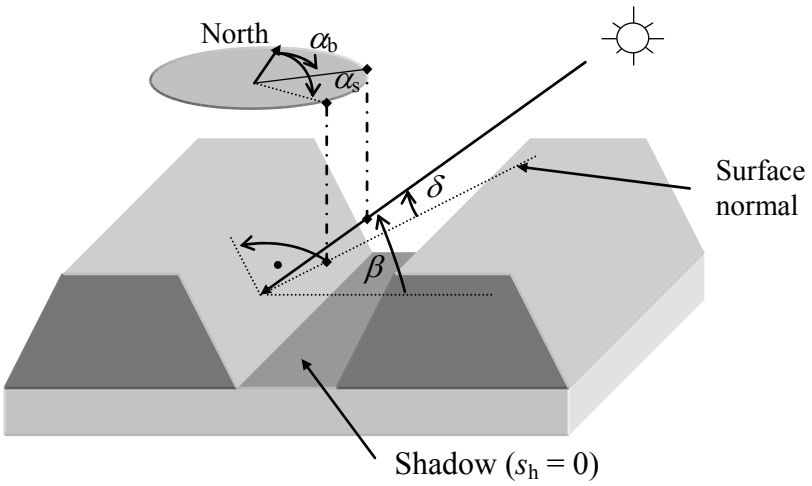

Fig. 3.3 Geometry of incident direct radiation on a ridge system; α_b sun azimuth; α_s surface normal azimuth; β sun elevation angle; δ radiation incidence angle; s_h shadow index.

The positive cosine of the incidence angle is given by:

$$\cos\delta_i = \max(\sin\beta\cos\mu_i + \cos\beta\sin\mu_i\cos\Delta_{\alpha,i}, 0) \tag{3.9}$$

where $\Delta_{\alpha,i}$ is the difference between the sun azimuth (α_b) and surface point normal azimuth (α_s, see Fig. 3.3). The albedo of an air dry soil was estimated from a relation given by BAUMER (1990)

$$\rho_{s,dry} = \min[0.6\exp(-40X_{hu}), 0.3] \tag{3.10}$$

with humus content of the top soil layer represented by X_{hu} and an added upper constraint being 0.3. Using a relation from ÅNGSTRÖM (1925), the corresponding wet soil albedo was derived from:

$$\rho_{s,wet} = \rho_{s,dry} / \left(n_r^2(1-\rho_{s,dry}) + \rho_{s,dry}\right) \tag{3.11}$$

where n_r is the real refraction index of water in the short-wave range (n_r = 1.325). As according to IDSO *et al.* (1975) and VAN BAVEL and HILLEL (1976), a linear interpolation between dry and wet soil albedo with actual volumetric soil water content θ_i was applied.

$$\rho_{s,i} = \rho_{s,dry} + (\rho_{s,dry} - \rho_{s,wet})\frac{\min(\theta_i, \theta_{fk}) - \theta_{dry}}{\theta_{fk} - \theta_{dry}} \tag{3.12}$$

where θ_{fk} and θ_{dry} are the field capacity and the air dry water content of the upper soil layer. Soil reflectivity tends to increase at high incidence angles, and this dependence was described using a relationship given by DICKINSON *et al.* (1986) in cases where the incidence angle increased above 60°:

$$\rho_{s,i}' = \begin{cases} 0.4(1-\rho_{s,i})\left(\dfrac{1.5}{1+4\sin(0.5\pi-\delta_i)}-0.5\right) & \delta_i \geq 60° \\ \rho_{s,i} & \delta_i < 60° \end{cases} \tag{3.13}$$

The corresponding absorptivities (Eq. (3.8)) were then simply given by:

$$\alpha_{d,s,i}=1-\rho_{s,i} \quad , \alpha_{b,s,i}=1-\rho_{s,i}' \tag{3.14}$$

The equation for the sky view factor $F_{d,i}$ was derived from an integral expression describing the sum of light originating from all uniform radiating sky points which contribute to the radiation interception of a surface location i with slope μ_i and perpendicular horizon obstructions $\gamma_{1,i}$ and $\gamma_{2,i}$. where the integration over the azimuth α begins at the ridge long axis.

$$F_{d,i}=\frac{1}{\pi}\int_0^{2\pi}\int_{\beta_{0,i}}^{\frac{\pi}{2}} \cos\beta\cos\delta_i \, d\beta \, d\alpha, \quad \beta_{0,i}=\begin{cases} \text{atan}(-\tan\gamma_{2,i}\cos(\alpha-\pi/2)) & \pi<\alpha\leq 2\pi \\ \text{atan}(\tan\gamma_{1,i}\cos(\alpha-\pi/2)) & 0<\alpha\leq\pi \end{cases} \tag{3.15}$$

The lower limit of the integration $\beta_{0,i}$ describes the actual horizon obstruction as a function of sky point azimuth and the given horizon obstructions perpendicular to the ridge long axis. Integration of Eq. (3.15) yields:

$$F_{d,i}=\frac{\cos(\max(\gamma_{2,i}-\mu_i,0))+\cos(\gamma_{1,i}+\mu_i)}{2} \tag{3.16}$$

Even with the removal of the circumsolar part of diffuse radiation, there is likely to be some anisotropy of diffuse sky radiation remaining, and the obtained uniform sky solution (Eq. (3.16)) might be not appropriate. This uncertainty was assessed by a simulation study using the "all-weather sky" luminance model of PEREZ *et al.* (1993) and a modification of Eq. (3.15) to normalise fluxes according to an approach proposed by VARTIAINEN (2000).

$$F_{\mathrm{d,sim}} = \frac{\int_0^{2\pi}\int_{\beta_0}^{\frac{\pi}{2}} \cos\beta\cos\delta L_u(\beta,\alpha)\,d\beta\,d\alpha}{\int_0^{2\pi}\int_0^{\frac{\pi}{2}} \cos\beta\sin\beta\,L_u(\beta,\alpha)\,d\beta\,d\alpha} \tag{3.17}$$

where the cases $\gamma_{2,\mathrm{i}} > \mu$ were here omitted and $L_\mathrm{u}(\beta, \alpha_\mathrm{b})$ is the sky luminance function given by PEREZ *et al.* (1993). VARTIAINEN (2000) demonstrated the validity of this approach among many other slope irradiance modelling approaches where predictions of total slope irradiances using Eqs. (3.8) and (3.17) were compared to measurements. The required parameters of the used sky luminance function $L_\mathrm{u}(\beta, \alpha_\mathrm{b})$ were obtained from two inputs: the ratio (t_S) between actual and extraterrestrial solar radiation (*i.e.* atmospheric transmission) and the fraction of diffuse solar radiation on total radiation (f_d). Firstly, the diffuse fraction was derived from t_S and β using the model provided in SKARTVEIT *et al.* (1998). Secondly, the numerical integration of Eq. (3.17) was performed using a nine-point Gauss algorithm. Thirdly, a large data set of realisations (n = 21,500) was simulated by a full combination of possible surface point geometries and sky conditions. The corresponding variable ranges and steps are listed in Table 3.1 .

Table 3.1 Variables, their ranges and step sizes, which were fully combined during the simulation of the test data set.

Variable	Range	Step size	Remarks
β	5°...80°	15°	
t_S	0.1...$t_\mathrm{S,max}$	0.05	$t_\mathrm{S,max} = 0.83 - 0.56\exp(-0.06\beta)$, SKARTVEIT *et al.* (1998)
μ	10°...90°	10°	
γ_1	0°...60°	15°	
Δ_α	0°...180°	45°	Difference between sun azimuth and surface point normal azimuth

The generated data set includes the circumsolar fraction of diffuse radiation, so that the simulated view factors were fitted by:

$$\hat{F}_{\mathrm{d,sim}} = a_1(1 - f_{\mathrm{d,ci}})F_{\mathrm{d}} + f_{\mathrm{d,ci}}F_{\mathrm{b}} \tag{3.18}$$

A least-square fit (STATSOFT, INC., 2001 STATISTICA for Windows, version 6) yielded an estimated coefficient a_1 =1.001 and accounted for 88% of simulated diffuse radiation interception ($R^2 = 0.88$, $RMSE = 0.1$).

Calculated reductions of diffuse radiation interception are detailed in Fig. 3.4 for various geometries. It is apparent that there is a reduction of intercepted diffuse radiation with increasing slope and with larger horizon obstruction angles towards the opposing ridge (γ_1) and the local slope in cases when γ_2 exceeds μ.

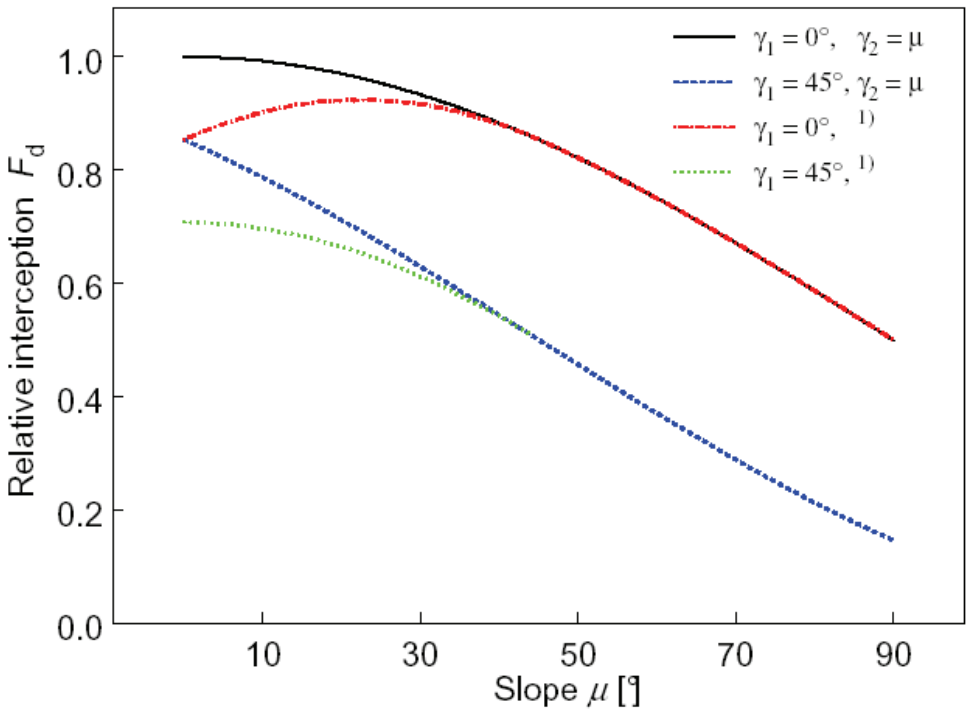

Fig. 3.4 Relative interception of short-wave diffuse sky radiation (F_d, Eq. (3.16)) of various surface geometries in terms of μ, γ_1 and γ_2 compared to a horizontal surface (γ_1, γ_2 horizon obstruction angles at a surface location with slope μ). 1) $\gamma_2 = \max(45°, \mu)$

3.2.4 Absorption of long-wave radiation

The interception of long-wave radiation bears a strong similarity to that of diffuse solar radiation, but has additional losses due to self emission. The long-wave radiation balance of an uncovered soil surface point *i* may be written as:

$$R_{\mathrm{L,s,i}} = \varepsilon_{\mathrm{s,i}} \left[R_{\mathrm{L,d}} F_{\mathrm{L,d,i}} + R_{\mathrm{L,g}} F_{\mathrm{s,i}} - \sigma T_{\mathrm{ce}}{}^{4} \right] \tag{3.19}$$

where $R_{\mathrm{L,d}}$ is the long-wave radiation originating from the sky and $R_{\mathrm{L,g}}$ is the mean long-wave radiation leaving the ground. The soil view factor is again given by $F_{\mathrm{s,i}} = 1 - F_{\mathrm{d,i}}$ because the reflected and emitted flux from the ground is assumed to be uniform. The uniformity assumption will be violated if there are strong surface temperature gradients between the furrow and the peak of the ridges; however, if this were to be the case, then it would be expected to have no large effects on nodal energy balance.

The emissivity of the soil surface was made dependent on actual volumetric water content of the node after VAN BAVEL and HILLEL (1976)

$$\varepsilon_{\mathrm{s,i}} = 0.9 + 0.18\theta_{\mathrm{i}} \tag{3.20}$$

There are various models that can predict the atmospheric long-wave radiation ($R_{\mathrm{L,d}}$) from air temperature, air vapour pressure and cloud fraction (BRUTSAERT, 1982; UNSWORTH & MONTEITH, 1975). However, only a few researchers have investigated the angular distribution of long-wave radiation from the sky, although UNSWORTH and MONTEITH (1975) presented an equation to calculate the intensity distribution:

$$I_{\mathrm{L}}(\beta) = ((1 - n_{\mathrm{p}} c)(a + b \ln(u_{\mathrm{w}} / \sin\beta)) + n_{\mathrm{p}} c) / \pi \tag{3.21}$$

where n_{p}, a and b are parameters, u_{w} is the atmospheric water depth at sky zenith (cm) and c is the cloud fraction. Similarly calculations as for the diffuse sky factor (Eq. (3.17)); replacing $L_{\mathrm{u}}(\beta, \alpha_{\mathrm{b}})$ with $I_{\mathrm{L}}(\beta)$) for a range of cloud fractions and ridge geometries revealed no large errors (~1%) when the long-wave sky factor was approximated with the diffuse sky factor:

$$F_{\mathrm{L,d,i}} \approx F_{\mathrm{d,i}} \tag{3.22}$$

Equation (3.21) and hence Eq. (3.22) are only valid for either clear or fully overcast sky conditions. Intermediate sky conditions have rather erratic distributions of long-wave radiation intensity (WEINLÄDER *et al.*, 2002) due to unpredictable cloud pattern.

3.2.5 Energy balance of uncovered nodes

For uncovered surface nodes the energy balance is given by:

$$R_{n,i} = H_i + G_i + \lambda_{\mathrm{w}} E_i \tag{3.23}$$

with sensible heat flux H_{i} , soil heat flux G_{i}, evaporation $\lambda_{\mathrm{w}}E_{\mathrm{i}}$ and isothermal net radiation $R_{\mathrm{n,i}}$. The sensible heat flux was calculated as:

$$H_{\mathrm{i}} = \rho_{\mathrm{air}} C_{\mathrm{air}} (T_{\mathrm{s,i}} - T_{\mathrm{ce}}) / r_{\mathrm{h,r,i}} \tag{3.24}$$

Using a semi-empirical derived relative humidity at the soil surface (rh_{s}), the latent heat flux is given as:

$$\lambda_{\mathrm{w}} E_{\mathrm{i}} = \frac{\rho_{\mathrm{air}} C_{\mathrm{air}} (rh_{\mathrm{s,i}} (e^*(T_{\mathrm{ce}}) + \Delta (T_{\mathrm{s,i}} - T_{\mathrm{ce}})) - e_{\mathrm{ce}})}{yr_{\mathrm{v,i}}} \tag{3.25}$$

where slope of the water vapour-temperature relation is Δ, psychometric constant is y, saturated and calculated vapour pressure at common exchange height are $e^*(T_{\mathrm{ce}})$ and e_{ce}, respectively, latent heat of vaporisation of water is λ_{w}. Combination of Eqs. (3.7), (3.24) and (3.9) allows the elimination of $T_{\mathrm{s,i}}$.

$$\lambda_{\mathrm{w}} E_i = \frac{\Delta rh_{\mathrm{s,i}} r_{\mathrm{h,r,i}} (R_{\mathrm{n,s,i}} - G_i) + \rho_{\mathrm{air}} C_{\mathrm{air}} (rh_{\mathrm{s,i}} e^*(T_{\mathrm{ce}}) - e_{\mathrm{ce}})}{\Delta rh_{\mathrm{s}} r_{\mathrm{h,r,i}} + yr_{\mathrm{v,i}}} \tag{3.26}$$

where the relative humidity at the soil surface is estimated using a node-based running water balance after SCHELDE *et al.* (1998).

$$rh_{s,i} = \exp\left(\frac{h_i M_w g 10^{-h_{eq} W_{ba,i}}}{R T_{s,i}}\right) \text{ with } W_{ba,i} = \min(\max(W_{ba,i}' - E_i' + P_i', -2), 1) \tag{3.27}$$

with molar mass of water M_w, gravitational constant g, soil water potential h_i, gas constant R, parameter h_{eq} and the running water balance term $W_{ba,i}$ [mm] of node i which is confined within the limits (-2; 1). E_i and P_i are the evaporation and precipitation rates per node and time step (in mm). The prime denotes the corresponding values from previous time step. Equation (3.27) may be viewed as a feed forward modelling device to account for reductions in soil evaporation due to subsequent drying. This would not be required if the spatial subdivision of the soil domain would be very small. Such a small size of surface elements would lead to a very large number of nodes and elements which results in a problem size that cannot be solved in a reasonable amount of time.

Net radiation is calculated as the sum of absorbed short-wave radiation ($R_{S,s,i}$) and long-wave radiation ($R_{L,s,i}$):

$$R_{n,s,i} = R_{S,s,i} + R_{L,s,i} \tag{3.28}$$

3.2.6 Energy balance of covered nodes

Following HAM and KLUITENBERG (1994), the energy balance has to be evaluated for both the soil and the plastic mulch and may be stated as:

$$\begin{aligned} R_{n,s,i} &= H_{sm,i} + G_i + \lambda_w E_{sm,i} + R_{e,s,i} \\ R_{n,m,i} &= -H_{sm,i} + H_{mb,i} - \lambda_w E_{sm,i} + \lambda_w E_{mb,i} + R_{e,m,i} \end{aligned} \tag{3.29}$$

with nodal net radiation fluxes of soil and plastic $R_{n,s,i}$, $R_{n,m,i}$ sensible and latent heat fluxes confined to the air layer between soil and plastic $H_{sm,i}$, $\lambda_w E_{sm,i}$ and between the outside of the plastic and the common exchange height $H_{mb,i}$, $\lambda_w E_{mb,i}$, and a residual term R_e which accounts for the internal long-wave radiation exchange between the lower plastic side and the soil surface.

The sensible heat fluxes are derived from:

$$H_{\mathrm{sm,i}} = \frac{\rho_{\mathrm{air}} C_{\mathrm{air}} (T_{\mathrm{s,i}} - T_{\mathrm{m,i}})}{r_{\mathrm{c,h,i}}},\ H_{\mathrm{mb,i}} = \frac{\rho_{\mathrm{air}} C_{\mathrm{air}} (T_{\mathrm{m,i}} - T_{\mathrm{ce}})}{r_{\mathrm{h,r,i}}} \tag{3.30}$$

The latent heat fluxes were derived from:

$$\begin{aligned} \lambda_{\mathrm{w}} E_{\mathrm{sm,i}} &= \frac{\rho_{\mathrm{air}} C_{\mathrm{air}} (e^*(T_{\mathrm{m}})(rh_{\mathrm{s,i}} - 1) + \Delta rh_{\mathrm{s,i}} (T_{\mathrm{s,i}} - T_{\mathrm{m,i}}))}{y(r_{\mathrm{c,v}} + r_{\mathrm{s,l}})} \\ \lambda_{\mathrm{w}} E_{\mathrm{mb,i}} &= \frac{\rho_{\mathrm{air}} C_{\mathrm{air}} (\Delta(T_{\mathrm{m,i}} - T_{\mathrm{ce}}) + e^*(T_{\mathrm{ce}}) - e_{\mathrm{ce}})}{y(r_{\mathrm{v,i}} + r_{\mathrm{s,u}})} \end{aligned} \tag{3.31}$$

where the latent heat exchange calculation between soil and mulch uses the saturated vapour pressure of the mulch ($e^*(T_{\mathrm{m}})$) from the previous time step. The surface resistance of the upper and lower side of the mulch $r_{\mathrm{s,u}}$, $r_{\mathrm{s,l}}$ where set depending on the state of the previous time step as according to:

$$r_{\mathrm{s,u}} = \begin{cases} 10000 & \text{otherwise} \\ 0 & d_{\mathrm{w,u,i}} \geq 5\mu m \end{cases} \quad r_{\mathrm{s,l}} = \begin{cases} 10000 & \text{otherwise} \\ 0 & d_{\mathrm{w,l,i}} \geq 5\mu m \ \text{ or } \ (e_{\mathrm{s,i}} - e_{\mathrm{m,i}})/e_{\mathrm{m,i}} > 0.1 \end{cases} \tag{3.32}$$

This overcomes the problem of estimation of water fluxes from dry plastics.

Another as yet unspecified energy balance term is the residual term (R_{e}) caused by long-wave radiation exchange of emitted radiation by the soil surface and the lower side of the plastic mulch. By deriving the emitted long-wave radiation fluxes beneath the plastic mulch, the downward ($R_{\mathrm{L}\downarrow}$) and upward ($R_{\mathrm{L}\uparrow}$) net fluxes can be obtained:

$$\begin{aligned} R_{\mathrm{L}\downarrow} &= e_{\mathrm{m}} \sigma T_{\mathrm{m}}{}^4 + \rho_{\mathrm{L}} R_{\mathrm{L}\uparrow} \\ R_{\mathrm{L}\uparrow} &= \varepsilon_{\mathrm{s}} \sigma T_{\mathrm{s}}^4 + (1 - \varepsilon_{\mathrm{s}}) R_{\mathrm{L}\downarrow} \end{aligned} \tag{3.33}$$

The amount of reabsorbed radiation is $\varepsilon_{\mathrm{m}} R_{\mathrm{L}\uparrow}$ for the plastic mulch and $\varepsilon_{\mathrm{s}} R_{\mathrm{L}\downarrow}$ for the soil. Substituting the solutions for downward and upward fluxes yields the following equations for the residual terms:

$$
\begin{aligned}
R_{\mathrm{e,s,i}} &= \frac{\varepsilon_{\mathrm{m,i}}^{2}\sigma T_{\mathrm{m}}{}^{4} + \rho_{\mathrm{L,i}}\varepsilon_{\mathrm{s,i}}e_{\mathrm{m,i}}\sigma T_{\mathrm{s,i}}{}^{4}}{1-\rho_{\mathrm{L,i}}(1-\varepsilon_{\mathrm{s,i}})}\varepsilon_{\mathrm{s,i}} \\
R_{\mathrm{e,m,i}} &= \frac{\varepsilon_{\mathrm{m,i}}(1-\varepsilon_{\mathrm{s,i}})\sigma T_{\mathrm{m,i}}{}^{4} + \varepsilon_{\mathrm{s,i}}\sigma T_{\mathrm{s,i}}{}^{4}}{1-\rho_{\mathrm{L,i}}(1-\varepsilon_{\mathrm{s,i}})}\varepsilon_{\mathrm{m,i}}
\end{aligned}
\tag{3.34}
$$

where $\rho_{\mathrm{L,i}}$, $\varepsilon_{\mathrm{m,i}}$ and $T_{\mathrm{m,i}}$ are the long-wave reflectivity, emissivity and temperature of plastic mulch, respectively. The net radiation for a covered soil surface was calculated as:

$$
\begin{aligned}
R_{\mathrm{n,s,i}} &= R_{\mathrm{S,s,i}} + R_{\mathrm{L,s,i}} \\
R_{\mathrm{S,s,i}} &= \alpha_{\mathrm{d,s,i}}(F_{\mathrm{d,i}}R_{\mathrm{d}} + F_{\mathrm{s,i}}R_{\mathrm{S,g}}) + \alpha_{\mathrm{d,s,i}}F_{\mathrm{b,i}}R_{\mathrm{b}} \\
R_{\mathrm{L,s,i}} &= \alpha_{\mathrm{L,s,i}}(F_{\mathrm{d,i}}R_{\mathrm{L,d}} + F_{\mathrm{s,i}}R_{\mathrm{L,g}}) - \varepsilon_{\mathrm{s,i}}\sigma T_{\mathrm{ce}}{}^{4}
\end{aligned}
\tag{3.35}
$$

with long-wave absorptivity of the covered soil $\alpha_{\mathrm{L,s,i}}$. After passage of the direct radiation flux through the plastic, it was assumed to be fully diffuse ($\alpha_{\mathrm{d,s,i}}$). For the plastic-mulch surface, net radiation was computed via:

$$
\begin{aligned}
R_{\mathrm{n,m,i}} &= R_{\mathrm{S,m,i}} + R_{\mathrm{L,m,i}} \\
R_{\mathrm{S,m,i}} &= \alpha_{\mathrm{d,m,i}}(F_{\mathrm{d,i}}R_{\mathrm{d}} + F_{\mathrm{s,i}}R_{\mathrm{S,g}}) + \alpha_{\mathrm{b,m,i}}(\delta_{\mathrm{i}})F_{\mathrm{b,i}}R_{\mathrm{b}} \\
R_{\mathrm{L,m,i}} &= \alpha_{\mathrm{L,m,i}}(F_{\mathrm{d,i}}R_{\mathrm{L,d}} + F_{\mathrm{s,i}}R_{\mathrm{L,g}}) - 2\varepsilon_{\mathrm{m,i}}\sigma T_{\mathrm{ce}}{}^{4}
\end{aligned}
\tag{3.36}
$$

where radiation emitting from both sides of the plastic mulch ($n_{\mathrm{sides}} = 2$) was accounted for.

3.2.7 Integration of nodal fluxes

The variables e_{ce} and T_{ce} are functions of the bulk latent and sensible heat fluxes from the surface, respectively. Using the evaporation fluxes from each node from the previous time step (E_{i}), the water vapour pressure at common exchange height is:

$$
e_{\mathrm{ce}} = r_{\mathrm{a1}}\sum_{\mathrm{i=1}}^{N_{\mathrm{surf}}}(E_{\mathrm{i}}w_{\mathrm{i}}/\cos\mu_{\mathrm{i}})/\sum_{\mathrm{i=1}}^{N_{\mathrm{surf}}}(w_{\mathrm{i}}) + e_{\mathrm{a}} \tag{3.37}
$$

where w_i is the width of the surface patch which node *i* represents, e_a is the vapour pressure at reference height and N_{surf} is the number of upper boundary nodes. Similarly, using nodal temperatures of the previous time step, the air temperature at common exchange height is:

$$T_{ce} = \frac{r_{a1} \sum_{i=1}^{N_{surf}} (T_i / r_{h,i} w_{r,i}) + T_a}{r_{a1} \sum_{i=1}^{N_{surf}} (1 / r_{h,i} w_{r,i}) + 1} \qquad \text{with} \quad w_{r,i} = w_i / \sum_{i=1}^{N_{surf}} (w_i \cos \mu_i) \tag{3.38}$$

with reference height temperature T_a. As for the vapour flux, r_{a1} is corrected by the horizontal width of the ridge system due to the *cos* μ_i term. The temperature T_i represents $T_{s,i}$ in cases of uncovered nodes and $T_{m,i}$ for covered ones.

If a part of the surface is covered by plastic mulch, it was assumed that all intercepted precipitation which exceeds the water capacity limit is routed to the first two uncovered nodes. Likewise for uncovered ridges, if the infiltration rate was lower than the precipitation rate, then the ponding water at the top and slopes of the ridge will be distributed by the same approach. The water capacity limit was described as function of wet ability and slope:

$$d_{w,max} = d_{w,h} - (d_{w,h} - d_{w,v}) \sin \mu \tag{3.39}$$

with maximum liquid water depths at horizontal and vertical aligned plastics, $d_{w,h}$ and $d_{w,v}$, respectively. The parameters given in Table 3.2 were fitted to data obtained by SCHULTZ (1997).

Table 3.2 Fitted water capacities of horizontal ($d_{w,h}$) and vertical ($d_{w,v}$) inclined plastics with prevailing drop and film condensation modes.

Condensation mode	$d_{w,h}$ [µm]	$d_{w,v}$ [µm]	*n*
drop wise	166	92	12
film wise	67	24	8

According to Table 3.2, highly wettable plastics with film condensation can retain roughly only one-third of the water volume at the lower or upper sides compared to

plastics with drop formation. If the liquid water capacity is exceeded at the lower side of the plastic, part of the surplus water is routed laterally downwards while the remaining water drips back to the soil. The contributions between dripping and drainage is largely unknown, but the following relation reproduces at least the general trend given by SCHULTZ (1997) for fraction of dripping f_{drip} of water exceeding the capacity of the plastic surface.

$$f_{\mathrm{drip}} \approx \begin{cases} \cos^2 \mu & \text{drop mode} \\ \cos^2 \min(2.2\mu, 0.5\pi) & \text{film mode} \end{cases} \tag{3.40}$$

where perfect drainage is assumed and all slipping water is routed to the deepest plastic covered node and added to it's infiltration flux.

The short-wave radiation balance in Eqs. (3.8) and (3.35) includes the mean reflected short-wave radiation flux which is amenable to absorption by nodes. This flux was semi-empirically approximated using Eq. (3.8) and weighting each reflected radiation with $F_{\mathrm{s,i}}\, w_{\mathrm{i}}$ as horizontal surfaces at the top do not supply radiation to lower located surfaces.

$$R_{\mathrm{S,g}} = \frac{\sum_{\mathrm{i=1}}^{N_{\mathrm{surf}}} \left[F_{\mathrm{s,i}} w_{\mathrm{i}} \left(\rho_{\mathrm{d,i}} (F_{\mathrm{d,i}} R_{\mathrm{d}} + F_{\mathrm{s,i}} R_{\mathrm{S,g}}) + \rho_{\mathrm{b,i}} F_{\mathrm{b,i}} R_{\mathrm{b}} \right) \right]}{\sum_{\mathrm{i=1}}^{N_{\mathrm{surf}}} \left[F_{\mathrm{s,i}} w_{\mathrm{i}} \right]} \tag{3.41}$$

$$\text{with} \quad \rho_{\mathrm{d,i}} = \begin{cases} 1 - \alpha_{\mathrm{d,i}} \\ 1 - \alpha_{\mathrm{d,s,i}} - \alpha_{\mathrm{d,m,i}} \end{cases}, \qquad \rho_{\mathrm{b,i}} = \begin{cases} 1 - \alpha_{\mathrm{b,i}} & \text{uncov.} \\ 1 - \alpha_{\mathrm{b,s,i}} - \alpha_{\mathrm{d,m,i}} & \text{cov.} \end{cases}$$

solving Eq. (3.41) for $R_{\mathrm{S,g}}$ yields:

$$R_{\mathrm{S,g}} = \frac{\sum_{\mathrm{i=1}}^{N_{\mathrm{surf}}} \left[F_{\mathrm{s,i}} w_{\mathrm{i}} \left(\rho_{\mathrm{d,i}} F_{\mathrm{d,i}} R_{\mathrm{d}} + \rho_{\mathrm{b,i}} F_{\mathrm{b,i}} R_{\mathrm{b}} \right) \right]}{\sum_{\mathrm{i=1}}^{N_{\mathrm{surf}}} \left[F_{\mathrm{s,i}} w_{\mathrm{i}} \right] - \sum_{\mathrm{i=1}}^{N_{\mathrm{surf}}} \left[{F_{\mathrm{s,i}}}^2 w_{\mathrm{i}} \rho_{\mathrm{d,i}} \right]} \tag{3.42}$$

Using the same approach for Eq. (3.19), an equation for the mean long-wave radiation

flux leaving the ground which is amenable to interception by other nodes can be produced.

$$R_{\mathrm{L,g}} = \frac{\sum_{\mathrm{i=1}}^{N_{\mathrm{surf}}} \left[F_{\mathrm{s,i}} w_{\mathrm{i}} \left(\rho_{\mathrm{L,i}} F_{\mathrm{d,i}} R_{\mathrm{L,d}} + R_{\mathrm{L,e,i}} \right) \right]}{\sum_{\mathrm{i=1}}^{N_{\mathrm{surf}}} \left[F_{\mathrm{s,i}} w_{\mathrm{i}} \right] - \sum_{i=1}^{N_{\mathrm{surf}}} \left[F_{\mathrm{s,i}}^2 w_{\mathrm{i}} \rho_{\mathrm{L,i}} \right]} \text{ with } \rho_{\mathrm{L,i}} = \begin{cases} 1 - \varepsilon_{\mathrm{s,i}} & \text{uncov.} \\ 1 - \alpha_{\mathrm{L,s,i}} - \alpha_{\mathrm{L,m,i}}, & \text{cov.} \end{cases} \tag{3.43}$$

where the emitted long-wave flux $R_{\mathrm{L,e,i}}$ of a covered node i was derived from the solution of the residual term of the plastic [$R_{\mathrm{e,m,i}}$, Eq. (3.34)].

$$R_{\mathrm{L,e,i}} = \begin{cases} \varepsilon_{\mathrm{s,i}} \sigma T_{\mathrm{s,i}}{}^4 & \text{uncov.} \\ R_{\mathrm{e,m,i}}\, \tau_{\mathrm{m,i}} / \varepsilon_{\mathrm{m,i}} + \varepsilon_{\mathrm{m,i}} \sigma T_{\mathrm{m,i}}{}^4 & \text{cov.} \end{cases} \tag{3.44}$$

3.2.8 Interfacing nodal energy balances with 2DSOIL

2DSOIL is a modular and available two-dimensional soil simulator, which can be interfaced with plant models. It simulates heat, water, solute and gas movement and other processes as nitrogen transformations and chemical interactions. The aim here is just to give a brief overview of the important relationships used in 2DSOIL to simulate the heat and water transfer, while more details have been given elsewhere (TIMLIN *et al.*, 1996).

The two-dimensional transport of heat in a variable saturated soil which accounts for diffusion of heat and advection due to water fluxes is given by:

$$\frac{\partial C_s T_s(x,z,t)}{\partial t} = \frac{\partial}{\partial x}\left(k_s \frac{\partial T_s}{\partial x} \right) + \frac{\partial}{\partial z}\left(k_s \frac{\partial T_s}{\partial z} \right) - \frac{\partial (q_x C_w T_s)}{\partial x} - \frac{\partial (q_z C_w T_s)}{\partial z} \tag{3.45}$$

with soil temperature (T_{s}), heat capacity of water (C_{w}) and the horizontal and vertical water fluxes (q_{x}, q_{z}). The volumetric heat capacity of soil (C_{s}) is calculated after the approach of DE VRIES (1966) but and the thermal conductivity (k_{s}) was calculated after CAMPBELL *et al.* (1994). Equation (3.45) is numerically solved using the Galerkin finite

element method with linear basis functions and triangular elements.

The two-dimensional liquid water movement is described by Richards' equation

$$\frac{\partial \theta(x,z,t)}{\partial t} = \frac{\partial}{\partial x}\left(k(h)\frac{\partial h}{\partial x} \right) + \frac{\partial}{\partial z}\left(k(h)\left(\frac{\partial h}{\partial z} \right) + 1 \right) - S \tag{3.46}$$

with volumetric water content (θ), pressure head (h) and a water extraction term (S). Any contributions from water vapour transport are assumed to be negligible. The necessary parameterisations to solve Eq. (3.46) are the hydraulic conductivity function ($k(h)$) and the water retention function $\theta(h)$. The numerical solution of Eq. (3.46) is obtained by the same approach as for Eq. (3.45).

The user has to provide a geometrical description of the problem as a grid of finite elements, several soil properties (water retention parameters, bulk density, contents of clay, sand and organic matter, saturated conductivity) and specific energy balance terms for each upper boundary node. At the atmospheric boundary 2DSOIL allows flux type boundary conditions to be used. The required nodal inputs per time step of the atmospheric forcing are the potential evaporation rate $E_{p,i}$, the rate of precipitation P_i and so called b_t and G_t terms. The last two terms are derived from the nodal energy balance by the relation:

$$G_i = -b_{t,i} T_{s,i} + G_{t,i} \tag{3.47}$$

where G_i is the realized soil heat flux of the boundary node at temperature $T_{s,i}$. The solutions for the b_t and G_t terms were derived by solving either Eq. (3.23) or Eq. (3.29) for G_i ($\lambda_w E$ is omitted from the energy balance as a matter of implementation, see TIMLIN *et al.* (1996)) and collecting all terms on the right side which are belonging to $T_{s,i}$ as b_t and the remaining terms are contributed to G_t. This procedure resulted for an uncovered node the following solution for $b_{t,i}$ and $G_{t,i}$

$$\begin{aligned} b_{t,i} &= \rho_{air} C_{air} / r_{h,r,i} / \cos\mu_i \\ G_{t,i} &= (R_{n,s,i} + \rho_{air} C_{air} / r_{h,r,i} T_{ce}) / \cos\mu_i \end{aligned} \tag{3.48}$$

where the cosine of slope correction is required as 2DSOIL relates internally the nodal fluxes only to the horizontal width of the node. 2DSOIL removes internally the energy required for evaporation ($\lambda_w E$) from $G_{t,i}$. If the resulting surface water potential is lower than a defined limit (*HritA*) only the evaporation rate which satisfies *HcritA* is allowed and more energy will be accordingly available for soil heating.

For covered surface nodes the same procedure yields:

$$\begin{aligned} b_{t,i} &= (c_{s1,i} c_{m2,i} - c_{m1,i} c_{s2,i}) / c_{m2,i} / \cos\mu_i \\ G_{t,i} &= (R'_{n,s,i}\, c_{m2,i} - R'_{n,m,i}\, c_{m1,i} + (c_{m1} c - c_{m2,i} c_{b1,i}) T_{ce}) / c_{m2,i} / \cos\mu_i + \lambda_w E_{sm,i} \end{aligned}$$

$$\begin{aligned} c_{b1,i} &= a_{1,i} a_3 + a_3 \varepsilon_{s,i} (a_{1,i} \rho_{L,i} / \varepsilon_{m,i} - 1) \\ c_{s1,i} &= -a_3 \varepsilon_{s,i} (a_{1,i} \rho_{L,i} / \varepsilon_{m,i} - 1) + \rho_{air} C_{air} \left(r_{c,h}{}^{-1} + \frac{\Delta r h_{s,i}}{y(r_{c,v} + r_{s,l})} \right) \\ c_{m1,i} &= -a_{1,i} a_3 - \rho_{air} C_{air} \left(r_{c,h}{}^{-1} + \frac{\Delta r h_{s,i}}{y(r_{c,v} + r_{s,l})} \right) \\ c_{b2,i} &= a_{1,i} a_3 + a_3 a_{2,i} - \rho_{air} C_{air} \left(r_{h,r,i}{}^{-1} + \frac{\Delta}{y(r_{v,i} + r_{s,u})} \right) \\ c_{s2,i} &= c_{m1,i} \\ c_{m2,i} &= -a_3 a_{2,i} + \rho_{air} C_{air} \left(r_{h,r,i}{}^{-1} + r_{c,h}{}^{-1} + \frac{\Delta}{y(r_{v,i} + r_{s,u})} \right) + \frac{\Delta r h_{s,i}}{y(r_{c,v} + r_{s,l})} \end{aligned} \tag{3.49}$$

The *a* terms in Eq. (3.49) are given by

$$a_{1,i} = \frac{\varepsilon_{s,i}\varepsilon_{m,i}}{1-\rho_{L,i}(1-\varepsilon_{s,i})}$$
$$a_{2,i} = \frac{\varepsilon_{m,i}^2(1-\varepsilon_{s,i})}{1-\rho_{L,i}(1-\varepsilon_{s,i})} \qquad (3.50)$$
$$a_3 = 4\sigma T_{ce}^{\ 3}$$

The net radiation terms are given from modified energy balance terms arising from linearization's of latent and long-wave fluxes around at common exchange height temperature.

$$R'_{n,s,i} = R_{n,s,i} + \sigma b_{1,i}(1+e_{s,i}\rho_{L,i}/\varepsilon_{m,i})T_{ce}^{\ 4} - \frac{\rho_{air}C_{air}(rh_{s,i}-1)e^*(T_m)}{y(r_{c,v}+r_{s,l})}$$
$$R'_{n,m,i} = R_{n,m,i} + \frac{\rho_{air}C_{air}(rh_{s,i}-1)e^*(T_m)}{y(r_{c,v}+r_{s,l})} - \frac{\rho_{air}C_{air}(e^*(T_{ce})-e_{ce})}{y(r_{v,i}+r_{s,u})} + (b_{2,i}+b_{1,i})\sigma T_{ce}^{\ 4} \qquad (3.51)$$

The potential evaporation rate of uncovered soil nodes is specified as $E_{p,i} = E_i/\cos\mu_i$. The precipitation flux is assigned as measured for horizontal surfaces.

For covered nodes, evaporation and precipitation terms submitted to 2DSOIL were calculated from the previous time step values according to:

$$E_{p,i} = \begin{cases} (E_{sm,i} - f_{drip}w_e)/\cos\mu_i & E_{sm,i} > 0 \\ 0 & E_{sm,i} \le 0 \end{cases} \qquad (3.52)$$
$$\text{with } w_e = \max(E_{sm,i} - (d_{w,max} - d_{w,l,i})/\Delta_t, 0)$$

where w_e is the condensation flux exceeding the plastic mulch water capacity in μm d^{-1}, Δ_t is time step length in d and E_{sm} has units μm d^{-1}.

$$P_i = \begin{cases} \min(-E_{sm,i}, d_{w,l,i}/\Delta_t)/\cos\mu_i 10^{-4} & E_{sm,i} < 0 \\ f_{drip}\, w_e/\cos\mu_i 10^{-4} & E_{sm,i} \ge 0 \end{cases} \qquad (3.53)$$

with corresponding updates on actual water depth at the plastic lower side $d_{w,l,i}$:

$$d_{\mathrm{w,l,i}} = \begin{cases} \min(E_{\mathrm{sm,i}}{}' \Delta_t + d_{\mathrm{w,l,i}}{}', d_{\mathrm{w,max}}) & E_{\mathrm{sm,i}} \geq 0 \\ \max(E_{\mathrm{sm,i}}{}' \Delta_t + d_{\mathrm{w,l,i}}{}', 0) & E_{\mathrm{sm,i}} < 0 \end{cases} \tag{3.54}$$

where the prime ' denotes quantities from previous time step.

The change of water depth at the upper side of the plastic was calculated similarly:

$$d_{\mathrm{w,u,i}} = \begin{cases} \min(d_{\mathrm{w,u,i}}{}' - E_{\mathrm{mb,i}}{}' \Delta_t, d_{\mathrm{w,max}}) & E_{\mathrm{mb,i}} < 0 \\ \max(d_{\mathrm{w,u,i}}{}' - E_{\mathrm{mb,i}}{}' \Delta_t, 0) & E_{\mathrm{mb,i}} \geq 0 \end{cases} \tag{3.55}$$

where E_{sm} has units μm d^{-1}.

For each time step, the drainage water $(1\text{-}f_{drip})w_e$ is routed to the lowermost covered node and released as precipitation P_{i}, accordingly.

Code modifications on 2DSOIL

The code of 2DSOIL has been modified to enable the use of different depths of lower boundaries for the water and heat transfer modules. The depth of the ground water table (d_{gw}) can now be located at any distance between the surface and the lower boundary for heat transfer (d_{ht}) which was set to 10 m depth.

2DSOIL implements originally the theory of DE VRIES (1963) to predict the soil thermal conductivity k_{s}. This module was replaced by the modified version of CAMPBELL *et al.* (1994) as the original formulation of the de Vries model was found to overpredict thermal conductivity (KIMBALL *et al.*, 1976, HORTON & WIERENGA, 1984). As the thermal conductivity of the solid fraction was treated as an adjustable parameter by CAMPBELL *et al.* (1994), it was derived here using an estimation of the quartz content X_{q} on the soil solid fraction from a data set given in RÜHLMANN *et al.* (2005).

$$X_{\mathrm{q}} = \frac{0.89 X_{\mathrm{sand}} + 0.54 X_{\mathrm{silt}}}{X_{\mathrm{hu}} + 1} \tag{3.56}$$

where X_{sand} and X_{silt} are the mass fractions of sand and silt, respectively. Applying a geometric averaging procedure as stated by FAROUKI (1986) yields the combined thermal conductivity of solids (k_{sl}) via geometric averaging of the contributing materials.

$$k_{\mathrm{sl}} = k_{\mathrm{q}}^{\,X_{\mathrm{q}}} k_{\mathrm{o}}^{\,X_{\mathrm{hu}}} k_{\mathrm{mi}}^{\,1-X_{\mathrm{q}}-X_{hu}} \tag{3.57}$$

where the thermal conductivities of quartz, organic matter and other minerals (k_{q}, k_{o}, k_{mi}) were estimated from TARNAWSKI *et al.* (2000).

3.3 Modelling absorptances for covered soil and plastic mulch

3.3.1 Derivation of absorptances

The plastic mulch absorbs the diffuse downward radiation flux (R_{d}) incident at the upper side and an upward radiation flux ($R_{\mathrm{d}\uparrow}$) at the lower side. Using similar arguments for the soil, the diffuse absorptivities are given as:

$$\alpha_{\mathrm{d,s}} = \frac{1-\rho_{\mathrm{s}}}{R_{\mathrm{d}}} R_{\mathrm{d}\downarrow} \qquad \alpha_{\mathrm{d,m}} = \frac{1-\rho_{\mathrm{d}}-\tau_{\mathrm{d}}}{R_{\mathrm{d}}} (R_{\mathrm{d}\uparrow} + R_{\mathrm{d}}) \tag{3.58}$$

where τ_{d} and ρ_{d} are the diffuse transmissivities and reflectivities of plastic mulch, respectively, and ρ_{s} is the soil albedo. A simple equation system can be stated for the radiation fluxes below a plastic mulch cover.

$$\begin{aligned} R_{\mathrm{d}\downarrow} &= \tau_{\mathrm{d}} R_{\mathrm{d}} + \rho_{\mathrm{d}} R_{\mathrm{d}\uparrow} \\ R_{\mathrm{d}\uparrow} &= \rho_{\mathrm{s}} R_{\mathrm{d}\downarrow} \end{aligned} \tag{3.59}$$

where solutions for both fluxes are:

$$R_{d\uparrow} = \frac{\rho_s \tau_d R_d}{1-\rho_s \rho_d} \qquad R_{d\downarrow} = \frac{\tau_d R_d}{1-\rho_s \rho_d} \tag{3.60}$$

Substitution of Eq. (3.60) into Eq. (3.58) provides the required expressions for the diffuse absorptivities.

$$\alpha_{d,s} = \frac{\tau_d (1-\rho_s)}{1-\rho_s \rho_d} \qquad \alpha_{d,m} = (1-\rho_d-\tau_d)\left[1+\frac{\tau_d \rho_s}{1-\rho_s \rho_d}\right] \tag{3.61}$$

Using an analogue procedure for the direct radiation component yields:

$$\alpha_{b,s} = \frac{\tau_b(\delta)(1-\rho_s)}{1-\rho_s \rho_d} \quad \alpha_{b,m} = (1-\rho_b(\delta)-\tau_b(\delta)) + \frac{\tau_b(\delta)\rho_s(1-\rho_d-\tau_d)}{1-\rho_s \rho_d} \tag{3.62}$$

with the angular-dependent direct reflectivity $\rho_b(\delta)$ and transmissivity $\tau_b(\delta)$ of the plastic mulch. Identical solutions were previously derived from infinite series expansions of multiple reflections (DE LUCA & RUOCCO, 2000; HAM & KLUITENBERG, 1994).

The absorptivity parameters of long-wave radiation are essentially identical to the terms given for the total diffuse absorptivity. However, common notation includes the emissivity ($\varepsilon = 1 - \tau - \rho$) of the material. Therefore, Eq. (3.61) was adapted to define the total long-wave absorptivities.

$$\alpha_{L,s} = \frac{\tau_L \varepsilon_s}{1-\rho_L(1-\varepsilon_s)} \quad \alpha_{L,m} = \varepsilon_m \left[1+\frac{\tau_L \varepsilon_s}{1-\rho_L(1-\varepsilon_s)}\right] \tag{3.63}$$

3.3.2 Modelling directional transmissivity and reflectivity

Several parameters used in the preceding section are explicit ($\tau_b(\delta)$, $\rho_b(\delta)$) or implicit (τ_d, ρ_d, τ_L, ρ_L) functions of the angle of radiation incidence, where the diffuse and long-wave radiation properties are obtained from a directional averaging procedure according to:

$$P_{d/L} = 2\int_0^{\frac{\pi}{2}} \cos\delta \sin\delta \, P_b(\delta)\, d\delta \tag{3.64}$$

with $P_{d/L}$ representing an averaged hemispherical quantity and P_b the corresponding explicit or directional parameter (INCROPERA & DEWITT, 2002).

The problem was now to specify the directional behaviour of short- and long-wave transmissivities and reflectivities from measured values at normal incidence. This was solved by using an approach from window design research (RUBIN *et al.*, 1998). Assuming an ideal dielectric or conductor, which is clean, smooth and without internal density gradients, the Fresnel theory can be used to describe the directional dependence of interfacial reflectivities and internal transmissivities (Fig. 3.5).

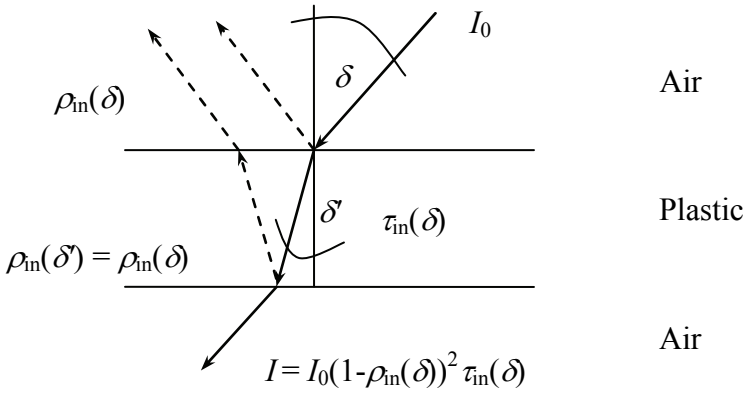

Fig. 3.5 Non-reflected (solid line) and single reflected light paths through an air – plastic-air interface with resulting intensity of non-reflected radiation at the plastic lower side *I*. The light beam is either mirror-like reflected or refracted with angle δ' as according to Snells' law. Internal transmissivities and reflectivities are $\tau_{in}(\delta)$ and $\rho_{in}(\delta)$, respectively

Considering a simple air-plastic-air configuration (Fig. 3.5), RUBIN *et al.* (1998) provided the solution for the required external transmissivities and reflectivities which result after multiple reflections:

$$\tau_b(\delta) = \frac{(1-\rho_{in}(\delta))^2 \tau_{in}(\delta)}{1-\rho_{in}(\delta)^2 \tau_{in}(\delta)^2} \quad \rho_b(\delta) = \rho_{in}(\delta) + \frac{(1-\rho_{in}(\delta))^2 \rho_{in}(\delta) \tau_{in}(\delta)^2}{1-\rho_{in}(\delta)^2 \tau_{in}(\delta)^2} \tag{3.65}$$

where the subscript in indicates an internal quantity. Solving Eq. (3.65) for the internal quantities yields (RUBIN *et al.*, 1998):

$$\rho_{\mathrm{in}}(\delta)=\frac{x-\left(x^2-4(2-\rho_{\mathrm{b}}(\delta))\rho_{\mathrm{b}}(\delta)\right)^{0.5}}{2-(2-\rho_{\mathrm{b}}(\delta))} \quad \tau_{\mathrm{in}}(\delta)=\frac{\rho_{\mathrm{b}}(\delta)-\rho_{\mathrm{in}}(\delta)}{\rho_{\mathrm{in}}(\delta)\tau_{\mathrm{b}}(\delta)} \qquad (3.66)$$

$$\text{with} \quad x=\tau_{\mathrm{b}}(\delta)^2-\rho_{\mathrm{b}}(\delta)^2+2\rho_{\mathrm{b}}(\delta)+1$$

At normal incidence ($\delta = 0$), the complex refractive index ($n = n_{\mathrm{r}} + i\, n_{\mathrm{im}}$) of the specific material can be derived from the calculated internal quantities [Eq. (3.66)].

$$n_{\mathrm{r}}=\frac{1+\rho_{\mathrm{in}}(0)+\left(4\rho_{\mathrm{in}}(0)-(\rho_{\mathrm{in}}(0)n_{\mathrm{im}})^2+2\rho_{\mathrm{in}}(0)n_{\mathrm{im}}{}^2-n_{\mathrm{im}}{}^2\right)^{0.5}}{1-\rho_{\mathrm{in}}(0)}, \quad n_{\mathrm{im}}=\frac{-\lambda\ln(\tau_{\mathrm{in}}(0))}{4\pi d_{\mathrm{m}}} \qquad (3.67)$$

with real (n_{r}) and imaginary (n_{im}) parts of refractive index, the thickness of the plastic d_{m} and the wave length λ. Equation (3.67) differs from the expression published by RUBIN *et al.* (1998) as it is also valid for strongly absorbing materials ($n_{\mathrm{im}} >> 0$).

The directional dependence of internal reflection of a light ray striking a surface with a refractive index n' from a medium with refractive index n is given by the Fresnel terms for parallel polarized ($\rho_{\mathrm{in}}^{\mathrm{p}}$) and transverse polarised ($\rho_{\mathrm{in}}^{\mathrm{t}}$) light, respectively.

$$\rho_{\mathrm{in}}^{\mathrm{p}}(\delta)=\left|\frac{n'\cos\delta-n\cos\delta'}{n'\cos\delta+n\cos\delta'}\right|^2, \quad \rho_{\mathrm{in}}^{\mathrm{t}}(\delta)=\left|\frac{n\cos\delta-n'\cos\delta'}{n\cos\delta+n'\cos\delta'}\right|^2 \qquad (3.68)$$

which is calculated in the complex domain. The internal transmissivity was given by RUBIN *et al.* (1998) and does not depend on the polarisation state:

$$\tau_{\mathrm{in}}(\delta)=\exp\left(\frac{-4\pi n_{\mathrm{r}}^{'}d_{\mathrm{m}}^{'}}{\lambda\cos\delta^{'}}\right), \quad \cos\delta'=\left(1-\frac{n_{\mathrm{r}}^2\sin^2\delta}{n_{\mathrm{r}}^{'2}}\right)^{0.5} \qquad (3.69)$$

where the cosine refraction angle ($\cos\delta'$) is derived from Snell's law. Finally, as the polarisation state of light fluctuates randomly under natural conditions (LO *et al.*, 1995), the external transmissivities and reflectivities are derived from Eq. (3.65) as average of

the results for parallel and transverse polarisation states.

There are occasionally circumstances were Fresnels' theory is not appropriate, *e.g.* for plastics which have dust deposits, having rough surfaces or internal material irregularities. In such cases, it is likely that a simpler relation from computational visualisation is more valid, such as the one proposed by SCHLICK (1993):

$$\rho(\delta) = \rho(0) + (1 - \cos(\delta))^5 (1 - \rho(0)) \tag{3.70}$$

with a reasonable feedback on transmission being:

$$\tau(\delta) = \exp\left(\frac{\ln(\tau(0)/(1-\rho(0))}{\cos\delta'} \right) (1 - \rho(\delta)) \tag{3.71}$$

If environmental conditions are favourable for dew formation at the lower side of the plastic mulch, which may always occur for highly transmitting plastics (short-wave range) and only during the night for low transmitting plastics, then the resulting transmissivities and reflectivities can be derived as function of incidence angle and water film thickness ($d_{w,l}$). The internal radiation fluxes can then be expressed by the following equation system, where the radiation is incident from the dry air-plastic side with intensity 1:

$$\begin{aligned}
R_{m\downarrow} = &\quad (1-\rho_{in,1})\tau_{in,m} + \rho_{in,1}\tau_{in,m}R_{m\uparrow} \\
R_{m\uparrow} = &\quad R_{m\downarrow}\rho_{in,2}\tau_{in,m} + R_{w\uparrow}(1-\rho_{in,2})\tau_{in,m} \\
R_{w\downarrow} = &\quad R_{m\downarrow}(1-\rho_{in,2})\tau_{in,w} + R_{w\uparrow}\rho_{in,2}\tau_{in,w} \\
R_{w\uparrow} = &\quad R_{w\downarrow}\rho_{in,3}\tau_{in,w}
\end{aligned} \tag{3.72}$$

with internal reflectivities of the air-plastic, plastic-water and water-air interfaces, $\rho_{in,1}$, $\rho_{in,2}$ and $\rho_{in,3}$ respectively, internal transmissivities of the plastic and water, $\tau_{in,m}$ and $\tau_{in,w}$, respectively, the instant radiation fluxes in the vicinity below the upper side, $R_{m\uparrow}$, and above the lower side, $R_{m\downarrow}$, of the plastic, and below the upper side, $R_{w\uparrow}$, and above the lower side, $R_{w\downarrow}$, of the water film (arrows indicate downward or upward fluxes, respectively). The external transmissivity through the wetted film is then $\tau_b = (1-\rho_{in,3})$ $R_{w\downarrow}$ and the reflectivity is given by $\rho_b = (1-\rho_{in,1})$ $R_{m\uparrow} + \rho_{in,1}$. Solving Eq. (3.72) for both

fluxes gives:

$$\tau_b = \frac{(1-\rho_{in,3})\tau_{in,m}\tau_{in,w}(1-\rho_{in,2}-\rho_{in,1}(1-\rho_{in,2}))}{1-\rho_{in,2}\rho_{in,3}-\tau_{in,m}^2\left\{\rho_{in,1}\rho_{in,3}\tau_{in,w}^2(1-2\rho_{in,2})-\rho_{in,1}\rho_{in,2}\right\}}$$
$$\rho_b = \frac{(1-\rho_{in,1})\tau_{in,m}^2\left\{\rho_{in,2}(1-\rho_{in,1})+\tau_{in,w}^2(\rho_{in,3}(1-2\rho_{in,1})-\rho_{in,1}\rho_{in,3}(1-2\rho_{in,2}))\right\}}{1-\rho_{in,2}\rho_{in,3}-\tau_{in,m}^2\left\{\rho_{in,1}\rho_{in,3}\tau_{in,w}^2(1-2\rho_{in,2})-\rho_{in,1}\rho_{in,2}\right\}}+\rho_{in,1} \quad (3.73)$$

Again Eq. (3.73) must be calculated for both polarisation states of light and averaged accordingly. From reflection and transmission spectra of the considered plastic and water, the weighted reflectivities and transmissivities are calculated for the short-wave (0.4 – 3 μm) and long-wave (3 - 100 μm) range using the Planck function. Using these weighted transmissivities and reflectivities at normal incidence, the refraction index is derived from Eq. (3.67). After that, the required internal transmissivities and reflectivities ($\tau_{in,m}$, $\tau_{in,w}$, $\rho_{in,1}$, $\rho_{in,2}$, $\rho_{in,3}$) are calculated using Eqs. (3.68) and (3.69) with the derived refraction index. For the short-and long-wave ranges, mean characteristic wave lengths of 0.7 μm and 10 μm were selected for calculations, respectively. The computed impacts of thin water films on directional transmission and reflection of short- and long-wave radiation are depicted in Fig. 3.6 and Fig. 3.7 for a polyethylene-based plastic with an adhering liquid water film.

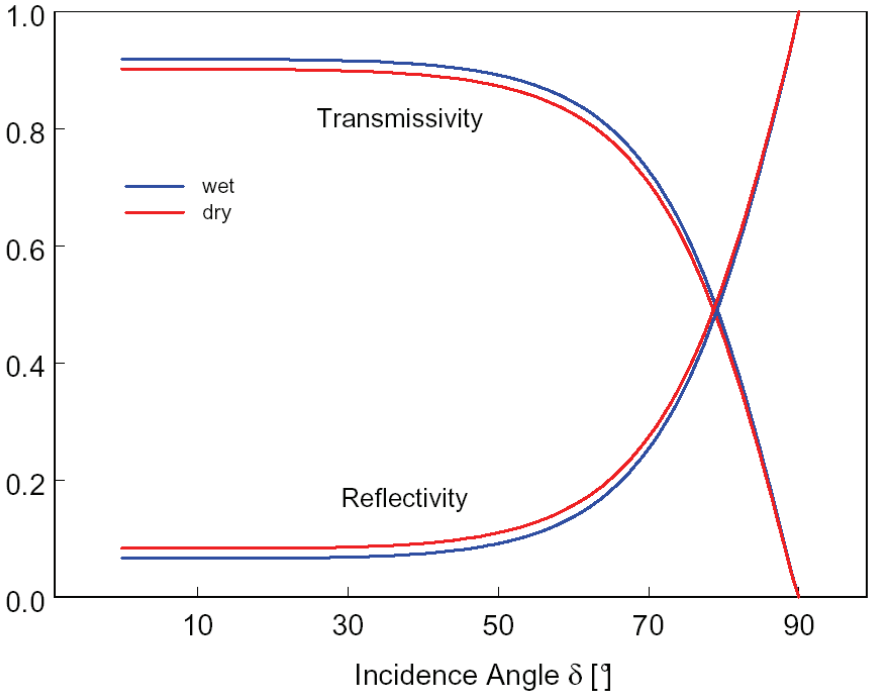

Fig. 3.6 Computed directional dependence of short-wave radiation transmission and reflection for a polyethylene plastic covered by a liquid water film at the lower side (d_m = 100 µm, $d_{w,l}$ = 15 µm, λ = 0.7 µm, plastic: n_r = 1.526, n_{im} = 8.4 10^{-6}, water: n_r = 1.33, n_{im} ~ 0.0).

As seen in Fig. 3.6, the solar transmissivity slightly increased by 1.8% for wetted plastics (directional average), whereas the reflectivity decreased by the same extent. The water film acts as an anti-reflection layer due to its lower real refraction index compared to the plastic. POLLET and PIETERS (2000) obtained similar results for directional transmissivity of an anti-drop low density polyethylene plastic (LDPE), where film condensation is the prevailing condensation mode. However, they detected no statistical difference between dry and wet transmissivities.

For other types of plastics, drop condensation is to be anticipated and can lead to diverse directional transmission responses depending on actual drop shape (POLLET & PIETERS, 2000). Overall, the hemispherical or directional averaged transmission of those plastics will likely be reduced by about 11-13% (POLLET & PIETERS, 2000). Therefore, directional short-wave transmissivities of plastics with likely drop condensation were reduced by 12% if liquid water was present at the lower side. Conversely, the directional reflectivity was increased accordingly.

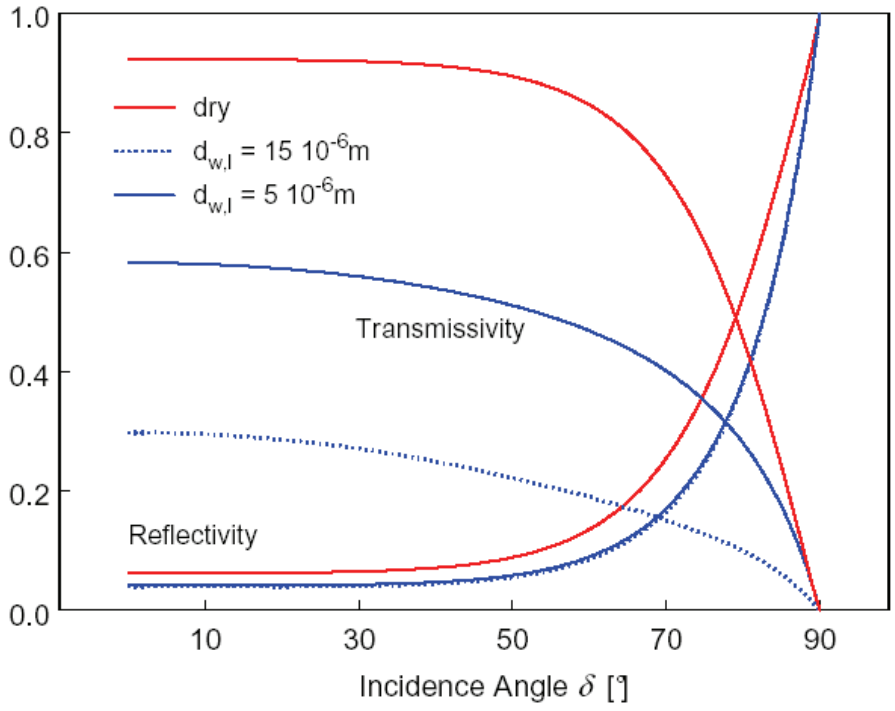

Fig. 3.7 Computed directional dependence of long-wave radiation transmission and reflection for a polyethylene plastic covered by a liquid water film with differing thickness (d_m = 100 µm, $d_{w,l}$ = 5 µm, 15 µm, λ = 10 µm, plastic: n_r = 1.44, n_{im} = 2.64 10^{-3}, water: n_r = 1.214, n_{im} = 0.0534).

As long-wave radiation absorption of liquid water is very efficient (n_{im} = 0.0534 at λ = 10 µm), directional transmissivities are much more affected by the presence of a water film (Fig. 3.7). For plastics exhibiting drop-wise condensation, it is reasonable to interpolate between dry and wet film transmissivities and reflectivities as in contrast to short-wave radiation, absorption within the water drops will be the primary mechanism for transmission losses. Interpolation was carried out using a constant wet area fraction of f_{wet} = 0.55 (BRISCOE & GALVIN, 1991).

Finally, long-wave transmission according to the simplified approach (Eq. (3.71)) was modified by the radiation absorption of the thin water layer, while the corresponding quantity in the short-wave range was left unchanged

$$\tau(\delta)' = \tau(\delta)\exp(-0.625 d_{w,l} / \cos\delta') \tag{3.74}$$

where δ' is the angle of refraction between the plastic and the water layer.

3.4 Discussion

The proposed relation for the sky view factor (F_d, Eq. 3.16) is essentially a refined version of the slope irradiance model proposed by HAY (1979) with added horizon obstructions due to ridges. MAHRER (1982) gave a similar solution to the long-wave radiation interception problem; however, the effect of slope was not taken into consideration. The validity of the proposed F_d formulation was checked using as standard the "all weather sky" luminance model of PEREZ *et al.* (1993) which is the recommended approach to model slope irradiances (VARTIAINEN, 2000). When comparing model results to irradiance measurements of various tilted surfaces with differing slopes and aspects, VARTIAINEN (2000) obtained *RMSEs* of 6%, 9.5% and 12.8% for the Perez model and the Hay model with and without circumsolar radiation treatment, respectively. The larger deviation relative to the Perez model from the simulation test here (10%, Eqs. (3.17) and (3.18) can be explained by the presence of direct radiation in the data set of VARTIAINEN (2000) as well as to a likely increased sensitivity to sky anisotropy if horizon obstructions are included. Regarding these rather small differences between the models and the equally good performance for the long-wave sky view factor, no substantial improvements are possible for the sky view factor model.

After adapting an approach from window design research, the directional radiative properties of plastics were expressed from their usual measured properties at normal incidence. The application of the used Fresnel theory is known to be suitable for different kinds of glasses and highly transmitting plastics. However, whether this approach is also valid for weakly transmitting plastics is unknown. The empirical reflection formula after SCHLICK (1993) might be of equal or more use for non-perfect dielectrics. Clearly, more research is required where measurements of directional reflectivity and transmissivity of plastics are compared to results from different models. Further uncertainties in directional radiative properties arise from liquid drops at the surface of the plastic, which are influenced by the actual drop pattern. As real or simulated drop pattern growth follows well-known scaling laws (MEAKIN, 1992) and the asymptotic drop coverage is strongly related to the receding, advancing and

equilibrium contact angles of drops (ZHAO & BEYSENS, 1995), it might be possible to generalise directional responses for various droplet patterns from coupled drop growth and radiative transfer simulations studies.

The proposed approach to predict the directional radiative response has been extended to a plastic covered by a liquid water film at the lower side and is based on solid theoretical grounds. This extension might also be valid in the long-wave range for plastics with a drop condensation layer, as radiation absorption is the prevailing mode of transmission losses; however, there are as yet no empirical results in the literature to verify this hypothesis.

The theoretical treatment of condensation on the lower side of the plastic, the subsequent saturation of water capacity and the slipping of water on sloped plastics contributes to the understanding of water transfer below plastic mulches, although the suggested relation to predict the fraction of dripping water (Eq. (3.40)) needs to be verified. Ridges covered by a highly transmitting plastic are sometimes observed to be dryer than those covered by an opaque plastic, although both plastics are highly impermeable to water vapour. For a highly transmitting, non-drop plastic, a frequent saturation of liquid water capacity and subsequent slipping of water down the sloped plastic can be anticipated. The dryer the soil the more efficient this transport mechanism will be when compared to the soil drainage process itself. This is because the unsaturated hydraulic conductivity of the soil is decreasing function on soil volumetric water content.

The incidence angle of the precipitation flux is assumed to be normal to the horizontal plane which results in a reduced precipitation for tilted surfaces. This is an approximation as it is known that rain interception of slopes without wind field disturbances follows the same laws as the direct radiation interception (SHARON, 1980). However, without complete information on hourly wind direction along with uncertainties about the instant rain intensity and possible wind field deformations, the applied simplified description of rain interception at normal incidence is retained here. Rain gauge error from wind field deformations around rain gauge orifices was predicted

and the results compare well with experimental data (HABIB *et al.,* 1999). Possibly, similar studies for ridge systems could provide information about the hydrological precipitation at specific ridge positions.

The described model contains only one largely unknown parameter – the common exchange height z_{ce}. This height is thought of as the effective level were vertical heat fluxes of single nodes are no longer independent of each other and are characterised by a mean overall flux. This loss of independence is contributed to the advection of heat, which was considered to be too complex to incorporate as it requires detailed data on wind direction, the horizontal wind field and on two-dimensional turbulent transfer resistances.

3.5 Conclusions

An energy balance model for a two-dimensional ridge surface partly covered by a plastic mulch as well as the interface to a public domain soil simulation model is presented. Previous approaches are modified and extended to include: (1) the circumsolar part of diffuse radiation; and (2) the altered interception of diffuse short- and long-wave radiation due to horizon obstructions and surface slope; and (3) the treatment of directional responses of short- and long-wave reflectivity and transmissivity of dry and wetted plastic mulches.

A simple solution was found for the interception problem under an uniform radiating sky, and an extensive numerical simulation study with broadly varying sky conditions and surface geometries revealed an error of about 10% using this approximation. Similarly simulations for long-wave sky radiation interception highlighted the good predictive quality of the uniform sky solution with errors of about 1%.

A thorough derivation of directional responses of transmissivity and reflectivity of different commonly used plastics is provided. Oblique direct radiation incidence angles due to ridged surfaces were taken into account using a Fresnel theory based approach adapted from window design research and extended to describe the effect of a liquid water film on the inside of the plastic.

Overall, the proposed model represents a fairly general and advanced description of the radiation and energy transfer to soil ridges partly covered with plastic-mulch**.**

4 Simulation of soil heating in ridges partly covered with plastic-mulch - Model calibration and validation

List of Symbols and Abbreviations

c	fraction of sky covered with cloud (0..1)	
C_{air}	specific heat capacity of air	J mol^{-1} K^{-1}
d	zero plane displacement	m
d_{gap}	thickness of the air layer between soil and plastic mulch	m
d_{gw}	depth of ground water table	m
d_{ht}	depth of constant soil temperature	m
E	evaporation flux density	mol m^{-2} s^{-1}
e_a	water vapour pressure of air at reference height	mol m^{-3}
F_d	sky view factor (0..1)	
$h(z)$	water potential of soil with depth z	hPa
h_c	ridge height	m
H	sensible heat flux	W m^{-2}
h_{eq}	parameter of the relative humidity function of upper soil layer	
k	von Kármán constant (0.4)	
$k(h)$	soil hydraulic conductivity function with water potential	cm d^{-1}
K_s	saturated hydraulic conductivity	cm d^{-1}
n_{im}	imaginary part of refraction index	
n_r	real part of refraction index	

Q	ground water recharge rate	cm d^{-1}
r_c	contact resistance to heat transfer between soil and plastic	s m^{-1}
$R_{L,d}$	long-wave sky radiation	W m^{-2}
$R_{L,d,c}$	long-wave sky radiation of clear sky	W m^{-2}
R_S	solar radiation received by a horizontal plane	W m^{-2}
$R_{S,max}$	maximum solar radiation received by a horizontal plane	W m^{-2}
rh_s	relativ humidity of soil air of surface layer	%
$RMSE$	root mean square error	
S_0	solar constant	W m^{-2}
T_a	reference height air temperature	K
T_{ce}	common exchange height air temperature	K
T_m	plastic mulch temperature	K
T_s	soil surface temperature	K
u_a	horizontal wind speed at reference height	m s^{-1}
X_{hu}	soil humus content	g g^{-1}
X_{sand}	soil sand content	g g^{-1}
X_{silt}	soil silt content	g g^{-1}
y	psychrometric constant	mol m^{-3} K^{-1}
z	vertical coordinate	m
z_0	roughness length	m
z_{ce}	common exchange height	m
α	parameter of van Genuchten retention function	cm^{-1}
β	sun elevation angle	degrees
δ	incidence angle, angle between surface normal and light ray	rad

Δ	slope of the saturated vapour pressure temperature function	mol m^{-3} K^{-1}
θ_r	residual soil water content	cm^3 cm^{-3}
θ_s	saturated soil water content	cm^3 cm^{-3}
λ	wave length of radiation	µm
λ_w	latent heat of vaporisation of liquid water	J mol^{-1}
ρ	reflectivity	
ρ_{air}	air density	mol m^{-3}
ρ_b	soil bulk density	g cm^{-3}

4.1 Introduction

This chapter focuses on the calibration and validation of the proposed simulation model from section 3. For our purposes, calibration is understood as setting values to largely unknown or potentially site-specific model parameters, and as the selection of the most appropriate submodels if no independent study clarifies their validity and precision. For the proposed model, only three parameters values need to be established: (1) the thickness of the air layer between the soil and the plastic mulch (d_{gap}) which might differ between sloped and horizontal surfaces; (2) the common exchange height (z_{ce}); and (3) modifying parameter of the function describing the relative humidity of the upper soil layer (h_{eq}). To date, in regards to directional radiative properties of plastics, literature is still not available to enable appropriate selection of submodels of plastics. However, possible options include the application of the Fresnel theory, Schlicks equation of reflection or quite simply ignoring the aspects of directional dependencies.

Moreover, clear guidelines on what constitutes appropriate calibration and validation of a simulation model have not been proposed. However, in the literature, root mean square error (*RMSE*) and mean biased error (*MBE*) are most frequently used. Therefore, both statistics will be used throughout

$$RMSE = \left(\sum_n \left(x_p - x_m \right)^2 / n \right)^{0.5} \qquad MBE = \sum_n \left(x_p - x_m \right) / n$$

where x_p and x_m are predicted and measured variables, respectively.

Ideally, model validation should be performed by comparing predicted data with actual field measurements for each intended application scenario; however, in terms of time and costs, this is not a viable option. However, for mechanistic models, it is usual to extrapolate variables out of the validation context which allows predictions of ‘unproven’ real life scenarios.

The model proposed here was designed to predict soil temperatures hourly within ridges

partly covered by plastic mulch or uncovered. For validation purposes, soil temperatures were taken hourly at various spatial positions for each of the 6 cover treatments (including bare ridges) within each ridge over several months at two sites. The two sites differed mostly in terms of soil humus content. At the Grossbeeren site, a complete two year data set is available. It is reasoned that comparison of predicted data with this data set is sufficient to validate the proposed simulation model.

4.2 Material and methods

4.2.1 Experiment I - site Grossbeeren

Temperature dynamics within soil ridges covered with 5 types of plastic mulches and one uncovered were recorded at the field site of the Institute of Vegetables and Ornamental Crops in Grossbeeren (Germany) over 3 months in both 2001 and 2002. This site is characterised by a sandy soil (Arenic Luvisol, World Reference Base) with contents of 0.8% humus, 91% sand and 4.6% clay. Standard meteorological inputs were available from a weather station located 50 m away from the site (air temperature T_a, vapour pressure e_a, global radiation R_s and horizontal wind speed u_a at 2 m and precipitation P at 1 m).

Various types of plastic mulches were tested and are listed in Table 4.1. These plastic mulches were selected as they are commonly used to cover ridges for crop production systems, *e.g.* white asparagus spears. These are mainly co-extruded plastics made from polyethylene and additives (modification of UV blockage, colour pigments, surface energy). The ‘White/Black’ plastic is also frequently used to accelerate or slow down spear growth by changing the sun-facing sides, which subsequently affects soil temperature. As asparagus spears change their colour from white to blue/purple when exposed to short-wave radiation, a combination plastic, such as the ‘Thermo Plus’ type, helps prevent exposure and has a black non-transparent central top part and transparent sides (Table 4.1).

Table 4.1 Characteristics and measured properties of the 5 plastic mulches used (τ normal transmissivity, ρ normal reflectivity)

Trade name	Label	Appearance	Short-wave range		Long-wave range		Width	Thick-ness	Density[a)]
			τ	ρ	τ	ρ	cm	µm	g cm^{-3}
Thermo Plus	tp	Black top	0.0012	0.046	0.054	0.05	70	65	0.93
		Transparent	0.886	0.094	0.66	0.045	90		
Black/White	wb	White	0.0012	0.637	0.065	0.04	140	100	0.98
Black/White	bw	Black	0.0012	0.048	0.063	0.043	140	100	0.98
Antidrop	ad	Transparent	0.91	0.083	0.82	0.056	160	35	-
Materbi	mb	Semi-transparent	0.315	0.052	0.29	0.033	140	20	1.25

[a)] as stated by the manufacturer

Polyethylene-based plastics exhibit mainly drop condensation behaviour. However, 'Antidrop' plastic is an exception and contains a special additive that causes almost perfect film condensation. Finally, 'Materbi' type plastic is a starch blend and is biodegradable.

The mean radiation properties at normal incidence were obtained by a common normalising procedure with given spectral data (*i.e.* transmission and reflection) using the Planck equation and assumed radiator temperatures of 5800 K and 293 K for the short-wave and long-wave radiation range, respectively. Different assumptions about the source temperature (-10 to 40°C) of the long-wave radiator (*e.g.* atmosphere, ground) had only minor effects on obtained long-wave transmissivities and reflectivities. Details on the procedures to obtain spectra for the reflection and transmission of plastic mulches can be found in HEIßNER *et al.* (2005).

In spring of 2001 and 2002, soil ridges were prepared which were typical for white asparagus spear production. Temperature sensors (PT 100 type, diameter: 5 mm) were

inserted horizontally at 5 different locations and measurements were taken hourly (DT 605, DATATAKER Corp., AU). Fig. 4.1 depicts the ridge dimensions and temperature sensor locations.

With the exception of the location of sensor II, for which 3 sensors were used in 2002, a single sensor was used to take measurements at each of the 5 locations. The overall experimental layout was such that two adjacent rows of ridges were serially covered with a 5 m long plastic mulch and one row to the south was established to diminish edge effects (*e.g.* missing shadow) (see Fig. 4.2). A control plot without any covering was also included in the experiment. The logging area was confined to the centre of each plot.

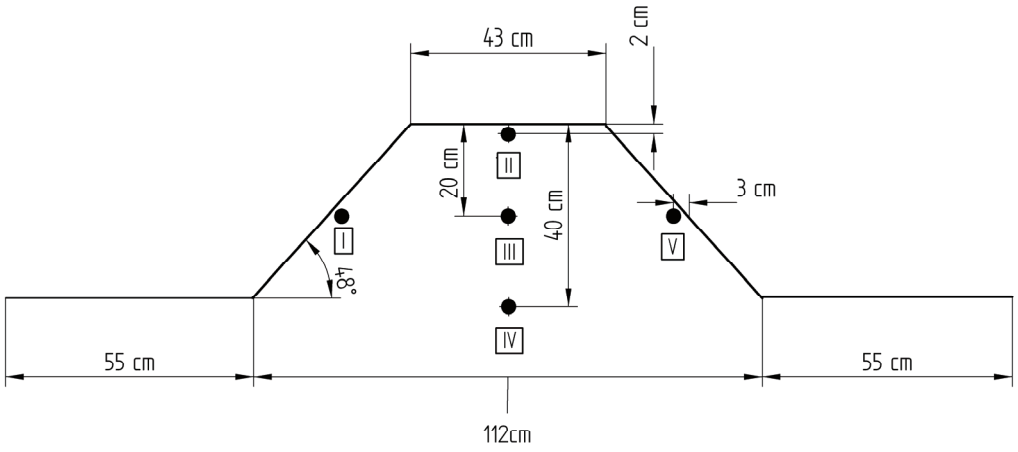

Fig. 4.1 Cross-sectional view of soil ridge dimensions and locations of the 5 temperature sensors (solid circles).

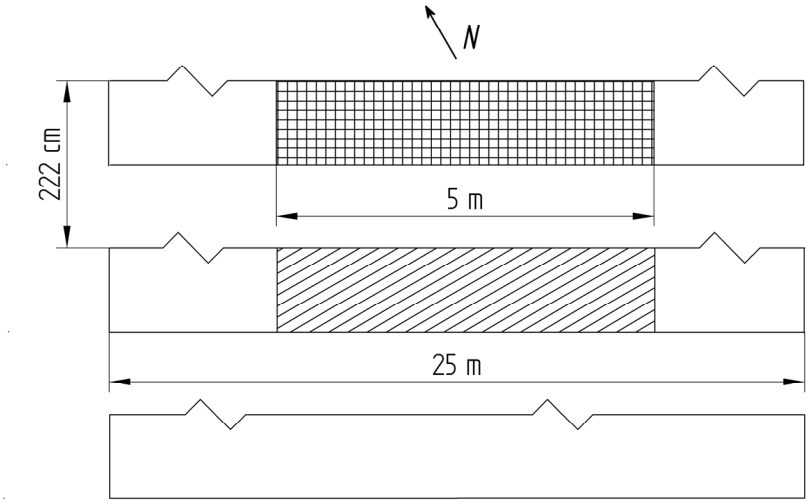

Fig. 4.2 Top view of soil ridges and imposed plots of plastic.

4.2.2 Experiment II - site Osnabrück

In 2003, measurements were taken on a farm located 18 km north of Osnabrück (Germany) and near the small river Mittelland-Kanal. This field site is characterised by a humus-rich sandy soil with contents of 3.96% humus, 89% sand and 2.5% clay. Hourly weather data were obtained from a weather station located at the University of Applied Sciences in Osnabrück and missing wind speed values have been drawn from a nearby station of the German Weather Service.

Overall, 19 north-south aligned ridges with a row distance of 1.80 m were prepared and covered with various plastic mulches. The same mulch types were used as in Experiment I (Table 4.1), but they differed in age as most had been already used for two years, except for the new 'Antidrop' plastic. Mulch application, *i.e.* initial placing, removing and turning, was not constant as different options were explored and the effect on soil temperature recorded. The corresponding dates of application changes are summarised in Table 4.2.

Table 4.2 Dates of treatment changes of plastic mulches in experiment II.

Plastic	Ridging and covering	Start of spear harvest	Cover off	Cover on	Cover off	End of recording
Thermo Plus	15.03.	12.04.	06.05.	23.05.	28.05.	10.06.
Black/White	15.03.	16.04.	-	-	-	10.06.
Antidrop	15.03.	10.04.	06.05.	-	-	10.06.
Bare	15.03.	22.04.	-	-	-	10.06.
			Turn to white	Turn to black	Turn to white	
White/Black	15.03.	19.04.	03.05.	23.05.	29.05.	10.06.

In contrast to experiment I, the ridges contained asparagus plants. Therefore, to harvest the spears, plastic mulch covers were removed for about 10 minutes each day. As harvesting through 'Antidrop' was done by piercing, the sheet was thereby damaged and removed on 6 May.

Temperature recordings were made at 2, 20 and 40 cm (positions II-IV in Fig. 4.1) below the ridge top at slightly off-centred positions with miniaturized temperature-data loggers (Thermofox Mini, Scanntronik, GER, sensor type: NTC 10kΩ, 3.5 x 3 x 2 mm width x height x length). Three mini-loggers were vertically fixed with wooden pieces within a closed plastic pipe (PVC, 40 cm length, 3.5 cm diameter) to ensure proper measurement levels and sealed with paper sheets to prevent substantial heat conduction between vertical levels. In some plots, water potential was measured twice at 40 cm depth with commercial used tensiometers.

4.2.3 Model calibration and parameterisation

The long-wave sky radiation ($R_{L,d}$) was not available for the time of our experiment, but using measurements of $R_{L,d}$ at the site in Grossbeeren for 2003 with a CG1 pyrgeometer

(Kipp & Zonen, NL), the scheme proposed by NIEMELÄ et al. (2001) was parameterised and used throughout the simulation:

$$R_{\mathrm{L,d}} = \left[1 + \left(\frac{\sigma T_{\mathrm{a}}^{4}}{R_{\mathrm{L,d,c}}} - 1\right) k_3 c^{k_4}\right] R_{\mathrm{L,d,c}} \qquad (4.1)$$

$$R_{\mathrm{L,d,c}} = (k_1 + k_2 e_a \exp(1500/T_a))\sigma T_{\mathrm{a}}^{4}$$

with cloud fraction c, air temperature at reference height T_{a} and clear sky radiation $R_{\mathrm{L,d,c}}$. The water vapour pressure at reference height e_{a} has units hPa. The cloud fraction c, treated as input by NIEMELÄ *et al.* (2001), was derived using an algorithm suggested by DONG *et al.* (1992).

$$c = \left(1.333 - 1.333\frac{R_{\mathrm{S}}}{R_{\mathrm{S,max}}}\right)^{0.294} \qquad (4.2)$$

where the maximum global radiation at the earth surface $R_{\mathrm{S,max}}$ was estimated as:

$$R_{\mathrm{S,max}} = (0.79 - 3.75/\beta) S_0 \qquad (4.3)$$

with solar elevation angle β in degrees and solar constant S_0. The cloud fraction was only estimated in hours when $\beta > 10°$ and was retained at that value during the following hours (*e.g.* during the night). The least-square estimated parameters (k_1 to k_4, Eqs (4.1)) were derived from fitting 3363 hourly day and night measurements of $R_{\mathrm{L,d}}$, e_{a}, T_{a} and R_{S} with a resulting *RMSE* of 18 W m^{-2}. Table 4.3 compares the estimated parameter values with the original values given by NIEMELÄ *et al.* (2001).

Table 4.3 Estimated parameters of the long-wave sky radiation submodel.

Parameter	Estimate	NIEMELÄ *et al.* (2001)
k_1	0.72	0.7
k_2	3.57	5.95
k_3	0.73	0.87
k_4	3.38	3.49

Measured dimensions of prepared ridges in experiments I and II were translated into a

finite element-type description as required by 2DSOIL. There are no decisive rules for the construction of grid meshes, except that surface-near elements, where fluxes are higher, should be small and neighbouring elements should not differ in size (area) by more than 50% (TIMLIN *et al.*, 1996). Care was taken to start with relatively thin elements at the soil surface (1.75 cm, Fig. 4.3). These elements were subsequently enlarged until the half depth of the ground water table (d_{gw}) was reached and then decreased until d_{gw} was approached. Below that depth, element size increased again towards the assumed depth of constant temperature (d_{ht} = 10 m).

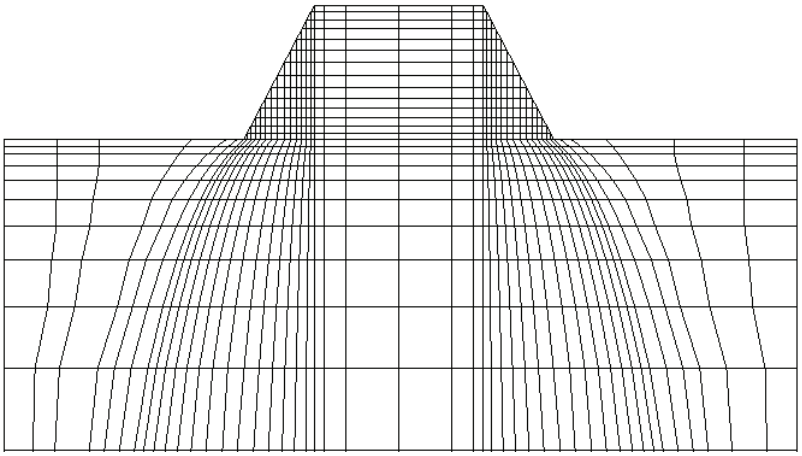

Fig. 4.3 Upper part of a finite element representation of a soil ridge as required by the 2DSOIL simulator. Each intersection of two lines represents one node.

The constructed grid was typically about 1500 nodes and 1500 elements and 45 upper and lower boundary nodes. Each plastic was applied symmetrically to the centre of the ridge tops and resulted in uncovered furrows dependent on the plastic's width. For each surface node, the local cover state was recorded as plastic type (two types for 'Thermo Plus') as well as uncovered or covered.

As the required aerodynamic parameters (zero plane displacement d and roughness length z_0) are rather influenced by non-ridged surroundings in experiments I and II, these parameters were set to general surface estimates using the relations: $d = 0.82h_c$ and $z_0 = 0.046h_c$ which were given by VERHOEF *et al.* (1997) with h_c (0.25 m) being the estimated mean height of roughness elements over the experimental field site during the

period of investigation. In other situations where the upwind fetch (~200 m for reference height of meteorological inputs of 2 m) is mainly influenced by soil ridges, the relations given by HAGEN and ARMBRUST (1992) or SALEH *et al.* (1997) should be used to infer values for d and z_0 from ridge height, spacing and wind direction.

Necessary parameters to solve the two-dimensional Richards equation of liquid water transport in 2DSOIL are the hydraulic conductivity function $k(h)$ and the water retention function $\theta(h)$. Here, use is made of the closed-form approximation from the 2DSOIL model with modified van Genuchten functions together with the pore size-distribution model of MUALEM (1976) (see TIMLIN *et al.,* 1996). Parameters required for the soil model (2DSOIL) are listed in Table 4.4.

For experiment I in 2002, in situ measurements of volumetric water content with a TDR sensor (Trime IT, IMKO, GER) and of soil water potential with a 1500 kPa range equitensiometer (Delta T devices, UK) at 10 cm depth have been used to calibrate the retention function. For experiment II, calibration was mainly based on the pedo-transfer relations given by VEREECKEN *et al*. (1989) which perform well compared to other proposed regression models (SCHAAP *et al*., 1998).

An important parameter for the partition between the various energy fluxes of uncovered ridges is h_{eq} (Eq. (3.27)). The estimated value of 1.3 for h_{eq} was an appropriate choice for the Grossbeeren site as evaluated on uncovered soil temperature simulations over the first month after ridging in 2002; this setting was also used for the other site. A similar value (h_{eq} = 1.0) was obtained by SCHELDE *et al.* (1998) for a quite different Scandinavian soil (clay: 8%; sand: 60%; organic carbon: 3%). The calibration period was restricted to the first month after ridging 2002 as there was no irrigation which might affect the predictions of soil temperature via advection of moist and cool air (see discussion below).

Table 4.4 Parameters required by the 2DSOIL model.

Parameter	Meaning	Unit	Input values	
			Expt I	Expt II
X_{sand}	sand content	%	91.3	89
X_{silt}	silt content	%	4.1	8.5
X_{clay}	clay content	%	4.6	2.5
X_{hu}	humus content	%	0.8	3.96
ρ_b	soil bulk density	g cm $^{-3}$	1.63[a)]	1.48[a)]
K_s	saturated hydraulic conductivity	cm d^{-1}	250[b)]	450[b)]
θ_s	saturated soil water content	cm^3 cm^{-3}	0.38[d)]	0.39[c)]
θ_r	residual soil water content	cm^3 cm^{-3}	0.03[d)]	0.055[c)]
α	parameter of van Genuchten retention function	cm^{-1}	0.0516[d)]	0.03[e)]
n	ditto	-	1.43[d)]	1.43[f)]

[a)] unpublished regression function of ρ_b on X_{hu} and X_{sand}
[b)] calculated after SAXTON *et al.* (1986)
[c)] calculated after pedo-transfer relations given by VEREECKEN *et.al.* (1989)
[d)] estimation from *in situ* measurements of θ and h in 2002 (TDR sensor: Trime IT, IMKO, GER; equitensiometer: Delta-T devices, UK, 1500 kpa range)
[e)] varied accordingly to increase in field capacity by 3 at volume basis
[f)] set to same value of the soil as in experiment I

From comparisons of simulated and measured soil temperatures of the Black/White plastics (either side) in experiment I (2001, 2002, one month), the optimal values of the mean effective air thickness between the soil and the plastic (d_{gap}) were estimated as 3 mm for horizontal nodes (criteria: minimum *RMSE* of the upper centred soil temperature, position II, see Fig. 4.1) and was increased by 30% for tilted nodes (criteria: minimum RMSE of the soil temperatures at the slopes, positions I and V). This compares well with d_{gap} = 3.6 which was adopted in a similar model by WU et al. (1996). In contrast, in the one-dimensional model of heat transfer of plastic mulches proposed by HAM and KLUITENBERG (1994), a mean air thickness of 0.65 mm was used. This large difference can be partly contributed to the neglected latent heat transfer from the soil to the plastic within their model which can be shown by the following ratio:

$$\frac{H+\lambda_w E}{H}=\frac{\rho_{air}C_{air}(T_s-T_m)/r_c+\rho_{air}C_{air}\Delta(T_s-T_m)/(yr_c)}{\rho_{air}C_{air}(T_s-T_m)/r_c}=1+\frac{\Delta}{y}=3.19 \quad (\text{for } 20°C)$$

This ratio represents the sensible (H) and latent ($\lambda_w E$) heat fluxes to sensible heat flux only. With r_c being the contact resistance as derived from d_{gap}. Therefore, a consistent re-estimate of d_{gap} from HAM and KLUITENBERG (1994) would be 0.65 × 3.19 = 2.07 mm, which is close to the value adopted here. However, note that this discussion is only valid in cases where the soil is warmer than the plastic and not too dry (relative humidity of soil surface layer air - rh_s ~ 100%) or when the lower side of the plastic is wetted and warmer than the soil. It is very likely that the d_{gap} value will depend on soil surface roughness and slope. Hence, some variation of d_{gap} between different studies is to be expected.

Using the same procedure to estimate the common exchange height (z_{ce}), produced an estimate of 0.5 m. However, simulated temperatures were insensitive to this parameter setting, *i.e.* overall *RMSE* were 1.22 and 1.26 for z_{ce} values of 0.5 and 1.5 m, respectively.

In Chapter 3 equations are presented to describe the directional responses of short- and long-wave transmissivities and reflectivities. For the 'Antidrop' and 'Materbi' plastics, measurements of short-wave directional transmissivity $\tau_b(\delta)$ (HEIßNER *et al.,* 2005, POLLET & PIETERS, 2000) were well reproduced by the proposed Fresnel theory based approach depicted in Fig. 4.4.

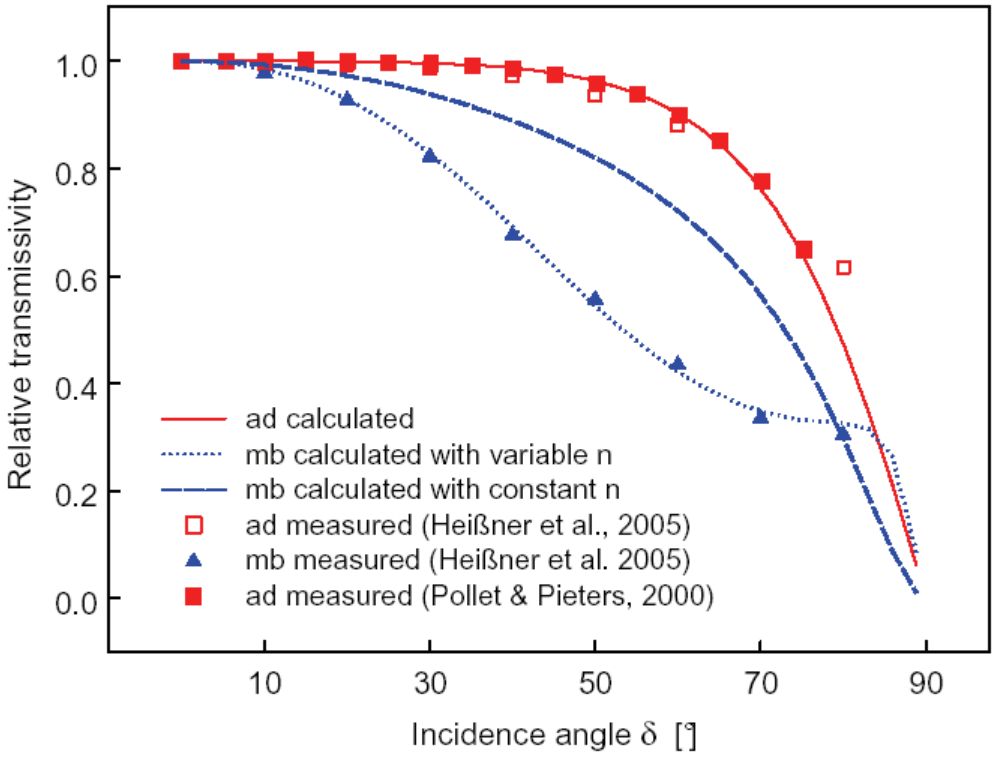

Fig. 4.4 Comparison of measured and simulated directional short-wave transmissivity for the 'Antidrop' (ad) and 'Materbi' (mb) plastics with constant or variable adopted *n* for the latter. All necessary inputs are listed in Table 4.1.

Using the measured transmissivities and reflectivities at normal incidence, predictions corresponded well with the estimated transmissivities at different incidence angles. However, for the 'Materbi' plastic, the empirical inclusion of an angle-dependent complex refraction index was necessary to fit data well and has been also applied to the long-wave range (with δ in rad).

$$n^*(\delta) = n\,(1 + 1.567\delta^{2.49}) \tag{4.4}$$

We then questioned whether the full Fresnel theory is required and even whether simpler approaches, such as the Schlick equation, are sufficient or indeed even more appropriate. Having no extensive measurements of directional response on plastic mulches available, recorded uppermost soil temperatures beneath plastic mulches (positions I, II, IV) over the first month after ridging in 2001 and 2002 in experiment I

were used as evaluation criteria for the different modelling options for directional radiative behaviour of plastics. The obtained *RMSEs* for various plastics are summarised in Table 4.5.

Table 4.5 Comparison of *RMSE* between simulated and measured soil temperatures (K) at uppermost depths (2-3 cm from soil surface). First month after ridging, experiment I, 2001 and 2002.

Label	Fresnel theory	Schlick theory	no directional response
tp	1.61	1.57	1.71
wb	1.14	0.88	0.87
bw	1.50	1.52	1.56
ad	1.99	1.98	2.91
mb	1.62	2.54	2.53
mean	1.57	1.70	1.92

For semi-transparent and transparent plastic mulches, it seems to be essential to include the directional radiative response (see Table 4.5), while the much simpler Schlick equation and its extensions gave similar predictive results for soil temperature, except for the 'Materbi' where transmission displays an unusual directional response (Fig. 4.4). As the Schlick equation performed better for the 'White/Black' plastic, this model was preferred for simulations of this plastic throughout this work.

4.2.4 Simulation procedure

The mean seasonal depth of ground water table is known to be at about 2 m for both sites. Therefore, it would be an option to use a constant saturated water content or zero water potential gradient as the lower boundary condition at the depth of ground water table. Here, more flexibility was introduced by adopting a time-dependent flux boundary condition according to the approach of HOPMANS and STRICKER (1989). This condition was parameterised using water table measurements and one-dimensional test simulations made from 1997-2000 using the estimated h_{eq} value defined for the site Grossbeeren. The ground water recharge rate Q (cm d^{-1}) was calculated as follows:

$$Q = -0.2 \exp(-0.0365 \,|\, h(d_{gw}) - 100 \,|) \qquad (4.5)$$

with soil water potential h at lower boundary depth (d_{gw} =2.5 m). Equation (4.5) was also used for the Osnabrück site. The lower boundary for heat transfer was set to 10°C at 10 m depth for both sites which represents the mean estimated air temperature over the years 2001 and 2002.

All simulations were initiated on 1 January each year with constant values for the soil water potential (10 hPa) and temperature (10 °C) at all depths. Computations were started with an one-dimensional bare soil column until the date of ridging and covering was reached. After that date, simulations proceeded using the two-dimensional ridge and covering description where initial profiles of temperatures and water potentials were derived from the previously simulated one-dimensional soil column because spatial density of sensor locations was insufficient.

As the computation of soil heat and water transfer of various neighbouring ridges is very resource demanding, only one ridge including the half width of the furrow at each side was considered for belowground calculations. However, diffuse and direct radiation shadows from neighbouring ridges were accounted for according to the actual position of each node and plastic. The maximum allowable time step was set to 10 minutes, while in reality, the time step was always lower. This was controlled internally by the synchroniser module of 2DSOIL (TIMLIN *et al.*, 1996).

Simulations proceeded for 3 months from the date of ridging and covering in experiment I (2001: DOY 134; 2002: DOY 82) and for varying amounts of time for experiment II as stated in Table 4.2. Hourly output values of simulated soil temperature and water potentials at sensor locations within the ridge were determined after six days following ridging by a bi-linear interpolation routine (PRESS *et al.*, 1994) with four adjacent nodal values as input.

4.3 Results and Discussion

4.3.1 Model validation

After implementation of all parameterisations outlined in the preceding subsection, the overall model performance to predict temperatures was evaluated over the first three months of covering in experiment I. The obtained *RMSE* ranged from 0.5 - 2.4 K depending on plastic type and sensor position (Table 4.6). Biases of mean soil temperatures varied between 1.1 K underprediction and 2.2 K overprediction (*MBE*, Table 4.6). The ranking of the investigated coverings in terms of the overall mean temperature of sensors locations II-IV was the same in predictions and measurements (results not shown).

Table 4.6 Model performance statistics of hourly temperature simulations over 3 months for experiment I (mean of 2001 & 2002). Sensor positions: I: south slope, 3 cm; II: central, 3 cm; III: central, 20 cm; IV: central, 40 cm; V: north slope, 3 cm. br = bare ridge (see Fig. 4.1).

Label	*RMSE*					*MBE*				
	I	II	III	IV	V	I	II	III	IV	V
tp	2.4	1.3	1.2	0.9	1.6	-0.2	-0.3	0.3	0.5	-0.4
wb	1.0	1.0	0.6	0.5	1.0	0.1	0.3	0.0	-0.2	-0.1
bw	1.7	1.4	1.4	1.3	2.6	0.8	0.7	1.1	1.1	2.2
ad	1.6	2.2	1.2	1.2	2.7	0.5	-1.1	0.2	0.9	1.1
mb	2.2	2.3	1.7	1.4	2.0	1.4	1.5	1.3	1.2	1.1
br	1.8	1.7	1.0	0.6	1.9	-0.2	0.6	0.4	0.1	-0.1
mean [a)]	1.8	1.7	1.2	1.0	2.0	0.4	0.3	0.5	0.6	0.6
mean [b)]			1.5					0.5		

[a)] per position
[b)] over all positions

Predicted and observed soil temperatures are presented for daily averages of central located sensor positions (II-IV) for the whole simulation periods in 2001 and 2002 (Fig. 4.5 & 4.6) with declining heating effects from the top to the bottom graphs. In general, measured temperatures are matched well with a slight tendency to overestimate mean soil temperatures under ridges covered with the ‘Materbi’ and the ‘Black/White’ plastics.

The slight mean overprediction of 0.5 K (*MBE*) for both years may be contributed to possible advection of relatively cool air from the surrounding experimental field site where mostly irrigated vegetables were grown. Looking at estimates of *MBE* at the deeper depths (positions III, IV, see Fig. 4.1 & Table 4.6), which are anticipated to be more precise and represent the overall system state as measurements are to a lesser extent affected by surface variations and diurnal oscillations it can be observed, that treatments causing less heating, such as the uncovered ridge or the 'White/Black' plastic show only a minor bias in temperature predictions; this observation supports the advection hypothesis.

Further comparisons were performed for experiment II. A slightly increased mean *RMSE* of 2 K when compared to all positions was found (Table 4.7). These larger deviations can be partly contributed to the usage of an offsite weather station and to less available information on the particular soil. Moreover, data were collected during the harvest season, and mostly three year old plastics were used. This introduces uncertainties about the actual radiation properties of the used plastics (AVISSAR *et al*., 1986a, 1986b) as well as daily disturbances of energy and mass transfer. There was a large underprediction for uncovered ridges (see Table 4.7) which also influenced the performance statistics of the temporarily uncovered 'Antidrop' and 'Thermo Plus' treatments (see Table 4.2).

Table 4.7 Model performance statistics of hourly temperature simulations in experiment II (2003). Sensor positions and depths: II: central, 2 cm; III: central, 20 cm; IV: central, 40 cm depth. br = bare ridge.

Label	*RMSE*			*MBE*		
	II	III	IV	II	III	IV
tp	3.2	2.0	1.5	-2.3	-1.1	-0.6
wb	1.9	1.3	1.4	-0.9	0.0	-0.4
bw	2.0	1.1	0.7	-0.6	-0.3	0.2
ad	3.6	2.4	1.7	0.2	-0.6	-0.4
br	3.2	2.0	1.7	-0.9	-1.7	-1.5
mean[a)]	2.8	1.8	1.4	-0.9	-0.7	-0.6
mean[b)]		2.0			-0.7	

[a)] per position
[b)] over all positions

Considering the biases in Table 4.7, the mean soil temperature of the uncovered soil was clearly critically underpredicted. Calculated soil albedos could be a possible source of error. Therefore, model calculations of dry and wet soil albedos were checked against a data set that measured short-wave soil albedos over a range of soil humus contents and textures (POST *et al*., 2000). Non-linear regression fits of their dry and wet albedos versus soil humus content were used to obtain independent estimates for the two soils used here (Table 4.8). As the calculated soil albedos from different sources correspond quite well, uncertainties that the submodel for soil albedo could cause biases of temperatures taken in uncovered soil were disregarded.

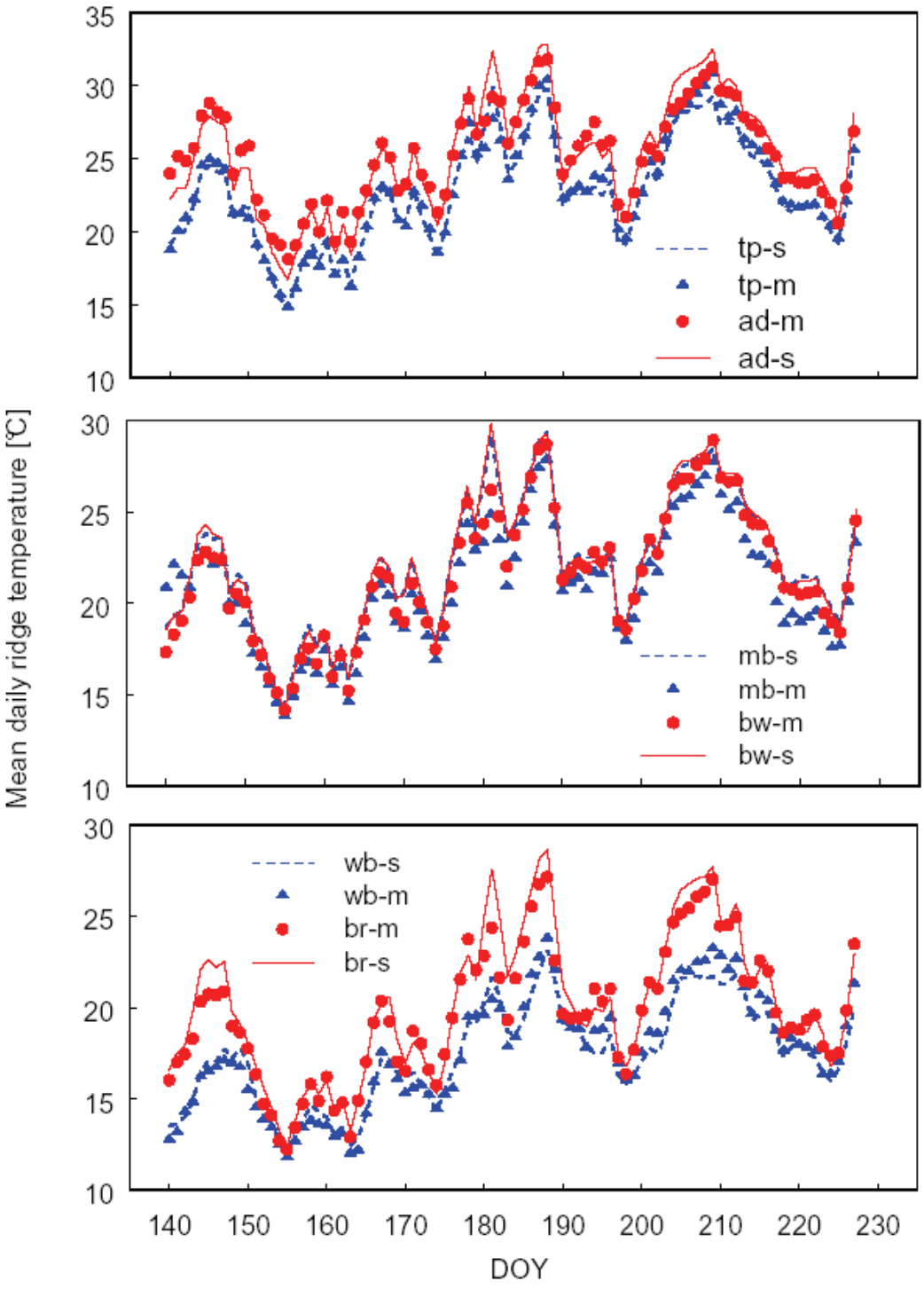

Fig. 4.5 Measured and simulated mean daily ridge temperatures in experiment I (2001) versus day of year (DOY). Symbol output is each second day. Labels: tp-s/ tp-m: Thermo plus simulated/measured; ad-s/m: 'Antidrop' simulated/measured; mb-s/m: 'Materbi' simulated/measured; bw-s/m: 'Black/White' simulated/measured; wb-s/m: 'White/Black' simulated/measured; br-s/m: bare simulated/measured. Means were obtained from sensor locations II, III and IV.

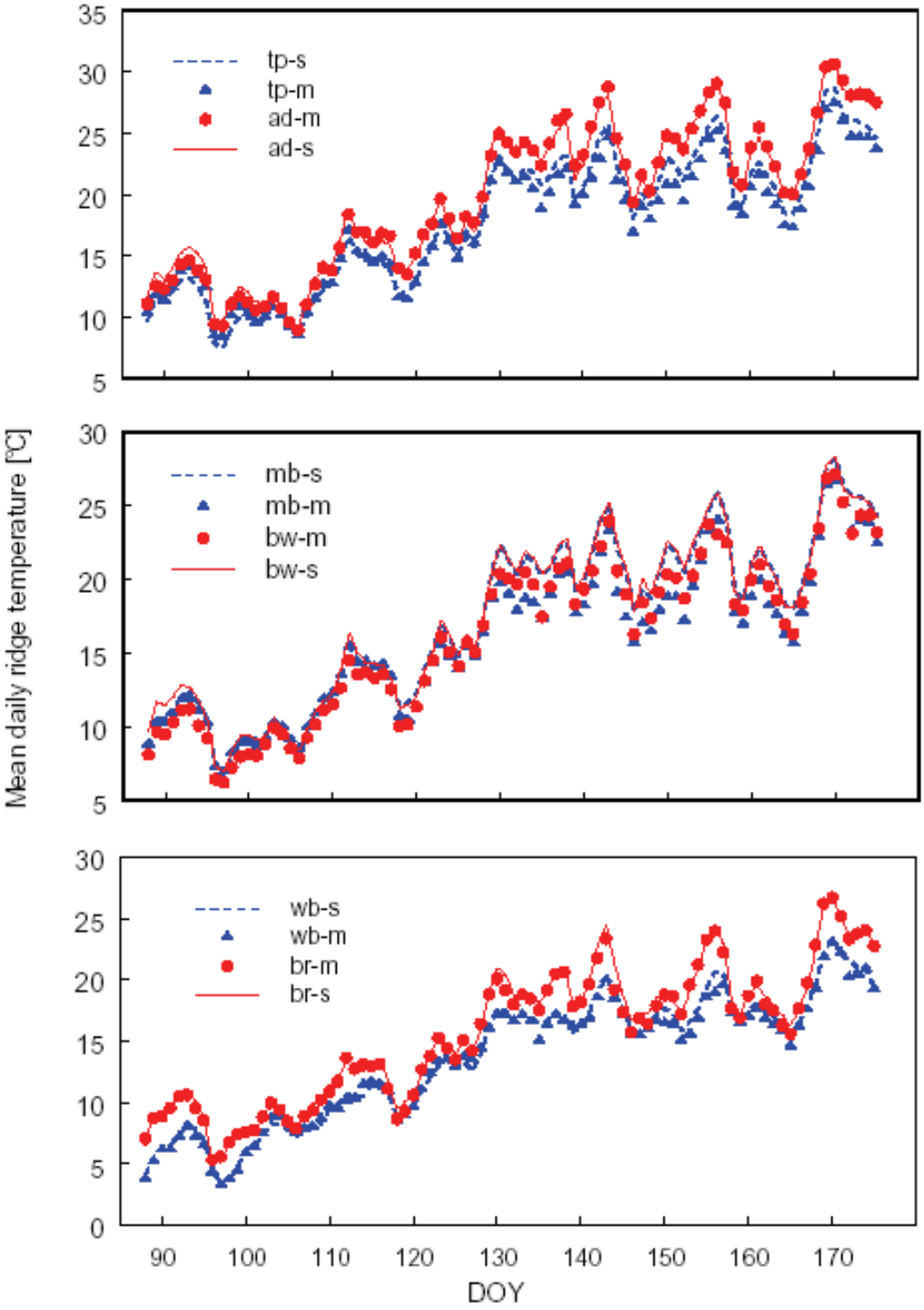

Fig. 4.6 Measured and simulated mean daily ridge temperatures in experiment I (2002) versus day of year (DOY). Treatment labelling and mean calculations are as in Figure 4.5.

Table 4.8 Calculated dry and wet albedos ($\rho_{s,dry}$ - Eq. (3.10) and $\rho_{s,wet}$ - Eq. (3.11)) for two sandy soils with substantial difference in humus contents. First values are calculated. Second values are from non-linear regressions fits to data given by POST *et al.* (2000).

Site	Humus content [%]	$\rho_{s,dry}$		$\rho_{s,wet}$	
Grossbeeren	0.8	0.30	0.279	0.196	0.165
Osnabrück	3.96	0.121	0.136	0.073	0.061

Next, sensitivity of bias versus the adopted value of the saturated hydraulic conductivity (K_s) was assessed. This precaution is warranted as estimated K_s from pedo-transfer function predictions should be treated as a random variable having a lognormal distribution (TIETJE & HENNINGS, 1996). Moreover, daily harvesting is likely to decrease the K_s of furrows. Another point of concern is the known poor performance of predicting unsaturated hydraulic conductivity with the Mualem-van Genuchten model using K_s directly (SCHAAP & LEIJ, 2000). SCHAAP and LEIJ (2000) concluded from their analysis of the Unsoda data set, that instead of K_s, a modified value K_o should be used to infer unsaturated hydraulic of soils, where K_o is one order of magnitude smaller than K_s. In fact, the 2DSOIL model provides the framework to use such an approach to account for this deficiency using the parameters K_k and θ_k; however, as there is no information on how to estimate θ_k (SCHAAP & LEIJ, 2000), this modelling device has not yet been used. Setting K_s to 100 cm d^{-1} and repeating simulations for experiment II resulted in a reduction of *RMSE* and *MBE*. As the ridged surface in experiment II was about 34 m x 100 m and covered with mostly soil heat promoting plastics, a smaller advection effect would be expected compared to experiment I. Taken together, the calculated overall bias of –0.1 K (see Table 4.9) would therefore seem quite reasonable.

Table 4.9 Model performance statistics of hourly temperature simulations in experiment II (2003) with reduced saturated hydraulic conductivity (K_s =100 cm d^{-1}). Sensor positions and depths: II: central, 2 cm; III: central, 20 cm; IV: central, 40 cm depth. br = bare ridge.

Label	*RMSE*			*MBE*		
	II	III	IV	II	III	IV
tp	3.1	1.7	1.2	-1.7	-0.5	-0.2
wb	1.9	1.4	1.4	-0.9	0.1	-0.3
bw	2.0	1.1	1.1	-0.5	0.1	0.7
ad	3.9	2.6	2.0	1.2	0.6	0.9
br	3.5	1.6	0.9	0.4	-0.4	-0.5
mean[a)]	2.9	1.7	1.3	-0.3	0.0	0.1
mean[b)]		1.9			-0.1	

[a)] per position
[b)] over all positions

The underprediction of soil temperatures by the partly transparent 'Thermo Plus' plastic was unexpected as one would empirically assume a loss of transmissivity of plastics with time. However, AVISSAR *et al.* (1986a, 1986b) reported larger soil heating beneath field-aged transparent polyethylene plastics compared to new plastics. They showed that this was due to modified transmission and reflection behaviour of wetted and dusty old plastics compared to wetted new clean plastics.

Mean daily ridge temperatures were well reproduced by simulations (see Fig. 4.7). From the start of spear harvest on day 100, the 'Antidrop' plastic was damaged due to piercing, and thereby its heating effect was severely diminished. By day 126, this plastic was completely destroyed and therefore removed, so data were then regarded as for an uncovered treatment. After the plastic's removal, simulations and observations compared better again for 'Antidrop' treatment. There is a clear tendency for underestimation of observed mean ridge temperatures for the 'White/Black' plastic in cases when the white side was on top (Fig. 4.7). This phenomenon is contributed to the possible advection of warm air from neighbouring ridges.

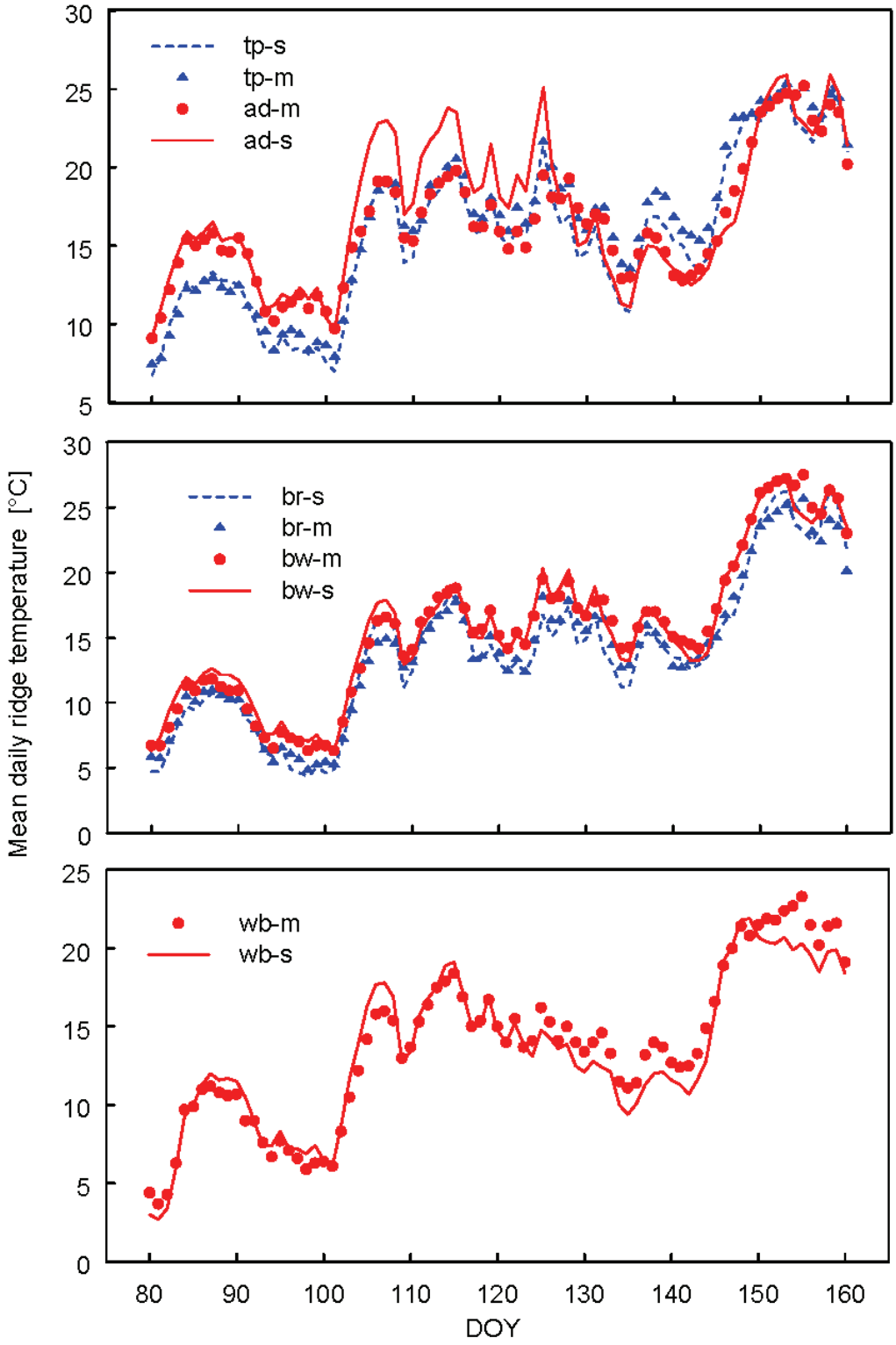

Fig. 4.7 Measured and simulated mean daily ridge temperatures in experiment II (2003) versus day of year (DOY). Treatment labelling and mean calculations are as in Fig. 4.5.

Over 10 days for a one-dimensional uncovered soil, *RMSE* values of 0.97 K and 0.42 K at simulated depths of 2.5 cm and 20 cm, respectively, were obtained (SCHELDE *et al*., 1998). This error level is lower than the observed *RMSEs* for experiment I and II here. However, after considering the increased complexity of the simulated problem (two-dimensional, plastic covers), the considerably longer evaluation period, the uncertainties due to advection effects as well as the offsite weather station used in experiment II, the obtained model errors here seem to be acceptable. Likewise, error levels are scale dependent, so normalising the estimated *RMSE* in experiment I with the corresponding observed mean yields relative *RMSEs* of 8.6% and 6.3% for the central located positions at 2 cm and 20 cm depth, respectively. These figures compare well with relative errors of 10% and 4% for similar locations reported by SCHELDE *et al.* (1998).

4.3.2 Comparing different spatial locations

In addition to hourly performance statistics for the various locations, some arbitrary time series of near-surface located positions for both simulated and measured diurnal courses of soil temperature during experiment I in 2001 are provided in Fig. 4.8. As anticipated for an almost east-west running ridge, the north sloped starts first to warm up during the morning hours and is followed by the ridge top. At about noon, the south slope is heated most effectively.

There is a slight tendency towards more rapid soil heating of model simulations compared to observations (see 4.8). We frequently observed that – compared to measurements- the north slope was heated faster in the morning hours, but also cooled faster in the afternoon. Therefore, this tendency could partly be related to the missing water vapour transfer mechanism in 2DSOIL which neglects water transfer to upper dry soil layers during the night due to water vapour exchange. Additionally, there are uncertainties regarding the diurnal behaviour of the used empirical modification of soil upper layer relative humidity prediction (h_{eq}). An underestimation of the latent heat flux of uncovered soil nodes will consequently lead to an overestimation of other heat fluxes including the soil heat flux. This reasoning is consistent with observations of YAMANAKA and YONETANI (1999) who reported that even a rather dry sand will

evaporate at its potential rate during the morning hours.

Whereas setting h_{eq} to 0 will lead to a slightly improved prediction of the uncovered treatment, there is no obvious reason to suggest that the foregoing discussion also holds for covered treatments. This is because for horizontal nodes, only water recycling between the soil surface and the lower plastic side is simulated.

Therefore, we further checked whether large gradients of near soil surface temperatures may lead to small scale advection effects of sensible heat from warm to cold surfaces nodes. Note that all aboveground heat fluxes are treated as one-dimensional fluxes by the proposed model as a two-dimensional implementation of the advection-diffusion equation for aboveground heat fluxes would be prohibitively complex. Indeed, a linear regression analysis of near surface bias dependence on the simulated gradient between the centre and south position revealed significant relations for both covered and uncovered treatments (Fig. 4.9). A difference in predicted temperature for the nodes at positions I and II was related to a bias of their prediction.

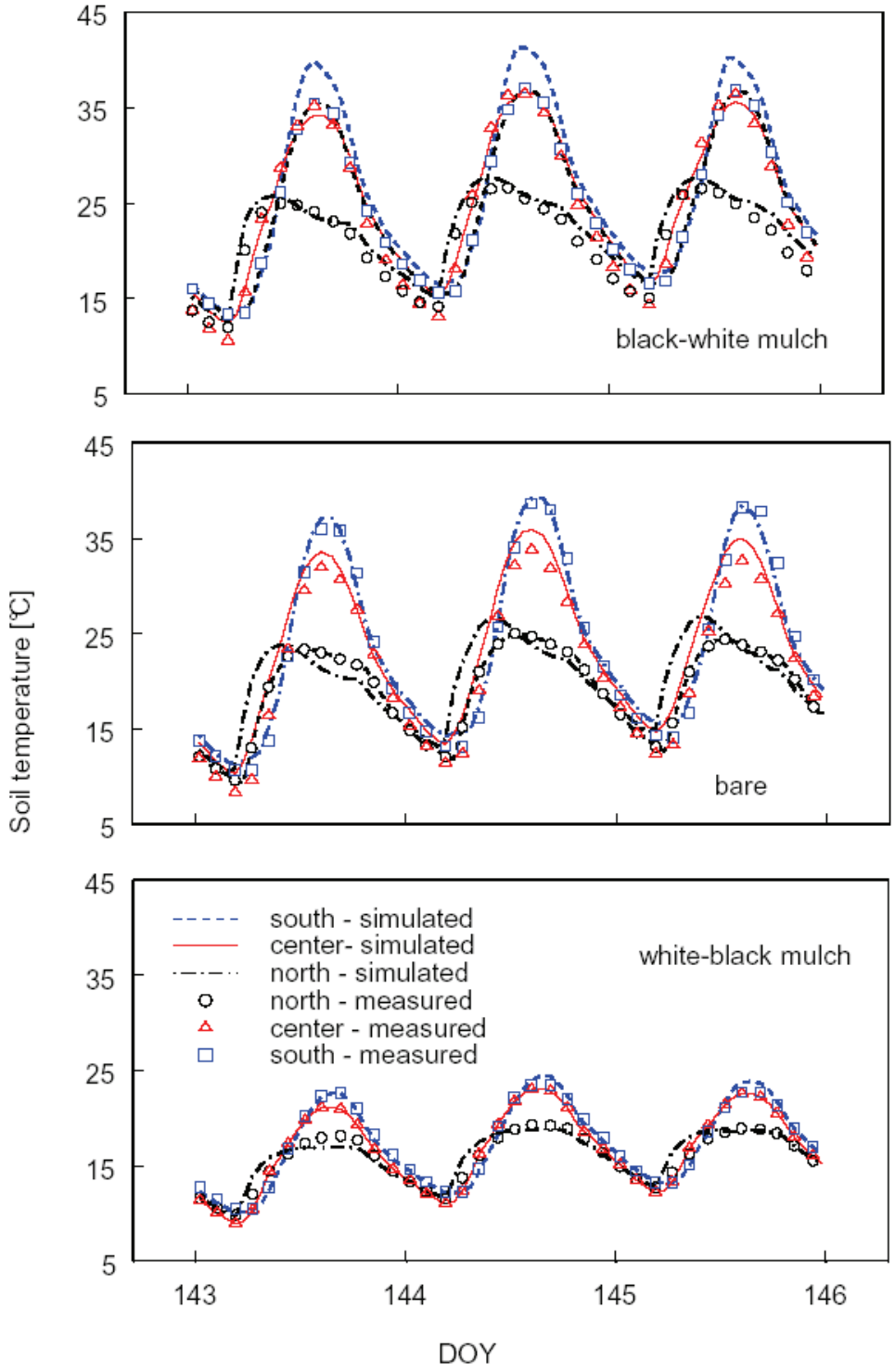

Fig. 4.8 Diurnal courses of hourly simulated and measured soil temperatures for different ridge positions and plastic coverings of an almost east-west aligned ridge (experiment I, 2001). bw: 'Black/White' plastic; br: bare, uncovered; wb: 'White/Black' plastic; North, South, Centre: near surface sensors at the north (V), south slope (I) and centre at 2 cm depth (II) and indicated in Fig. 4.1

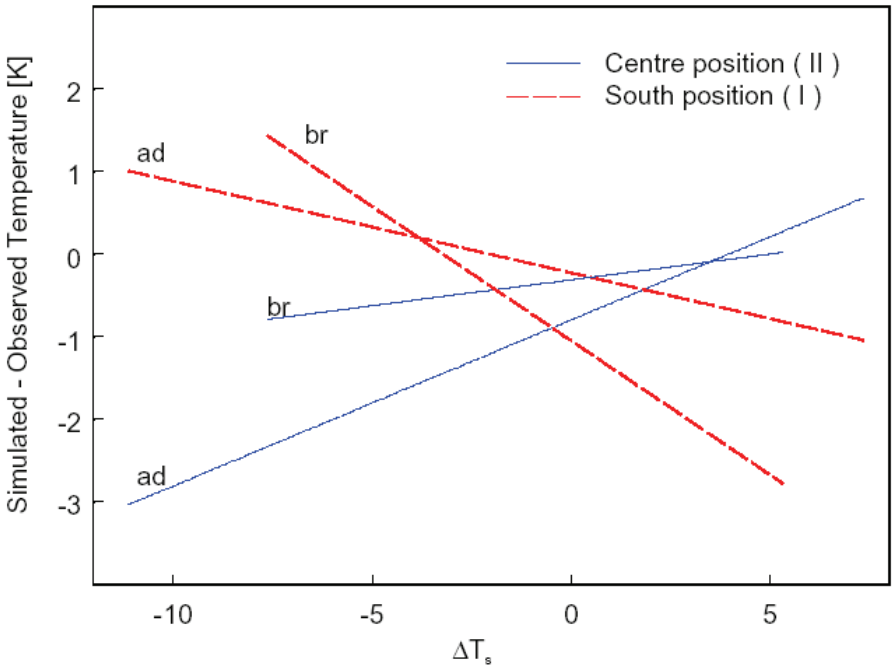

Fig. 4.9 Linear regression fits of the conditional bias of soil surface temperature on the simulated difference between the centre and south position (ΔT_s). Data are from experiment I (2002, daytime hours: 9–16, n = 792). Treatments: ad: 'Antidrop'; br: bare.

As this reasoning is supported by highly significant regression fits (for all models: $p <$ 0.01), this offers strong support for the advection hypothesis. For example, if the south slope is 5 K warmer than the ridge top (in predictions), then nodal temperatures of the ridge top were underestimated by about 0.7-1.8 K depending on the treatment. From the occurrence of advection effects in both covered and uncovered treatments, lateral heat transfer can be concluded to be mostly confined to the air space above the ridge surface. This was anticipated regarding the small cross-sectional area for lateral heat fluxes between the plastic and soil as given by d_{gap}.

An interesting phenomenon, which is reproduced at least partly by simulated results, is the occurrence of the night-time minimum at the central location. This behaviour results mostly from the ridge tops and slopes exposure to varying fractions of the sky. For example, on clear nights, ridge tops receive exclusively reduced long-wave radiation from the sky, whereas slopes are shielded to some portions of the sky and receive

usually higher long-wave radiation intensities from neighbouring warmer soil surfaces. This phenomenon was taken into accounted by the sky view factor parameterisation in our proposed model (F_d).

4.3.3 Transient heating behaviour of a managed white/black plastic mulch

As plastic mulch handling is time-dependent during experiment II (see Table 4.2), this aspect was studied in more detail for the 'White/Black' managed plastic. This plastic allows a certain level of control of soil temperatures. By reversing the side of the plastic exposed, a fast adaptation of the mean ridge temperature within about 1-5 days was simulated.

The measured transient behaviour was very similar to the simulations. However, the 'control space' was sometimes reduced when the white side was facing upwards (see Fig. 4.10 lower graph).

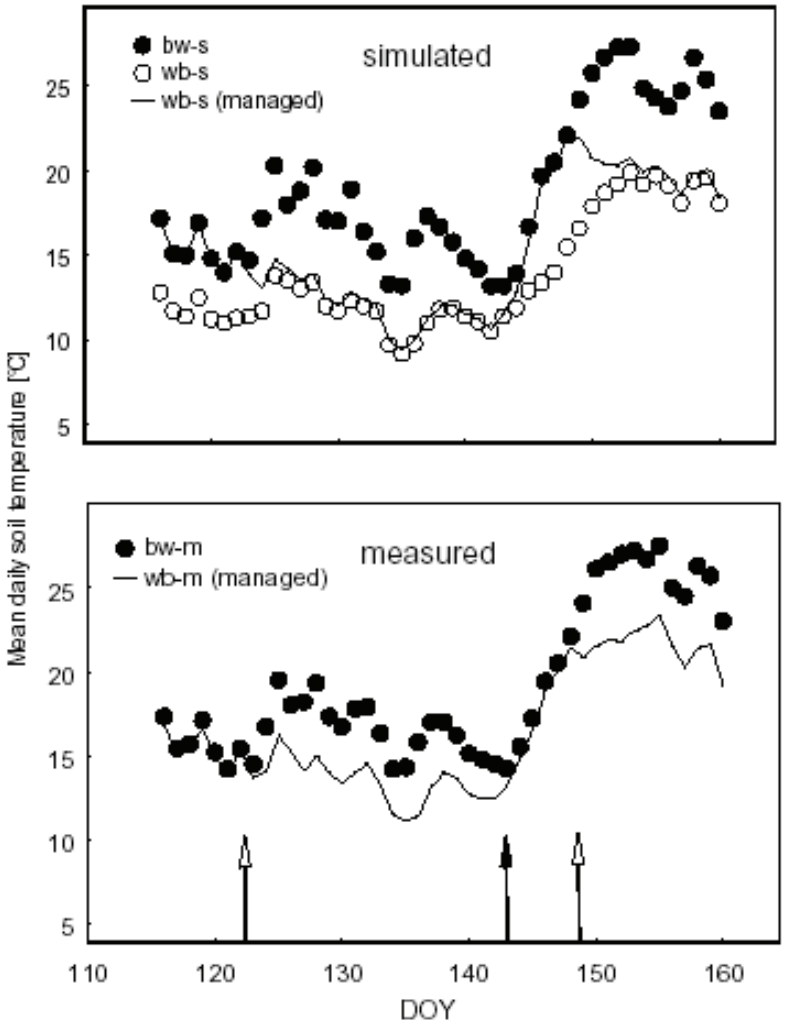

Fig. 4.10 Simulated (top) and measured (bottom) mean daily ridge temperatures for various handlings of the Black/White plastic mulch. Open and closed arrows on specific DOYs indicate a change of the top side to white and black, respectively. Treatments: bw-s/m: 'Black/White' measured/simulated throughout; wb-s: 'White/Black' covering throughout, simulated; wb-s/m (managed): 'White/Black' covering with changed upper sides, simulated/measured.

4.3.4 Simulated soil water dynamics

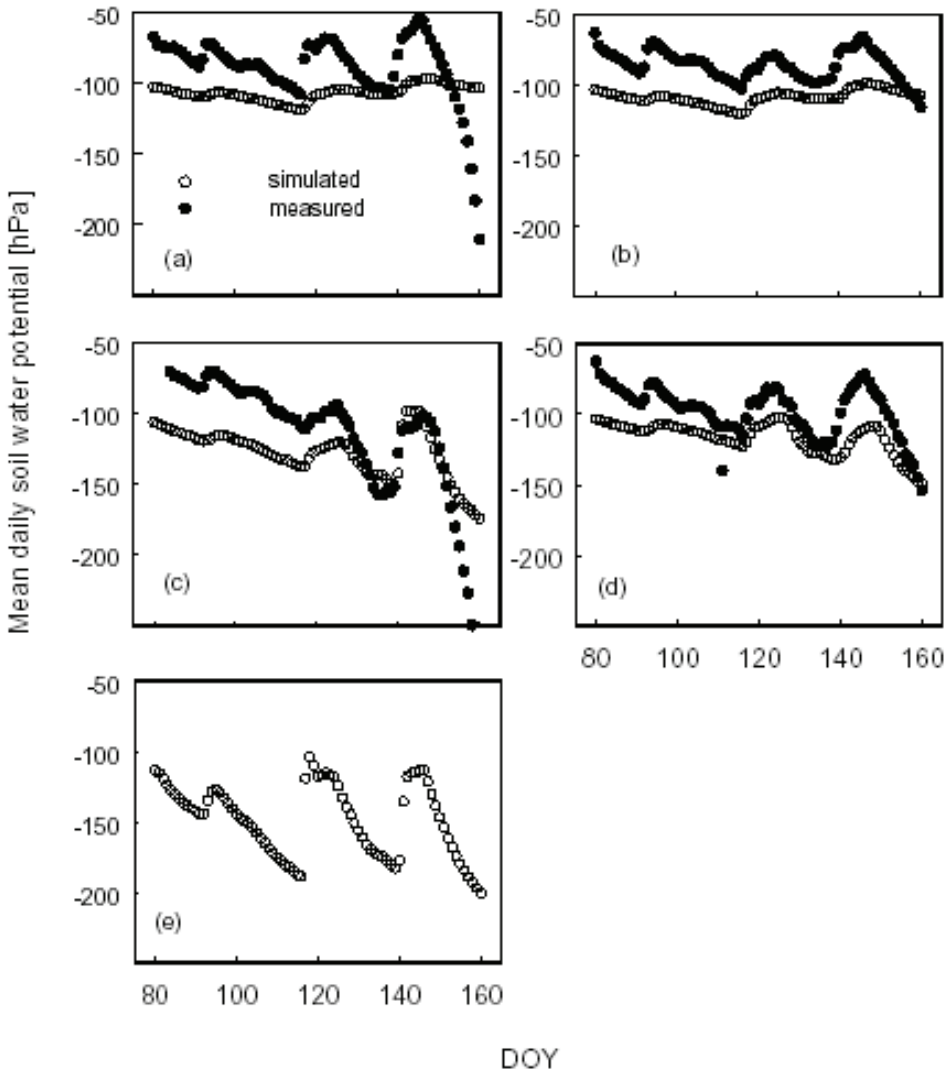

Fig. 4.11 Simulated and measured mean daily soil water potentials [hPa] at 40 cm depth below ridge top with day of year (DOY); (a) wb-ma; (b) bw; (c) ad; (d) tp; (e) uncovered.

Simulation of water dynamics was not the main objective of this investigation; however, the overall precision of temperature prediction is of course related to reliable volumetric water content simulations due to the dependency of volumetric heat capacity and thermal conductivity on volumetric water content. Simulations and measurements of soil water potential in experiment II are provided in Fig. 4.11 for all simulated

treatments.

Major trends of soil water potential at a 40 cm depth were well reproduced by the simulation model (Fig. 4.11). Regarding the temporal trends of drying and rewetting, the model tends to respond less sensitively when simulated water potentials are compared to actual measurements. To some extent, this could be related to uncertainties regarding the water retention characteristic of the soil in experiment II. This characteristic was approximated from the obtained soil parameterisation of experiment I with increasing the field capacity by 3% (volumetric content) at 180 hPa.

As expected, plastic coverage tends to conserve soil water (MAHRER *et al.*, 1984; NAOT *et al.*, 1987) although to what extent this is plastic dependent is not clear. Clear plastics with mostly film condensation (*e.g.* 'Antidrop' plastic) mode tend to decrease water conservation ability. This is probably due to pronounced evaporation during the day and more efficient water drainage at the lower plastic side on ridged slopes. Therefore, the most effective plastics were opaque with a drop-wise condensation mode (*e.g.* 'Black/White' plastic). These plastics prevent soil evaporation fluxes of covered nodes in periods of positive heat fluxes and reduce plastic water drainage at slopes after reaching the saturation limit.

4.3.5 Derived refraction indices for plastics

Using the measured and weighted transmissivities and reflectivities at normal incidence (see Table 4.1), an inversion approach from the Fresnel theory as well as taking the interfacial reflections and internal transmission into consideration (see Section 3.3.2), the complex refraction index of plastics have been calculated. The high reflecting 'White/Black' plastic has as would be expected a high real refraction index of 8.89 in the short-wave range; whereas the highly transmitting plastics ('Antidrop', 'Thermo Plus' at transparent sides) are characterised by refractions indices with a much lower imaginary part in both the short- and long-wave range.

Table 4.10 Real (n_r) and imaginary part (n_{im}) of the complex refraction index as derived from normal incidence transmissivities and reflectivities.

Plastic		Short-wave range $\lambda = 0.7$ µm		Long-wave range $\lambda = 10$ µm	
		n_r	n_{im}	n_r	n_{im}
Thermo Plus	black	1.56	5.70E-3	1.57	3.44E-2
	transparent	1.58	1.13E-5	1.42	2.81E-3
White/Black		8.89	2.60E-3	1.50	2.11E-2
Black/White		1.56	3.70E-3	1.52	2.12E-2
Antidrop		1.53	7.38E-6	1.44	2.64E-3
Materbi		1.55	2.95E-3	1.41	4.68E-2

The estimated refractive indices in the short-wave range for the transparent plastics ('Antidrop' and 'Materbi') compare well with values stated by PIETERS (1995) for polyethylene plastics (n_r = 1.515, n_{im} = 4.2E-6). COELHO *et al.* (2004) estimated refractive indices of various plastics with a similar inversion procedure for low and high density polyethylene (LDPE, HDPE) plastics for a wave length of 10.6 µm. A comparison of inverted refraction indices of the 'Black/White' and 'Antidrop' plastics, which belongs presumably to the HDPE group, revealed that the real values of the refraction index are very similar, but imaginary parts seem to be highly variable depending on the specific production process of plastic. Values are provided in Table 4.11.

Table 4.11 Estimates of the complex refraction index for different plastics from inversion modelling using transmissivities and reflectivities at a wave length of 10.6 µm. n_r: real part of refractive index; n_{im}: imaginary part of refractive index.

Plastic	Appearance	n_r	n_{im}	Density [g cm^{-3}]
LDPE	Transparent	1.58	9.0E-4	0.91-0.94[a)]
HDPE	Transparent	1.50	7.0E-4	0.95-0.97[a)]
HDPE	White	1.50	1.0E-3	0.95-0.97[a)]
Antidrop[b)]	Transparent	1.51	1.2E-3	not available
White/Black[c)]	White	1.51	3.4E-2	0.98

[a)] typical range, COELHO *et al.* (2004)
[b)] τ = 86.9%, ρ = 7.56% at λ=10.6 µm
[c)] τ = 1.62%, ρ = 4.16% at λ=10.6 µm

4.4 Conclusions

This study investigated the modelling of the energy balance and heating behaviour of soil ridges partly covered with plastic mulch. The proposed model was found to be valid from comparisons of simulated and observed soil temperatures at different depths and positions along the ridged surface over several months of recording. Moreover, the general trends of soil moisture dynamics were also simulated well.

To avoid repeating previous research, our study was based on a well-tested two-dimensional soil model 2DSOIL. This allowed us to simulate belowground heat and water transfer which was interfaced with a detailed model of the energy balance of surface nodes. In contrast to the complexity of the previously proposed model, our model only demands a view inputs: (1) basic soil information such as humus content, texture and saturated conductivity, (2) the shape and dimensions of the ridge and plastic mulch cover, and (3) the transmissivities and reflectivities of the used plastic mulches. Further parameterisations like estimations of soil water retention characteristics or soil quartz content are also likely to improve temperature predictions.

From test simulations, it is clear that a very detailed treatment of directional radiative properties of opaque plastics is unnecessary. However, for transparent plastics, rather simpler approaches, such as the proposed Schlick equation with empirically deviations

for transmission and wet behaviour should be sufficient. For specific non-polyethylene based plastics (*e.g.* 'Materbi'), data on direction properties seem to be needed as a prerequisite to meaningful simulation.

Presumably, advection effects which operate at two spatial scales affected measured temperatures. Large-scale heat advection from surface sources are between 2-100 m away. These very likely affected soil temperature predictions. However, in future studies, large-scale heat advection effects can be prevented by covering and ridging of rather large experimental fields (*e.g.* 400 m × 400 m) with similar plastics in regard to their heating or cooling performance. Additionally, required meteorological inputs should be taken from a central point within this area. Furthermore, due to additional short- and long-wave radiation gains from neighbouring ridges, at least three neighbouring rows should be tested per plastic.

Small-scale advection effects along a single ridge were shown to be evident and could not be circumvented via the introduced common exchange height. Deviations between hourly simulations and observations, which are contributable to small-scale advection effects, reached up to 3 K in this study. As the explicit consideration of these lateral heat fluxes is to complex and computational demanding, simpler advection equations are required. These may include (1) some spatial statistic of the ridge surface temperatures, (2) presumed vertical profiles of wind speed and (3) both vertical and horizontal scalar diffusivities. These factors should help to derive local lateral heat flux corrections.

Observations and simulations of a plastic with either heating and cooling abilities compared to uncovered ridges (*e.g.* 'Black/White' plastic) highlighted the possibility to control ridge temperatures efficiently. Here, prior states of heating or cooling were mostly overridden within 1-5 days at up to 40 cm soil depth from the ridge top. The dependence of different periods of adaptation on prior and actual conditions needs further investigations.

The presented model can be used in further application studies, *e.g.* to develop and test an asparagus spear growth model. Such a study could reveal information on the optimal timing of ridging and covering, the appropriate dimensions and orientations of ridges as

well as optimal radiative properties of plastic mulches required to maximise soil heating or cooling under transient meteorological conditions.

5 Summary

Implementation and application of Soil Vegetation Atmosphere Transport Models (SVAT) in agriculture require knowledge of aerodynamic properties of the exchanging surface. Therefore, one needs to specify several parameters such as the zero plane displacement (d), the roughness length for momentum ($z_{0,m}$), and additional parameters describing the roughness layer just above the canopy as the height of the roughness layer for momentum and scalars (Z_{m*}, Z_{s*}), and parameters of the modified diffusivity profile functions.

Several data summaries from the literature on aerodynamic properties over a broad range of plant canopies are used to develop and test predictive models for a number of needed aerodynamic parameters. A new predictive equation for d is presented as a function of canopy height (h_c) and Plant Area Index (PAI). A semi-empirical equation for the canopy length scale $L_s = u(h_c)/(\mathrm{d}u/\mathrm{d}z)$ (u horizontal wind speed) is derived from h_c, PAI, fractional crown height (f_{cr}), and inter-element spacing of roughness elements (D). Furthermore, for tall canopies ($h_c > 1.7$ m) Z_{m*} is well described by the simple relationship: $Z_{m*} = h_c + 2.32L_s$ and was also valid for sparse canopies from savannah sites with high D. For short canopies the relation $Z_{m*} = 2.42 \min(L_s, h_c)$ described data reasonable.

Having estimates of d, L_s, Z_{m*} and other inputs one can derive predictive equations for $z_{0,m}$ with choice of an appropriate profile function of momentum exchange enhancement in the roughness layer. From comparisons of predicted and observed roughness length $z_{0,m}$ it was concluded that use of the hyperbolic profile function proposed by CELLIER and BRUNET (1992) is more appropriate even for canopies with high relative spacing D/h_c where the functional form of GARRATT (1980) originated. Moreover using the hyperbolic profile function, predictions of $z_{0,m}$ were improved compared to a previous similar approach.

Assuming independence of buoyancy and roughness effects, the integrated stability/roughness layer functions were derived, and an approximate integration of the momentum function for unstable atmospheric conditions is proposed. Closed form analytical expressions are given for the friction velocity (u_*), the horizontal wind speed profile ($u(z)$) and the aerodynamic resistance (r_a), which account for both stability and roughness layer effects.

An energy balance model for a two-dimensional ridge surface partly covered by a plastic mulch as well and the linkage to a public domain soil simulation package (2DSOIL) is presented. Previous approaches are modified and extended to include (1) the circumsolar part of diffuse radiation and (2) the altered interception of diffuse short- and long-wave radiation due to horizon obstructions and surface slope and (3) the directional dependence of transmissivity and reflectivity of plastic mulches.

A simple solution was found for the short-wave radiation interception under an uniform radiating sky, and an extensive numerical simulation study with broadly varying sky conditions and surface geometries revealed an error of about 10% using this approximation. Similarly simulations for long-wave sky radiation interception highlighted the good predictive quality of the uniform sky solution with errors of about 1%.

Additionally, a thorough derivation of directional responses of transmissivity and reflectivity of different commonly used plastics is provided. Oblique direct radiation incidence angles due to ridged surfaces were taken into account using a Fresnel theory based approach adapted from window design research and extended to describe the effect of a liquid water film on the inside of the plastic.

The last section presents the calibration and validation procedure of the proposed simulation model to predict the temperature dynamics for soil ridges partly covered by a plastic mulch. To this end, soil temperatures were measured hourly over 3 months at two sites for 6 different plastic mulch – soil treatments. For calibration, only three parameters had to be estimated from data taken over one month at one site. Overall, simulated data fitted with the whole data set on soil temperatures, with root mean square

errors of 1.5 K and 1.9 K for both sites, respectively; thus confirming the validity of this approach.

Test simulations established that for opaque plastics, detailed analysis of directional radiative properties is not necessary, and for transparent plastics, rather simpler approaches, such as the Schlick equation, are sufficient to model directional transmissivity and reflectivity.

Small-scale advection effects along single ridges were evident, and hourly deviations (biases) between measurements and predictions caused by this effect reached up to 3 K.

Only a few inputs have to be provided to apply the model: the soil humus content and texture, the shape of the ridge, and the transmissivities and reflectivities of the used plastic mulches in the short-wave and long-wave range.

The presented model can be applied for optimisations regarding (1) the timing of ridging and covering, (2) the dimensions and orientations of ridges, and (3) the radiative properties of plastic mulches.

References

[1] Akaike, H. (1976): An information criterion, Mathematical Science (volume 14), issue 1, pp. 5-9.

[2] Albini, F. A. (1981): A phenomenological model for wind speed and shear stress profiles in vegetation cover layers, Journal of Applied Meteorology (volume 20), pp. 1325-1335.

[3] Amiro, B. D. (1990): Drag coefficients and turbulence spectra within three boreal forest canopies, Boundaray Layer Meteorology (volume 52), pp. 227-246.

[4] Angström, A. (1925): The albedo of various surfaces of ground, Geofiska Annaler (volume 7), issue 323, pp. 342.

[5] Avissar, R. (1986): Field Aging of transparent polyethylen mulches: II. Influences on the effectiveness of soil heating., Soil Science Society of America Journal (volume 50), issue 1, pp. 205-209.

[6] Avissar, R.; Mahrer, Y.; Margulies, L. und Katan, J. (1986): Field aging of transparent polyethylene mulches: I. Photometric properties, Soil Science Society of America Journal (volume 50), issue 1, pp. 202-209.

[7] Baldocchi, D. D. und Meyers, T. P. (1988): Turbulence structure in a deciduos forest, Boundary-Layer Meteorology (volume 43), pp. 345-364.

[8] Baldocchi, D. D. und Harley, P. C. (1995): Scaling carbon dioxide and water vapour exchange from leaf to canopy in a deciduous forest. 2. Model testing and application, Plant, Cell and Environment (volume 18), pp. 1157-1173.

[9] Baumer, O. W. (1990): Prediction of soil hydraulic parameters, SCS National Soil Survey Laboratory, WEPP Data Files for Indiana , Lincoln, NE.

[10] Briscoe, B. J. und Galvin, K. P. (1991): The effect of surface fog on the transmittance of light, Solar Energy (volume 46), pp. 191-197.

[11] Brunet, Y.; Finnigan, J. J. und Raupach, M. R. (1994): A wind tunnel study of air flow in waving wheat: single-point velocity statistics, Boundary-Layer Meteorology (volume 70), issue 1-2, pp. 95-132. URL: ISI:A1994PD04200006

[12] Brutsaert, W. (1982): Evaporation into the atmosphere, 1. edition , Davenport, A. J.; Hicks, B. B.; Hilst, G. R.; Munn, R. E. und Smith, J. D., Kluwer Academic Publishers, Dordrecht, The Netherlands.

[13] Campbell, G. S.; Jungbauer, J. D.; Bidlake, W. R. und Hungerford, R. D. (1994): Precdicting the effect of temperature on soil thermal conductivity, Soil Science (volume 94), pp. 307-313.

[14] Cellier, P. und Brunet, Y. (1992): Flux-gradient relationships above tall plant canopies, Agricultural and Forest Meteorology (volume 58), pp. 93-117.

[15] Chung, S. und Horton, R. (1987): Soil heat and water flow with a partial surface mulch, Water Resources Research (volume 23), issue 12, pp. 2175-2186.

[16] Coelho, J. M. P.; Abreu, M. A. und Rodrigues, F. C. (2004): Methodologies for determening thermoplastic films optical parametrs at 10.6(mycro)m laser wavelength, polymer testing (volume 23), pp. 307-312.

[17] De Luca, V. und Ruocco, G. (2000): A transient-spectral thermal model of soil under radiative- interfering cover, Journal of Agricultural Engineering Research (volume 77), issue 1, pp. 93-102. URL: ISI:000089603300007

[18] De Vries, D. A. (1963): Thermal properties of soils, van Wijk, W. R., Physics of plant environment , pp. 210-235, John Wiley and Sons, Inc., New York.

[19] De Wit, C. T. (1965): Photosynthesis of leaf canopies (volume 663), Pudoc, Wageningen, the Netherlands.

[20] Denmead, O. T. (1976): Temperate cereals, Monteith, J. L., Vegetation and the Atmosphere, Volume 2 Case Studies , pp. 1-31, Academic Press, London.

[21] Dickinson, R. E.; Henderson-Sellers, A.; Kennedy, P-J. und Wilson, M. F. (1986): Biosphere-atmosphere transfer scheme (BATS) for the NCAR community climate model, National Center for Atmospheric Research, Boulder, Colorado.

[22] Dong, A.; Grattan, S.; Carroll, J. und Prashar, C. (1992): Estimation of daytime net radiation over well-watered grass, Journal of Irrigation and Drainage Engineering (volume 118), issue 3, pp. 466-471.

[23] Farouki, O. T. (1986): Thermal properties of soils, 11. edition , Technical University Clausthal, Clausthal-Zellerfeld, Germany.

[24] Fazu, C. und Schwerdtfeger, P. (1989): Flux-gradient relationships form momentum and heat over a rough natural surface, Quarterly Journal of the Royal Meteorological Society (volume 115), pp. 335-352.

[25] Garratt, J. R. (1977): Aerodynamic roughness and mean monthly surface stress over Australia, 29. edition , CSIRO, Australia.

[26] Garratt, J. R. (1980): Surface influence upon vertical profiles in the atmospheric near-surface layer, Quarterly Journal of the Royal Meteorological Society (volume 106), pp. 803-819.

[27] Garratt, J. R. (1983): Surface influence upon vertical profiles in the nocturenal boundaray layer, Boundary-Layer Meteorology (volume 26), issue 69, pp. 80.

[28] Habib, E.; Krajewski, W. F.; Nespor, V. und Kruger, A. (1999): Numerical simulation studies of rain gaga data correction due to wind effect, Journal of Geophysical Research (volume 104), issue D16, pp. 19,723-19,733.

[29] Hagen, L. J. und Armbrust, D. V. (1992): Aerodynamic roughness and saltation trapping efficiency of tillage ridges, Transactions of the ASAE (volume 35), issue 4, pp.

1179-1184. URL: ISI:A1992JY49800014

[30] Ham, J. M. und Kluitenberg, G. J. (1994): Modeling the effect of mulch optical-properties and mulch soil contact resistance on soil heating under plastic mulch culture, Agricultural and Forest Meteorology (volume 71), issue 3-4, pp. 403-424. URL: ISI:A1994PP63600011

[31] Hay, J. E. (1979): Calculation of monthly mean solar radiation for horizontal and inclined surfaces, Solar Energy (volume 23), pp. 301-307.

[32] Heißner, A.; Schmidt, S. und von Elsner, B. (2005): Comparison of plastic films with different optical properties for soil covering in horticulture: test under simulated environmental conditions, Journal for the Science of Food and Agriculture (volume 85), pp. 539-548.

[33] Horton, R. und Wierenga, P. J. (1984): The effect of column wetting on soil thermal conductivity, Soil Science (volume 138), pp. 102-107.

[34] Högstrom, U.; Bergstrom, H.; Smedman, A. S.; Halldin, S. und Lindroth, A. (1989): Turbulent exchange above a pine forest 1. Fluxes and gradients, Boundary-Layer Meteorology (volume 49), issue 1-2, pp. 197-217. URL: ISI:A1989CB30000010

[35] Idso, S. B.; Jackson, R. J.; Reginato, R. J.; Kimball, B. A. und Nakayama, F. S. (1975): The dependence of bare soil albedo on soil water content, Agricultural and Forest Meteorology (volume 14), pp. 109-113.

[36] Incropera, F. P. und DeWitt, D. P. (2002): Fundamentals of heat and mass transfer, 5. edition , John Wiley & Sons, New York.

[37] Jacobs, A. F. G. und van Boxel, J. (1988): Changes of the displacement height and roughness length of maize during a growing season, Agricultural and Forest Meteorology (volume 42), pp. 53-62.

[38] Katul, G.; Hsieh, C-I.; Bowling, D.; Clark, K.; Shurpali, N.; Turnipseed, A.;

Albertson, J.; Tu, K.; Hollinger, D. Y.; Evans, B.; Offerle, B.; Anderson, D.; Ellsworth, D.; Vogel, C. und Oren, R. (2006): Spatial variability of turbulent fluxes in the roughness sublayer of an even aged pine forest, Boundary-Layer Meteorology (volume 93), pp. 1-28.

[39] Kimball, B. A.; Jackson, R. D.; Reginato, R. J.; Nakayama, F. S. und Idso, S. B. (1976): Comparison of field-measured and calculated soil-heat fluxes, Soil Science Society of America Journal (volume 40), issue 1, pp. 18-25. URL: ISI:A1976BN71500005

[40] Koitzsch, R.; Dzingel, M.; Foken, Th. und Mücket, G. (1988): Probleme der experimentellen Erfassung des Energieaustausches über Winterweizen, Z.Meteorol. (volume 38), pp. 150-155.

[41] Kustas, W. P. und Norman, J. M. (1999): Evaluation of soil and vegetation heat flux predictions using a simple two-source model with radiometric temperatures for partial canopy cover, Agricultural and Forest Meteorology (volume 94), pp. 13-29.

[42] Lo, C.; Palmer, B.; Drost, M. und Welty, J. (1995): Incorporation of polarization effects in Monte Carlo simualtions of radiative heat transfer, Numerical Heat Transfer, Part A (volume 27), pp. 129-142.

[43] Mahrer, Y. (1982): A theoretical study of the effect of soil surface shape upon the soil temperature profile, Soil Science (volume 134), pp. 381-387.

[44] Mahrer, Y.; Naot, O.; Rawitz, E. und Katan, J. (1984): Temperature and moisture regimes in soils mulched with transparent polyethylen, Soil Science Society of America Journal (volume 48), pp. 362-367.

[45] Mahrer, Y. und Avissar, R. (1985): A numerical study of the effect of soil surface shape upon the soil temperature and moisture regimes, Soil Science (volume 139), pp. 483-490.

[46] Massman, W. J. (1996): An analytical one-dimensional model of momentum

transfer by vegetation of arbitary structure, Boundary-Layer Meteorology (volume 83), pp. 407-421.

[47] Massman, W. J. (1999): A model of kB^{-1}_H for vegetated surfaces unsing 'localized near - field' Langrangian theory, Journal of Hydrology (volume 223), pp. 27-43.

[48] Mathsoft Engineering & Education, Inc (2001): Axum 7 for Windows User's Guide, Mathsoft Engineering & Education, Inc., Cambridge, Massachusetts.

[49] Matthias, A. D. und Hernandez, A. R. P. (1998): Modeling temperatures in soil under an opaque cylindrical enclosure, Agricultural and Forest Meteorology (volume 90), issue 1-2, pp. 27-38. URL: ISI:000073312400003

[50] McInnes, K. J.; Heilman, J. L. und Gesch, R. W. (1991): Momentum roughness and zero-plane displacement of ridge-furrow tilled soil, Agricultural and Forest Meteorology (volume 55), pp. 167-179.

[51] Meakin, P. (1992): Droplet deposition growth and coalescence, Reports on Progress in Physics (volume 55), issue 2, pp. 157-240. URL: ISI:A1992HP31300002

[52] Monteith, J. L. und Unsworth, M. H. (1990): Principles of environmental physics, Edward Arnold, London.

[53] Mölder, M.; Grelle, A.; Lindroth, A. und Halldin, S. (1999): Flux profile relationships over a boreal forest - roughness sublayer corrections, Agriculture and Forest Meteorology (volume 98-99), pp. 645-658.

[54] Mualem, Y. (1976): A new model for predicting the hydraulic conductivity of unsaturated porous media, Water Resources Research (volume 12), pp. 513-522.

[55] Naot, O.; Mahrer, Y.; Rawitz, E.; Avissar, R. und Katan, J. (1987): The effect of reirrigation on the thermal regime of polyethylene-mulched soils: experimental and numerical studies, Soil Science (volume 144), issue 2.

[56] Novak, M. D. (1993): Analytical solutions for 2-dimensional soil heat-flow with radiation surface boundary-conditions, Soil Science Society of America Journal (volume 57), issue 1, pp. 30-39. URL: ISI:A1993KW02200006

[57] Pereira, A. R. und Shaw, R. H. (1980): A numerical experiment on the mean wind structure inside canopies of vegetation, Agricultural Meteorology (volume 22), pp. 303-318.

[58] Perez, R.; Seals, R. und Michalsky, J. (1993): All-weather model for sky luminance distribution-preliminary configuration and validation, Solar Energy (volume 51), issue 5, pp. 423-423. URL: ISI:A1993MC49600016

[59] Physick, W. L. und Garratt, J. R. (1995): Incorporation of a high-roughness lower boundary into a mesoscale model for studies of dry deposition over complex terrain., Boundary-Layer Meteorology (volume 74), pp. 55-71.

[60] Piergiovanni, L.; Fava, P. und Sicilano, A. (1995): A mathematical model for the prediction of water vapor transmission rate at different temperature and relative humidity combinations, Packaging Technology and Science (volume 8), pp. 73-83.

[61] Pollet, I. V. und Pieters, J. G. (2000): Condensation and radiation transmittance of greenhouse cladding materials, part 3: Results for glass plates and plastic films, Journal of Agricultural Engineering Research (volume 77), issue 4, pp. 419-428. URL: ISI:000166485500008

[62] Post, D.; Fimbres, A.; Matthias, A. D.; Sano, E.; Accioly, L.; Batchily, A. und Ferreira, L. (2000): Predicting soil albedo from soil color and spectral reflectance data, Soil Science Society of America Journal (volume 64), issue 3, pp. 1027-1034.

[63] Press, W. H.; Teukolsky, S. A.; Vetterling, W. T. und Flannery, B. P. (1992): Numerical recipes, 2. edition , Press Syndicate of the University of Cambridge, Cambridge.

[64] Qirk, R. P. und Alsamarraie, M. A. A. (1999): Physical constants of poly(ethylene),

Brandrup, J. und Immegrut, E. H. , Polymer Handbook , 3. edition, John Wiley & Sons, New York.

[65] Rauner, J. L. (1976): Deciduous forests, Monteith, J. L., Vegetation and the Atmosphere, Volume 2 Case Studies , pp. 241-264, Academic Press, London.

[66] Raupach, M. R.; Thom, A. S. und Edwards, I. (1980): A wind tunnel study of turbulent flow close to regularly arrayed rough surfaces, Boundary-Layer Meteorology (volume 18), pp. 373-397.

[67] Raupach, M. R. und Thom, A. S. (1981): Turbulence in and above plant canopies, Annual Review of Fluid Mechanics (volume 13), pp. 97-129.

[68] Raupach, M. R. (1987): A langrangian analysis of scalar transfer in vegetation canopies, Quarterly Journal of the Royal Meteorology Society (volume 113), pp. 107-120.

[69] Raupach, M. R.; Atonia, R. A. und Rajagopalan, S. (1991): Rough-wall turbulent boundary layers, Applied Mechanical Reviews (volume 44), issue 1, pp. 1-25.

[70] Raupach, M. R. (1992): Drag and drag partition on rough surfaces, Boundary-Layer Meteorology (volume 60), pp. 375-395.

[71] Raupach, M. R. (1994): Simplified expressions for vegetation roughness length and zero-plane displacement as functions of canopy height and area index, Boundary-Layer Meteorology (volume 71), issue 1-2, pp. 211-216. URL: ISI:A1994PR60400013

[72] Raupach, M. R. (1995): Corrigenda, Boundary-Layer Meteorology (volume 76), pp. 303-304.

[73] Raupach, M. R.; Finnigan, J. J. und Brunet, Y. (1996): Coherent eddies and turbulence in vegetation canopies: The mixing-layer analogy, Boundary-Layer Meteorology (volume 78), issue 3-4, pp. 351-382. URL: ISI:A1996VB07200005

[74] Ripley, E. A. und Redmann, R. E. (1976): Grassland, Monteith, J. L., Vegetation and the Atmosphere, Volume 2 Case Studies , pp. 349-398, Academic Press, London.

[75] Rubin, M.; von Rottkay, K. und Powles, R. (1998): Window optics, Solar Energy (volume 62), pp. 149-161.

[76] Saleh, A.; Fryear, D. W. und Bilbro, J. D. (1997): Aerodynamic roughness prediction from soil surface roughness measurement, Soil Science (volume 162), issue 3, pp. 205-210. URL: ISI:A1997WP07700006

[77] Saugier, B. (1976): Sunflower , Monteith, J. L., Vegetation and the Atmosphere, Volume 2 Case Studies , pp. 87-119, Academic Press, London.

[78] Saxton, K. E.; Rawls, W. J.; Romberger, J. S. und Papendick, R. I. (1986): Estimating generalized soil-water characteristics from texture, Soil Science Society of America Journal (volume 50), issue 4, pp. 1031-1036. URL: ISI:A1986D639500039

[79] Schaap, M. G.; Leij, F. J. und van Genuchten, M. T. (1998): Neural network analysis for hierarchical prediction of soil hydraulic properties, Soil Science Society of America Journal (volume 62), issue 4, pp. 847-855.

[80] Schaap, M. G. und Leij, F. J. (2000): Improved prediction of unsaturated hydraulic conductivity with the Mualem-van Genuchten model, Soil Science Society of America Journal (volume 64), issue 3, pp. 843-851. URL: ISI:000089446300005

[81] Schelde, K.; Thomsen, A.; Heidmann, T.; Schjonning, P. und Jansson, P. E. (1998): Diurnal fluctuations of water and heat flows in a bare soil, Water Resources Research (volume 34), issue 11, pp. 2919-2929. URL: ISI:000076652600013

[82] Sharon, D. (1980): The distribution of effective rainfall incident on sloping ground, Journal of Hydrology (volume 46), pp. 165-188.

[83] Sharratt, B. S.; Schwarzer, M. J.; Campbell, G. S. und Papendick, R. I. (1992): Radiation balance of ridge-tillage with modeling strategies for slope and aspect in the

sub-arctic, Soil Science Society of America Journal (volume 56), issue 5, pp. 1379-1384. URL: ISI:A1992JX04200008

[84] Shaw, R. H. und Pereira, A. R. (1982): Aerodynmaic roughness of a plant canopy: a numerical experiment., Agricultural Meteorlogy (volume 26), pp. 51-65.

[85] Skartveit, A.; Olseth, J. A. und Tuft, M. E. (1998): An hourly diffuse fraction model with correction for variability and surface albedo 5, Solar Energy (volume 63), issue 3, pp. 173-183. URL: ISI:000076522600004

[86] Soegaard, H. (1999): Fluxes of carbon dioxide, water vapour and sensible heat in a boreal agricultural area of sweden- scaled from canopy to landscape level, Agricultural and Forest Meteorology (volume 98-99), pp. 463-478.

[87] Sui, H.; Zeng, D. und Chen, F. (1992): A numerical model for simulating the temperature and moisture regimes of soil under various mulches, Agricultural and Forest Meteorology (volume 61), issue 3-4, pp. 281-299.

[88] Tarnawski, V. R.; Gori, F.; Wagner, B. und Buchan, G. D. (2000): Modelling approaches to predicting thermal conductivity of soils at high temperatures, International Journal of Energy Research (volume 24), pp. 403-423.

[89] Thom, A. S. (1971): Momentum absorption by vegetation, Quarterly Journal of the Royal Meteorology Society (volume 97), pp. 414-428.

[90] Tietje, O. und Hennings, V. (1996): Accuracy of the saturated hydraulic conductivity prediction by pedo-transfer functions compared to the variability within FAO textural classes, Geoderma (volume 69), issue 1-2, pp. 71-84. URL: ISI:A1996TN34600004

[91] Timlin, D.; Acock, B. und van Genuchten, R. (1996): 2DSOIL – A modular simulator of soil and root processes (volume 3), Remote sensing and modelling Lab, Soil Salinity Lab, Beltsville, MD and Riverside, CA.

[92] Unsworth, M. H. und Monteith, J. L. (1975): Long-wave radiation at the ground I. Angular distribution of incoming radiation, Quarterly Journal of the Royal Meteorological Society (volume 101), pp. 13-24.

[93] van Bavel, C. H. M. und Hillel, D. (1976): Calculating potential and actual evaporation from a bare soil surface by simulation of concurrent flow of water and heat, Agricultural Meteorology (volume 17), pp. 453-476.

[94] Vartiainen, E. (2000): a new approach to estimating the diffuse irradiance on inclined surfaces, Renewable Energy (volume 20), pp. 45-64.

[95] Vereecken, H.; Maes, J. und Feyen, J. (1990): Estimating unsaturated hydraulic conductivity from easily measured soil properties, Soil Science (volume 149), issue 1, pp. 1-12 . URL: ISI:A1990CP31000001

[96] Verhoef, A.; McNaughton, K. G. und Jacobs, A. F. G. (1997): A parametrization of momentum roughness length and displacement height for a wide range of canopy densities, Hydrology and Earth System Sciences (volume 1), pp. 81-91.

[97] Weinläder, H.; Pottler, K. ; Beck, A. und Fricke, J. (2002): Angular-dependent measurements of the thermal radiation of the sky, High Temperatures-High Pressures (volume 34), pp. 1413-1420.

[98] Wu, Y.; Perry, K. B. und Ristaino, J. B. (1996): Estimating temperature of mulched and bare soil from meterological data, Agriculture and Forest Meteorology (volume 81), pp. 299-323.

[99] Yamanaka, T. und Yonetani, T. (1999): Dynamics of the evaporation zone in dry sandy soils, Journal of Hydrology (volume 217), pp. 135-148.

[100] Zhao, H. und Beysens, D. (1995): From droplet growth to film growth on a heterogeneous surface: condensation associated with a wettability gradient, Langmuir (volume 11), pp. 627-634.